DISK ACCRETION TO ROTATING MAGNETIZED STARS: MAGNETOHYDRODYNAMIC SIMULATIONS

A Dissertation

Presented to the Faculty of the Graduate School

of Cornell University

in Partial Fulfillment of the Requirements for the Degree of

Doctor of Philosophy

by

Min Long

May 2008

DISK ACCRETION TO ROTATING MAGNETIZED STARS:

MAGNETOHYDRODYNAMIC SIMULATIONS

Min Long, Ph.D.

Cornell University 2008

The star-disk interaction between a rotating magnetized star and a surrounding accretion disk is a fundamental process in astrophysics, and is usually difficult to investigate due to the complicated magnetohydrodynamic structures. The aim of this work is for understanding the accretion manifestations of this interaction, especially the mechanism of the transport of the angular momentum, and the influence of the complex magnetic geometries on the accretion behavior.

One of the complicated aspects of the disk-magnetosphere interaction is the angular momentum transport between the disk and the star. It was proposed that the ralation between spin-up torque arising from the magnetic connection of the star to the fast rotating inner part of the disk, and the spin-down torque arising from the connection of the star to the slow rotating outer part of the disk determines the spin evolution of the star. It was suggested that for a particular value of the star's rotation rate, the positive spin-up torque balances the negative spin-down torque and the star is "locked" in the rotational equilibrium state. We improve the model of the transport of the angular moment and present the most probable periods of rotation in the equilibrium state for different astrophysical objects, such as classical T Tauri stars, dwarf novae and millisecond X-ray pulsars.

The magnetic geometry of a rotating star can have a strong influence on the matter in an accretion disk, which is disrupted and channelled by the magnetic

field to the star along the field lines. Theoretical and observational approaches reveal that the actual magnetic geometries of stars may depart from the pure dipole configuration. We study the accretion in different complex magnetic configurations including pure quadrupole, aligned dipole plus quadrupole, misaligned dipole plus quadrupole and superposition of off-centre dipoles. The results show that they have different features in matter flow, hot spots on the surface of the star and associated light curves, such as accretion "belt", extended ring-like hot spots and non-sinusoidal variations of light curves for large inclination angle, which could be used as an indicators of a complex field.

BIOGRAPHICAL SKETCH

Min Long was born and grew up in Nanjing, China, an ancient capital of six dynasties with a history of 2500 years. He received his Bachelors and Masters degrees with honors in Astrophysics from the Department of Astronomy, Nanjing University in 1999 and 2001 respectively. After that, he began to study at Cornell University.

To my parents.

To my friends for supporting me for years.

ACKNOWLEDGEMENTS

This thesis would not have been possible without many people who helped me throughout my graduate study. I would like to express gratitude to Prof. Richard Lovelace for his invaluable guidance as my advisor, and Dr. Marina Romanova for her constant support and excellent academic suggestions. Richard is very nice and always willing to offer help to his students. He also impressed us with his great insights into the different fields of theoretical astrophysics. Marina is enthusiastic and introduced me to work on the magnetohydrodynamic simulations of the disk accretion to rotating magnetized stars, which becomes a more and more active subject.

I am fortunate to have these outstanding professors in my special committee, James Cordes, Éanna Flanagan and Dong Lai, who not only examined me, but also encouraged and suggested me a lot.

I want to express my sincere acknowledgement to the professors who I've worked with over the years, Phillip Nicholson, Donald Campbell, Paul Goldsmith. I really enjoyed that time.

Special thanks to Prof. James Bell, as our Director of Graduate Studies, who was always there whenever I needed signatures for planning conferences, scheduling exams and so on. In particular, I want to express my respect to him for opening his family to all the students in Astronomy Department who couldn't enjoy family reunion during holidays.

Thanks to my fellow graduate students, especially Akshay Kulkarni for his help.

Thanks to everyone in the Space Sciences Building.

TABLE OF CONTENTS

LIST OF TABLES

LIST OF FIGURES

CHAPTER 1

INTRODUCTION

The star-disk interaction between a rotating magnetized star and a surrounding accretion disk is a fundamental process in astrophysics, and is usually difficult to investigate due to the complicated magnetohydrodynamic (MHD) structures. In this thesis we consider two important aspects of this interaction, one is the disk locking and the mechanism of the transport of the angular momentum, the other is the influence of the complex magnetic geometries on the accretion behavior.

The star is "locked" in the rotational equilibrium state if the net torque on the star is zero. In the first models of the disk-magnetosphere interaction it was proposed that the magnetic field has a dipole configuration everywhere and that the relation between spin-up torque which arises from the magnetic connection of the star to the disk within the corotation radius r_{co} and the spin-down torque which arises from the connection beyond the corotation radius determines the spin evolution of the star (Ghosh, Lamb & Pethick 1977; Ghosh & Lamb 1978, 1979). It was suggested that for a particular value of the star's rotation rate, Ω_{eq}, the positive spin-up torque balances the negative spin-down torque (Ghosh & Lamb 1978, 1979; Wang 1995). This model has been developed and studies show that the inflation of field lines due to the difference in the angular velocities of the foot-points (Lovelace, Romanova & Bisnovatyi-Kogan 1995; Shu et al. 1994; Bardou 1999, Uzdensky, Königl & Litwin 2002) could change the rotational equilibrium state. Our goal is to derive the conditions for the rotational equilibrium state using axisymmetric 2.5-dimensional (2.5D) MHD simulations of the disk-magnetosphere interaction.

The magnetic geometry of a rotating star can have a strong influence on the matter in an accretion disk, which is disrupted and channelled by the magnetic field to the star along the field lines. The properties of such accretion will depend on the structure of the magnetic field of the star. In early models it was assumed that the star's intrinsic magnetic field was a pure *dipole* (Ghosh & Lamb 1979a,b; Camenzind 1990; Königl 1991). However, the actual configuration of the magnetic field of strongly magnetized stars may depart from the dipole one. For example, Safier (1998) presented a number of arguments pointing to a non-dipolar magnetic fields in some CTTSs. The Zeeman measurements of the magnetic field of a number of CTTSs based on the photospheric lines show that the magnetic field at the surface of CTTSs is strong (1-3 kGs) but not ordered, which means that close to the star the magnetic field is non-dipole (e.g., Johns-Krull et al. 1999; Johns-Krull, Valenti, & Koresko 1999; Johns-Krull & Gafford 2002; Smirnov et al. 2003).

We study the accretion in different complex magnetic configurations including pure quadrupole, aligned dipole plus quadrupole, misaligned dipole plus quadrupole and superposition of off-centre dipoles. The results show that they have different features in matter flow, hot spots on the surface of the star and associated light curves, such as accretion "belt", extended ring-like hot spots and non-sinusoidal variations of light curves for large inclination angle, which could be used as an indicators of a complex field.

In Chapter 2, we introduce the numerical methods for calculating magnetohydrodynamic equations in principle, and we present the theoretical description of our model, grid, initial and boundary conditions and references units used in simulations.

In Chapter 3, we investigate the transport of the angular momentum between the star and the disk. We search for rotational equilibrium state of a disk accreting magnetized star by using axisymmetric 2.5D magnetohydrodynamic simulations and present conditions when the spin-up torque exserted to the star balances the spin-down torque. We investigate different situations including one with a relatively weak stellar magnetic field plus high coronal density, and one with a stronger stellar field plus a lower coronal density. We observe that for both cases the rotation of the star is locked to the rotation of the disk and opened field lines carry significant angular momentum out of the star. In the equilibrium state the corotation radius r_{co} is related to the magnetospheric radius r_A as $r_{co}/r_A \approx 1.2 - 1.5$, which could be used to estimate most probable periods of rotation in the equilibrium state for classical T Tauri stars, dwarf novae and X-ray millisecond pulsars.

In Chapter 4 & 5, we study the influence of magnetic geometries of the star on the accretion process. First, we consider some simple non-dipole magnetic configurations by using in full three-dimensional (3D) magnetohydrodynamic simulations, for the first time. They are pure quadrupole configuration and aligned dipole plus quadrupole configuration, i.e., the quadrupole magnetic moment $\mathbf{D}$ is taken to be parallel to the dipole magnetic moment $\boldsymbol{\mu}$, and both are inclined relative to the spin axis of the star $\boldsymbol{\Omega}$ at an angle Θ. Unlike polar funnel flow and arch-like hot spots in pure dipole case, in the cases with quadrupole components, partial accreting matter flows to the magnetic equator and forms a quadrupole accretion "belt" in the disk and ring-shape hot spots on the star. And we conclude: (1) Angular momentum flow between the star and disk is less efficient in the case of the quadrupole field; (2) Hot spots are hotter and brighter in case of the dipole field because the matter accelerates over a longer

distance compared with the flow in a quadrupole case. However, the associated light curves could be similar if the inclination angle is small.

Next, we discuss more complicated situations, including misaligned dipole plus quadrupole configuration and superposition of off-centre dipole configurations. The simulations show that when the quadrupole component is comparable to the dipole component, the magnetic field has a complex structure with three major magnetic poles on the surface of the star and three sets of loops of field lines connecting them. A significant amount of matter flows between loops of field lines to a quadrupole accretion "belt", forming a ring-like hot spot on the star. If the maximum strength of the magnetic field on the star is fixed, then we observe that the mass accretion rate, the torque on the star and the area covered by hot spots are several times smaller in the quadrupole-dominant cases than in the pure dipole cases. The influence of the quadrupole component on the shape of the hot spots becomes noticeable when the ratio of the quadrupole and dipole field strengths $B_q/B_d \gtrsim 0.5$, or dominant when $B_q/B_d \gtrsim 1$. In the case of an off-centre dipole field, most of the matter flows through a one-armed accretion stream, forming a large hot spot on the surface, with a second much smaller secondary spot. The light curves may have simple, sinusoidal shapes, thus mimicking stars with pure dipole fields. Or, they could be complex and unusual. In some cases, the light curves may be indicators of a complex field, in particular if the inclination angle is known independently.

CHAPTER 2

THEORETICAL DESCRIPTION AND NUMERICAL METHOD

The magnetohydrodynamic (MHD) equations characterize the state of the sufficiently collisional plasma, including the accreting matter around magnetized stars. These partial differential equations (PDE) rule the dynamics of the magnetized plasma around accreting stars and are usually very complicated due to the MHD characteristic structures. The problem is hard to investigate with analytical methods in some aspects because different simplifying assumptions lead to different conclusions. For numerical investigation, the problem is still hard, but a lot of effort has been devoted to solve MHD equations numerically in recent years.

In this chapter, first, we write the MHD equations in conservative forms, and then discuss the Riemman problem and one of its solution method: the Godunov method. After that, we present the grids, the initial and boundary conditions used in the simulation for such non-linear system.

2.1 The MHD Equations in Conservative Forms

The disk-magnetoshpere interaction is considered to be described by the time-dependant MHD equations, which consist of the continuity equation for the mass density ρ, the equations of motion for the velocity $\boldsymbol{v}$, the law of conservation of energy for the pressure p and the reduced form of Maxwell equations for the magnetic field $\boldsymbol{B}$ which do not explicitly include the electric field or displacement current. In addition, the equation of the state should also be considered.

These physical variables ρ, $\boldsymbol{v} = (u, v, w)$ where u, v, w are components of the

velocity, p and $\boldsymbol{B} = (B_1, B_2, B_3)$ are called primitive variables and governed by the following full set of MHD equations:

$$\frac{\partial \rho}{\partial t} + \nabla \cdot (\rho \boldsymbol{v}) = 0 \,, \tag{2.1}$$

$$\rho \frac{\mathrm{d}\boldsymbol{v}}{\mathrm{d}t} = -\nabla p + \rho\, \boldsymbol{g} + \frac{1}{4\pi}(\nabla \times \boldsymbol{B}) \times \boldsymbol{B} + \boldsymbol{F}^{vis}, \tag{2.2}$$

$$\frac{\partial (\rho S)}{\partial t} + \nabla \cdot (\rho \boldsymbol{v} S) = Q, \tag{2.3}$$

$$\frac{\partial \boldsymbol{B}}{\partial t} + \nabla \times (\boldsymbol{B} \times \boldsymbol{v}) = \eta \nabla^2 \boldsymbol{B}, \tag{2.4}$$

$$\nabla \cdot \boldsymbol{B} = 0 \,. \tag{2.5}$$

Here, $S = p/\rho^{\gamma}$ is the entropy per unit mass, $\boldsymbol{g}$ is the gravitational acceleration due to the star of mass M, Q is the Lagrangian change of the entropy, $\boldsymbol{F}^{vis}$ is the viscous force. The viscosity model of Shakura and Sunyaev (1973) is used with viscosity coefficient $\nu = \alpha_v c_s h$, the diffusivity term is $\eta = \alpha_d c_s h$, where h is the scale height of the disk, $c_s = (\gamma p/\rho)^{1/2}$ is the sound speed, and parameters α_v and α_d are dimensionless with values $\sim 0.01 - 1$ considered here. The ideal MHD equations correspond to the above equations with no resistivity.

The MHD equations can also be written in terms of conserved variables: the density ρ, the momentum $\rho\boldsymbol{v}$, the total energy ε and the magnetic field $\boldsymbol{B}$. This choice of variables naturally reflects the fundamental laws of conservation of mass, momentum and energy and has more advantages in numerical calculations. Because the number of conservation laws equals the number of variables, we can say the MHD equations are written in conservative form:

$$\frac{\partial \boldsymbol{U}}{\partial t} + \nabla \cdot \boldsymbol{F}(\boldsymbol{U}) = 0 \tag{2.6}$$

where the $\boldsymbol{F}(U)$ is the flux. For ideal MHD equations, one choice (ref. Balsara & Kim 2004) of the conserved variables is,

$$\boldsymbol{U} = \left(\rho, \rho u, \rho v, \rho w, \varepsilon, B_1, B_2, B_3\right)^T \tag{2.7}$$

where,

$$\varepsilon = \frac{\rho \boldsymbol{v}^2}{2} + \frac{p}{\gamma - 1} + \frac{B^2}{8\pi} \tag{2.8}$$

and the corresponding flux is,

$$\boldsymbol{F} = (F_1, F_2, F_3)^T, \tag{2.9}$$

and we define the column vectors,

$$F_1 = \begin{pmatrix} \rho u \\ \rho u^2 + p + \frac{B^2}{8\pi} - \frac{B_1^2}{4\pi} \\ \rho uv - \frac{B_1 B_2}{4\pi} \\ \rho uw - \frac{B_1 B_3}{4\pi} \\ (\varepsilon + p + \frac{B^2}{8\pi})u - \frac{B_1(\boldsymbol{v}\cdot\boldsymbol{B})}{4\pi} \\ 0 \\ uB_2 - vB_1 \\ -(wB_1 - uB_3) \end{pmatrix} \tag{2.10}$$

$$F_2 = \begin{pmatrix} \rho v \\ \rho uv - \frac{B_1 B_2}{4\pi} \\ \rho v^2 + p + \frac{B^2}{8\pi} - \frac{B_2^2}{4\pi} \\ \rho vw - \frac{B_2 B_3}{4\pi} \\ (\varepsilon + p + \frac{B^2}{8\pi})v - \frac{B_2(\boldsymbol{v}\cdot\boldsymbol{B})}{4\pi} \\ -(uB_2 - vB_1) \\ 0 \\ vB_3 - wB_2 \end{pmatrix} \tag{2.11}$$

$$F_1 = \begin{pmatrix} \rho w \\ \rho uw - \frac{B_1 B_3}{4\pi} \\ \rho vw - \frac{B_2 B_3}{4\pi} \\ \rho w^2 + p + \frac{B^2}{8\pi} - \frac{B_3^2}{4\pi} \\ (\varepsilon + p + \frac{B^2}{8\pi})w - \frac{B_3(\boldsymbol{v}\cdot\boldsymbol{B})}{4\pi} \\ wB_1 - uB_3 \\ -(vB_3 - wB_2) \\ 0 \end{pmatrix} \tag{2.12}$$

For realistic non-linear system, the non-ideal MHD equations should be used and the equations in conservative forms could be more complicated. The purpose of the MHD simulations is to solve MHD equations in conservative form with necessary initial and boundary conditions.

2.2 Riemann Problem and the Godunov Method

Hyperbolic PDE of conservation laws, including MHD equations, describe the physical process in various systems. The exact or approximate method to solve

the Riemann problem is called the Riemann solver, which is very useful for obtaining the solution of hyperbolic PDE of conservation laws in non-linear systems, since properties like shocks appear naturally in the solution.

The simplest Riemann problem with initial condition (IC) is,

$$\begin{aligned} &\text{PDE}: \quad \tfrac{\partial u}{\partial t} + a\tfrac{\partial u}{\partial x} = 0 \\ &\text{IC}: \quad u(x,0) = u_0(x) = \begin{cases} u_L & (x<0), \\ u_R & (x>0), \end{cases} \end{aligned} \tag{2.13}$$

where a, u_L, u_R are constant values. The initial condition shows the discontinuity at $x = 0$.

The Riemann problem for scalar non-linear conservation laws is,

$$\begin{aligned} &\text{PDE}: \quad \tfrac{\partial u}{\partial t} + \tfrac{\partial f(u)}{\partial x} = 0 \\ &\text{IC}: \quad u(x,0) = u_0(x) = \begin{cases} u_L & (x<0), \\ u_R & (x>0), \end{cases} \end{aligned} \tag{2.14}$$

where $f(u)$ is the flux for conservation law.

Generally, the Riemann problem with ICs and boundary conditions (BCs) for linear and non-linear hyperbolic systems are:

$$\begin{aligned} &\text{PDEs}: \quad \tfrac{\partial \boldsymbol{u}}{\partial t} + \boldsymbol{A}\tfrac{\partial \boldsymbol{U}}{\partial x} = 0 \\ &\text{ICs}: \quad \boldsymbol{U}(x,0) = \boldsymbol{U}_0(x) \\ &\text{BCs}: \quad \boldsymbol{U}(0,t) = \boldsymbol{U}_l(t), \boldsymbol{U}(L,t) = \boldsymbol{U}_r(t), \end{aligned} \tag{2.15}$$

and,

$$\begin{aligned} &\text{PDEs}: \quad \tfrac{\partial \boldsymbol{u}}{\partial t} + \tfrac{\partial \boldsymbol{F(U)}}{\partial x} = 0 \\ &\text{ICs}: \quad \boldsymbol{U}(x,0) = \boldsymbol{U}_0(x) \\ &\text{BCs}: \quad \boldsymbol{U}(0,t) = \boldsymbol{U}_l(t), \boldsymbol{U}(L,t) = \boldsymbol{U}_r(t), \end{aligned} \tag{2.16}$$

where, $\boldsymbol{U(x,t)}$ is the set of conserved variables, constant $\boldsymbol{A}$ is the coefficient matrix, $\boldsymbol{F(U)}$ is the set of fluxes, $x = 0$, $x = L$ are the boundaries.

There are a lot of schemes to solve the Riemann problem, but results show that high order Godunov schemes have essential ingredient to obtain stable solutions. Here we use the equation 2.13 to describe the second order $\sim O(\Delta x^2, \Delta t^2)$ Godunov method.

Given the general initial data $\tilde{u}(x, t^n)$ from the initial conditions, the Godunov method assumes a piecewise constant distribution of the conserved variables in each computing cell $[x_{i-1/2}, x_{i+1/2}]$ at time t^n:

$$u_i^n = \frac{1}{\Delta x} \int_{x_{i-1/2}}^{x_{i+1/2}} \tilde{u}(x, t^n) \mathrm{d}x, \tag{2.17}$$

The first order ($O(\Delta x, \Delta t)$) Godunov scheme gives,

$$\frac{u_i^{n+1} - u_i^n}{\Delta t} - a \frac{u_i^n - u_{i-1}^n}{\Delta x} = 0 \tag{2.18}$$

Then we can get the values of the variables at the next time $t^{n+1} = t^n + \Delta t$ for all computing cells,

$$u_i^{n+1} = u_i^n - \frac{\Delta t}{\Delta x}(u_i^n - u_{i-1}^n). \tag{2.19}$$

To increase the accuracy of the solution u_i^{n+1}, we can do calculation twice in each time step. First, use first order Godunov scheme for half time step $\Delta t/2$ to get some cell averages:

$$\overline{u}_i^n = u_i^n - a \frac{\Delta t}{2\Delta x}(u_i^n - u_{i-1}^n). \tag{2.20}$$

Then use the cell averages to get the values of variables at the next time t^{n+1},

$$u_i^{n+1} = u_i^n - a \frac{\Delta t}{\Delta x}(\overline{u}_i^n - \overline{u}_{i-1}^n). \tag{2.21}$$

which is of second order accuracy $O(\Delta x^2, \Delta t^2)$ and this method is called second order Godunov method.

For realistic non-linear system, the Godunov method is the same in principle, but the procedure is more complicated. The simulation code we used in the following sections is a second order Godunov-type code.

2.3 MHD Numerical Simulation Model

2.3.1 Model

We consider a rotating magnetized star surrounded by an accretion disk with a low-density, high-temperature corona above and below the disk. The disk and the corona are initially in a quasi-equilibrium state. We solve the 3D MHD equations in a reference frame rotating with the star (Koldoba et al. 2002; Romanova et al. 2004; Ustyugova et al. 2006, Long, et al. 2005, 2007), with the $z-$axis aligned with the star's rotation axis. The angular velocity of the star is $\mathbf{\Omega}$, so, $\boldsymbol{V} = \boldsymbol{v} + \boldsymbol{\omega} \times \boldsymbol{r}$, where the $\boldsymbol{V}$ is the velocity in the lab frame, the $\boldsymbol{v}$ is the velocity in the corotating frame. The MHD equations have the same form except the equation of the motion:

$$\rho \frac{\mathrm{d}\boldsymbol{v}}{\mathrm{d}t} = -\nabla p + \rho\ \boldsymbol{g} + \frac{1}{4\pi}(\nabla \times \boldsymbol{B}) \times \boldsymbol{B} + 2\rho \boldsymbol{v} \times \mathbf{\Omega} - \rho \mathbf{\Omega} \times (\mathbf{\Omega} \times \boldsymbol{R}) + \boldsymbol{F}^{vis}, \tag{2.22}$$

or,

$$\frac{\partial \rho \boldsymbol{v}}{\partial t} = -\nabla \mathcal{T} + \rho\ \boldsymbol{g} + 2\rho \boldsymbol{v} \times \mathbf{\Omega} - \rho \mathbf{\Omega} \times (\mathbf{\Omega} \times \boldsymbol{R}), \tag{2.23}$$

where $\boldsymbol{v}$ and $\boldsymbol{B}$ are vectors of velocity and magnetic field in the three-dimensional space, ρ is density, $\mathbf{\Omega}$ is the angular velocity of rotation of the star, S is the entropy per unit mass, $\boldsymbol{g}$ is the gravitational acceleration. The momentum flux-density tensor is,

$$\mathcal{T} = \rho v_i v_k + p\delta_{ik} + \left(\frac{B^2}{8\pi} \delta_{ik} - \frac{B_i B_k}{4\pi} \right) + \tau_{ik} \tag{2.24}$$

where τ_{ik} is the viscous stress. We notice the new terms of Coriolis and centrifugal forces in the equation. Using the reference frame rotating with the star we eliminate from equation large terms corresponding to the magnetic forces induced by rotation of the strong field associated with connected with rotation.

The problem of accretion to a star with magnetic fields is complicated because of high gradients of the magnetic field, $B_d \sim 1/R^3$ for the dipole and $B_q \sim 1/R^4$ for the quadrupole components and so on. To avoid this difficulty and other difficulties connected with strong magnetic field near the star, the magnetic field was decomposed into the "main" component, which is fixed and consists of the dipole and quadrupole parts: $\boldsymbol{B}_0 = \boldsymbol{B}_d + \boldsymbol{B}_q$, and variable component $\boldsymbol{B_1}$ which is induced by currents in the simulation region and is calculated in equations. This splitting helps to reduce the gradient of the magnetic field (Tanaka 1994; Powell et al. 1999).

The code is a second order Godunov-type numerical scheme (see, e.g., Toro 1999) developed earlier in our group (Koldoba et al. 2002). Viscosity is incorporated into the MHD equations in the interior of the disk so as to control the rate of matter inflow to the star. For the viscosity we used an $\alpha-$prescription with $\alpha_v = 0.04$ in all 3D simulation runs, and with smaller/larger values for testing.

2.3.2 Initial Conditions

The region considered consists of the star located in the center of coordinate system, a dense disk located in the equatorial plane and a low-density corona which occupies the rest of the simulation region. Initially, the disk and corona are in *rotational* hydrodynamic equilibrium. That is, the sum of the gravitational, centrifugal, and pressure gradient forces is zero at each point of the simulation region. The initial magnetic field is a combination of dipole and quadrupole field components which are force-free at $t = 0$. The initial rotational velocity in the disk is close to, but not exactly, Keplerian (i.e., the pressure gradient is taken

into account). The corona at different cylindrical radii r rotates with angular velocities corresponding to the Keplerian velocity of the disk at this distance r. This initial rotation is assumed so as to avoid a strong initial discontinuity of the magnetic field at the boundary between the disk and corona. The distribution of density and pressure in the disk and corona and the complete description of these initial conditions is given in Romanova et al. (2002) and Ustyugova et al. (2006).

The initial accretion disk extends inward to an inner radius r_d and has a temperature T_d which is much less than the corona temperature $T_d = 0.01T_c$. The density of the corona is 100 times less than the density of the disk, $\rho_c = 0.01\rho_d$. These values of T_c, T_d, ρ_c, ρ_d are specified at the disk-corona boundary near the inner radius of the disk.

After the beginning of the rotation, the magnetic field lines start to twist and the exact force-balance is disturbed because the magnetic forces begin to act. However, these forces are not strong enough to disturb the disk significantly. The accretion rate increases only slightly as a result of the magnetic braking associated with this initial twist. These initial conditions allow an investigation of accretion to a star with a dipole magnetic field for conditions where the disk matter accretes inward very slowly on the viscous time-scale. The $\alpha-$ viscosity incorporated in our code permits the regulation of the accretion rate. Earlier, we used these initial conditions to investigate magnetospheric flow in case of a pure dipole intrinsic field (Romanova et al. 2002, 2004).

2.3.3 Boundary Conditions

At the inner boundary ($r = R_*$), where R_* is the radius of the star, boundary conditions are applied to the density $\partial\rho/\partial r = 0$, pressure $\partial p/\partial r = 0$, entropy $\partial S/\partial r = 0$, velocity $\partial(\mathbf{v} - \mathbf{\Omega} \times \mathbf{R})/\partial r = 0$ and the magnetic field, $\partial B_\theta/\partial r = 0$, $\partial B_\phi/\partial r = 0$. The $r-$component of the magnetic field satisfies $\partial(r^2 B_r)/\partial r = 0$. The matter flow is frozen to the strong magnetic field so that we have $(\mathbf{v} - \mathbf{\Omega} \times \mathbf{R}) \parallel \mathbf{B}$. At the outer boundary, free boundary conditions are taken for all variables with the additional condition that matter is not permitted to flow in through the outer boundary. The investigated numerical region is large, $\sim 45R_*$, so that the initial reservoir of matter in the disk is large and sufficient for the performed simulations. Matter flows slowly inward from the external regions of the disk. During the simulation times studied here only a small fraction of the total disk matter accretes to the star.

2.3.4 Grids

The Grid Used in 2.5D Simulations: Spherical Grid

In 2.5D MHD simulations, we use the inhomogeneous spherical grid with $N_r \times N_\theta$ cells in the region $r_{in} < r < r_{out}$, $0 < \theta < \pi/2$, where $r_{in} = 0.35$ is the radius of the star, the inner boundary of the simulation region, r_{out} is the external boundary of the simulation region. N_r means the number of steps in r direction, N_θ means the number of steps in θ direction. The grid equally separates the whole region in θ direction and chooses the radial steps so that the poloidal cells are curvilinear rectangles with the size of $\Delta r = r\Delta\theta$. Figure 2.1 shows the grid with a resolution

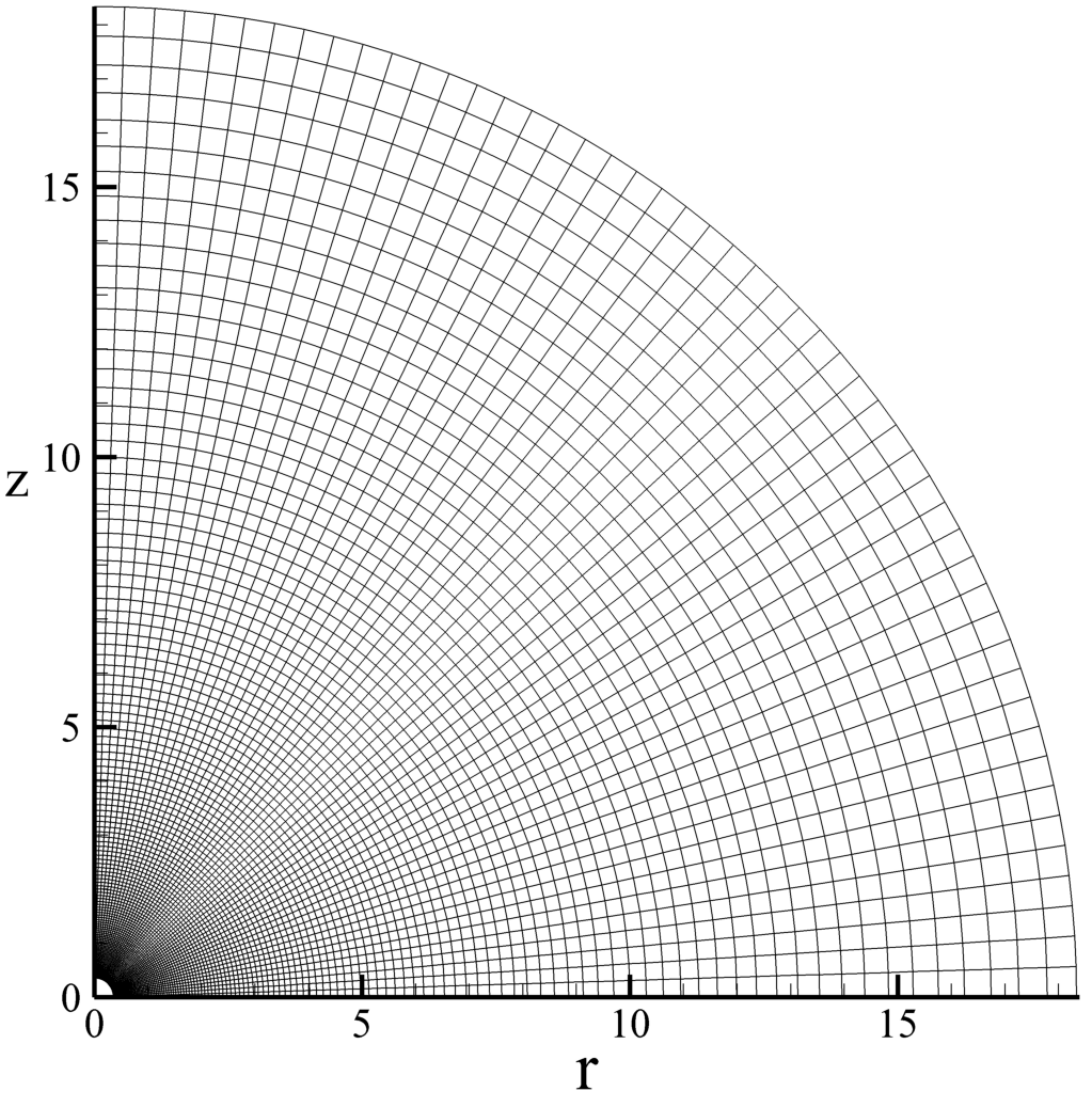

Figure 2.1: Sample grid of spherical coordinates used in 2.5D simulations with a resolution of $N_r \times N_\theta = 131 \times 51$. Subscripts donates the r and θ directions respectively. The radius of the star is $r_* = 0.35$. The size of each grid cell is about $\Delta r \sim r\Delta\theta$, which gives higher resolution close to the star.

of $N_r \times N_\theta = 131 \times 51$. We can see this grid gives better resolution in the region close to the star, where we have more interest. The number of steps in r direction determines the size of the simulation region, for example, the external boundary r_{out} is about 157 times of the radius of the star for above grid. We choose big N_r to minimize the influence of the external boundary on the vicinity of the star.

The Grid Used in 3D Simulations: Cubed Sphere Grid

A special *cubed* sphere grid (Koldoba et al. 2002) is used in 3D MHD simulations, which takes advantages of both Cartesian coordinate and spherical coordinate, but overcome the difficulty of singularity in spherical coordinate. The grid consists of N_r concentric spheres, where each sphere represents an inflated cube and the radii of next spheres should be $r_{i+1}/r_i = const. > 1$. Each sphere consists of six identical sectors corresponding to the six sides of the cube, and an $N \times N$ grid of curvilinear cartesian coordinates is introduced in each sector. Thus, the whole simulation region consists of six blocks with $N_r \times N^2$ cells. In the current simulations we chose a grid resolution of 75×31^2. Other resolutions were also investigated for comparison. The coarser grids give satisfactory results for a pure dipole field. However, for a quadrupole field, the code requires a finer grid because of the higher magnetic field gradients.

Figure 2.2 shows the homogeneous cubed sphere grid in the whole simulation region, which has six identical sectors. We can see it has better resolution close to the star.

Figure 2.3 shows the inhomogeneous cubed sphere grid in the whole simulation region, which has two big identical sectors with coarse resolution in the

corona region, and has four small identical sectors with much higher resolution in the disk region.

2.3.5 Reference Units:

We solve the MHD equations using dimensionless variables: distance $\widetilde{R} = R/R_0$, velocity $\widetilde{v} = v/v_0$, time $\widetilde{t} = t/P_0$, etc. The subscript "0" denotes a set of reference (dimensional) values for variables, which are chosen as follows: $R_0 = R_*/0.35$, where R_* is the radius of the star; $v_0 = (GM/R_0)^{1/2}$; time scale $P_0 = 2\pi R_0/v_0$. Other reference values are: angular velocity $\Omega_0 = v_0/R_0$; magnetic field $B_0 = B_{*0}(R_*/R_0)^3$, where B_{*0} is the reference magnetic field on the surface of the star; dipole magnetic moment $\mu_0 = B_0 R_0^3$; quadrupole moment $D_0 = B_0 R_0^4$; density $\rho_0 = B_0^2/v_0^2$; pressure $p_0 = \rho_0 v_0^2$; mass accretion rate $\dot{M}_0 = \rho_0 v_0 R_0^2$; angular momentum flux $\dot{L}_0 = \rho_0 v_0^2 R_0^3$; energy per unit time $\dot{E}_0 = \rho_0 v_0^3 R_0^2$ (the radiation flux J is also in units of $\dot{E}_0$); temperature $T_0 = \mathcal{R} p_0/\rho_0$, where $\mathcal{R}$ is the gas constant; and the effective blackbody temperature $T_{\rm eff,0} = (\rho_0 v_0^3/\sigma)^{1/4}$, where σ is the Stefan-Boltzmann constant.

In the subsequent chapters and figures, we show dimensionless values for all quantities and drop the tildes (~). To obtain the real dimensional values of variables, one needs to multiply the dimensionless values by the corresponding reference units. Our dimensionless simulations are applicable to different astrophysical objects with different scales. For convenience, we list the reference values for typical CTTSs, cataclysmic variables, and millisecond pulsars in Table 2.1.

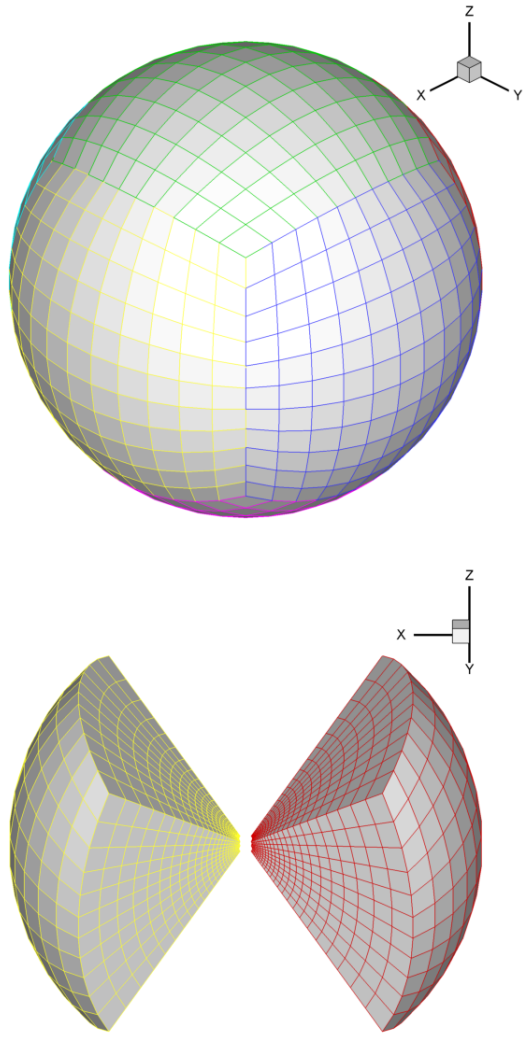

Figure 2.2: Sample homogeneous cubed sphere grid used in 3D simulations. The coordinate separates the space by six identical sectors, and each has a resolution of $N_r \times N^2 = 24 \times 11^2$. N_r means the number of grid cells in r direction, N means the number of grid cells in each cocentric sphere in each sector. The radius of the star is $r_* = 0.35$. The coordinates have higher resolution close to the star. Top panel: all sectors. Bottom panel: two of sectors.

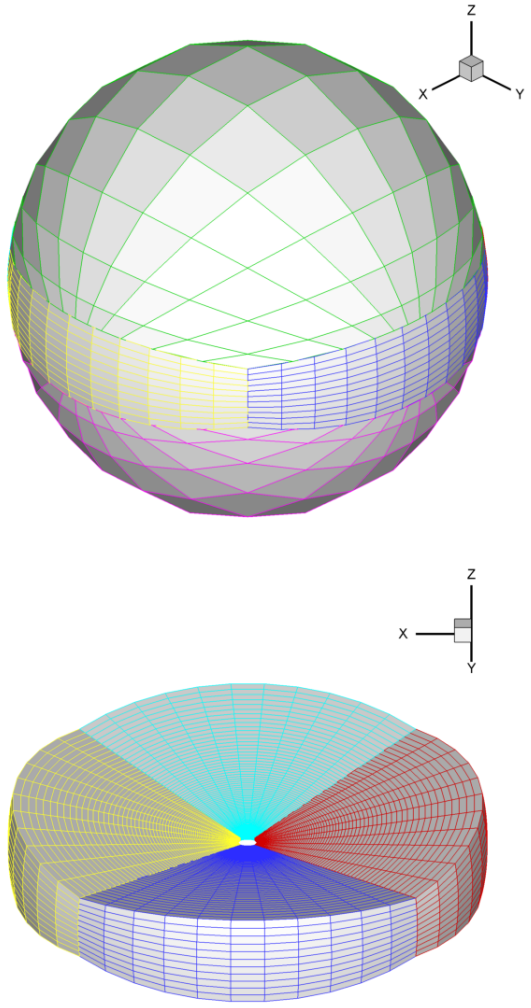

Figure 2.3: Sample inhomogeneous cubed sphere grid used in 3D simulations. The coordinate separates the space by four identical sectors near the equatorial plane and two sectors in the other region. Each sector has a resolution of $N_r \times N^2 = 24 \times 11^2$. N_r means the number of grid cells in r direction, N means the number of grid cells in each cocentric sphere in each sector. The radius of the star is $r_* = 0.35$. The coordinates have higher resolution in the disk than in the corona, especially in the inner region of the disk. Top panel: all sectors. Bottom panel: four sectors in the disk region.

	CTTSs	White dwarfs	Neutron stars
$M_*(M_\odot)$	0.8	1	1.4
R_*	$2R_\odot$	5000 km	10 km
B_{*0} (G)	10^3	10^6	10^9
R_0 (cm)	4×10^{11}	1.4×10^9	2.9×10^6
v_0 (cm s^{-1})	1.6×10^7	3×10^8	8.1×10^9
Ω_0 (s^{-1})	4×10^{-5}	0.2	2.8×10^3
P_0	1.5×10^5 s 1.8 days	29 s	2.2 ms
B_0 (G)	43	4.3×10^4	4.3×10^7
ρ_0 (g cm^{-3})	7×10^{-12}	2×10^{-8}	2.8×10^{-5}
p_0 (dy cm^{-2})	1.8×10^3	1.8×10^9	1.8×10^{15}
$\dot{M}_0$ (g s^{-1})	1.8×10^{19}	1.2×10^{19}	1.9×10^{18}
$\dot{M}_0$ ($M_\odot$yr^{-1})	2.8×10^{-7}	1.9×10^{-7}	2.9×10^{-8}
$\dot{L}_0$ (g cm^{2}s^{-2})	1.15×10^{18}	4.9×10^{36}	4.5×10^{34}
T_0 (K)	1.6×10^6	5.6×10^8	3.9×10^{11}
$\dot{E}_0$ (erg s^{-1})	4.8×10^{33}	1.2×10^{36}	1.2×10^{38}
$T_{\rm eff,0}$ (K)	4800	3.2×10^5	2.3×10^7

Table 2.1: Sample reference units used in simulations for typical CTTSs, cataclysmic variables, and millisecond pulsars. Real dimensional values for variables can be obtained by multiplying the dimensionless values of variables shown in this paper by these reference units, i.e., Real Dimensional Values = Dimensionless Values × Reference Units.

CHAPTER 3

LOCKING OF THE ROTATION OF DISK ACCRETING MAGNETIZED STARS*

We investigate the rotational equilibrium state of a disk accreting magnetized stars using axisymmetric MHD simulations. In this "locked" state, the spin-up torque balances the spin-down torque so that the net average torque on the star is zero. We investigated two types of initial conditions, one with a relatively weak stellar magnetic field and high coronal density, and the other with a stronger stellar field and a lower coronal density. We observed that for both initial conditions the rotation of the star is locked to the rotation of the disk. In the second case, the opened field lines carry significant angular momentum out of the star. However, this did not appreciably change the condition for locking of the rotation of the star. We find that in the equilibrium state the corotation radius r_{co} is related to the magnetospheric radius r_A as $r_{co}/r_A \approx 1.2 - 1.3$ for case (1) and $r_{co}/r_A \approx 1.4 - 1.5$ for case (2). We estimated periods of rotation in the equilibrium state for classical T Tauri stars, dwarf novae and X-ray millisecond pulsars.

3.1 Introduction

Disk accretion to a rotating star with a dipole magnetic field is important in a number of astrophysical objects, including T Tauri stars (Camenzind 1990; Königl 1991), X-ray pulsars (Nagase 1989; Bildsten et al. 1997), and cataclysmic variables (Warner 1995). An important property of this interaction is the disrup-

*This chapter is based on the published paper by Long et al. 2005, the Astrophysical Journal, 634, 1214. It is rewritten here with minor changes.

tion of the disk at the Alfvén radius, r_A, and the "locking" of the star's angular rotation at an angular velocity, Ω_{eq}, which is expected to be of the order of the disk rotation rate at the Alfvén radius, $\Omega(r_A) = (GM/r_A^3)^{1/2}$. However, the exact conditions for locking and for the value of the equilibrium rotation rate Ω_{eq} (when the star does not spin up or spin down) were not been established.

One of the complicated aspects of the disk-magnetosphere interaction is the process of angular momentum transport between the disk and the magnetized star. In the first models of the disk-magnetosphere interaction it was proposed that the magnetic field has a dipole configuration everywhere and that the net change between spin-up torque which arises from the magnetic connection of the star to the disk within the corotation radius r_{co} and the spin-down torque which arises from the connection beyond the corotation radius determines the spin evolution of the star (Ghosh, Lamb & Pethick 1977; Ghosh & Lamb 1978, 1979 - hereafter GL79). The corotation radius is the radius where the disk rotates at the same speed as a star, $r_{co} = (GM/\Omega_*^2)^{1/3}$. It was suggested that for a particular value of the star's rotation rate, Ω_{eq}, the positive spin-up torque balances the negative spin-down torque and the star is in the rotational equilibrium state (Ghosh & Lamb 1978, 1979; Wang 1995).

Recent studies of the evolution of the magnetic field threading the disk and the star led to understanding that the field tends to be inflated and possibly opened due to the difference in the angular velocities of the foot-points (Lovelace, Romanova & Bisnovatyi-Kogan 1995 - hereafter LRBK; Shu et al. 1994; Bardou 1999, Uzdensky, Königl & Litwin 2002). In this case a star may lose some angular momentum through the open field lines and the equilibrium state will be determined by the balance between processes of spin-up/spin-down as-

sociated with the disk-magnetosphere interaction, and spin-down associated with the open field lines.

In some models it was suggested that the angular momentum transport between the star and the disk may be much less efficient (Agapitou & Papaloizou 2000) if the field lines are opened as proposed by LRBK. Under such conditions the rotational equilibrium state will be quite different (e.g., Matt & Pudritz 2004, 2005). The goal of this paper is to derive the conditions for the rotational equilibrium state using axisymmetric MHD simulations of the disk-magnetosphere interaction.

The properties of the rotational equilibrium state depend on the configuration of the magnetic field threading the star and the disk. Consequently, analysis of this problem requires two or three dimensional simulations. Axisymmetric simulations have shown that the field lines do open (Hayashi et al. 1996; Miller & Stone 1997; Hirose et al. 1997; Romanova et al. 1998; Fendt & Elstner 1999). However, longer runs have shown that the innermost field lines reconnect to form a closed magnetosphere, and some of them open and close again in a recurrent manner (Goodson & Winglee 1997; Goodson, Winglee & Böhm 1999; Romanova et al. 2002, hereafter RUKL; Romanova et al. 2004; Kato et al. 2004, Von Rekowski & Brandenburg 2004). Detailed simulations of the slow, viscous disk accretion to a rotating star with an aligned dipole field (RUKL) have shown that on long time-scales, the magnetic field lines in the vicinity of the Alfvén radius r_A are closed or only partially open, and these lines are important for the angular momentum transport between the star and the disk. The balance between the magnetic flux in closed and open field lines is clearly important for determining the rotational equilibrium state.

In RUKL, a preliminary search for the conditions of torqueless accretion was performed and the torqueless accretion was shown to exist. In this paper, we give a detailed study of the conditions for torqueless accretion using an improved axisymmetric MHD code which makes possible longer simulation runs compared to RUKL. The main question is: What is the angular rotation rate of a star Ω_{eq} for the torqueless accretion given the star's mass M, magnetic moment μ, and accretion rate $\dot{M}$. Equivalently, if we know the Alfvén radius r_A, then what is the corotation radius r_{co} in the rotational equilibrium state? In earlier theoretical models, it was estimated that the critical fastness parameter

$$\omega_s = \Omega_*/\Omega_K(r_A) = (r_A/r_{co})^{3/2} \tag{3.1}$$

of the equilibrium state is in the range of $0.47-0.95$ (Li & Wickramasinghe 1997). This corresponds to the ratio $r_{co}/r_A \sim 1.1 - 1.7$.

In this chapter we determine the value of r_{co}/r_A for torqueless accretion numerically by performing a large set of numerical simulations for different values of Ω_*, μ, $\dot{M}$, and disk/corona parameters. We also investigated the matter flow and the angular momentum transport in the equilibrium state. We focus on conditions where the torqueless accretion occurs and study its dependence on different physical parameters for different cases in §3.3 and 3.4. In §3.5, we apply our results to relevant objects, such as CTTSs, cataclysmic variables, and X-ray millisecond pulsars. We give discussion in §3.6.

3.2 Theoretical Ideas and Numerical Simulations

Theoretical aspects of the disk-magnetoshpere interaction were developed in the 1970s (e.g. Pringle & Rees, 1972; Ghosh, Lamb & Pethick 1977; GL79). As

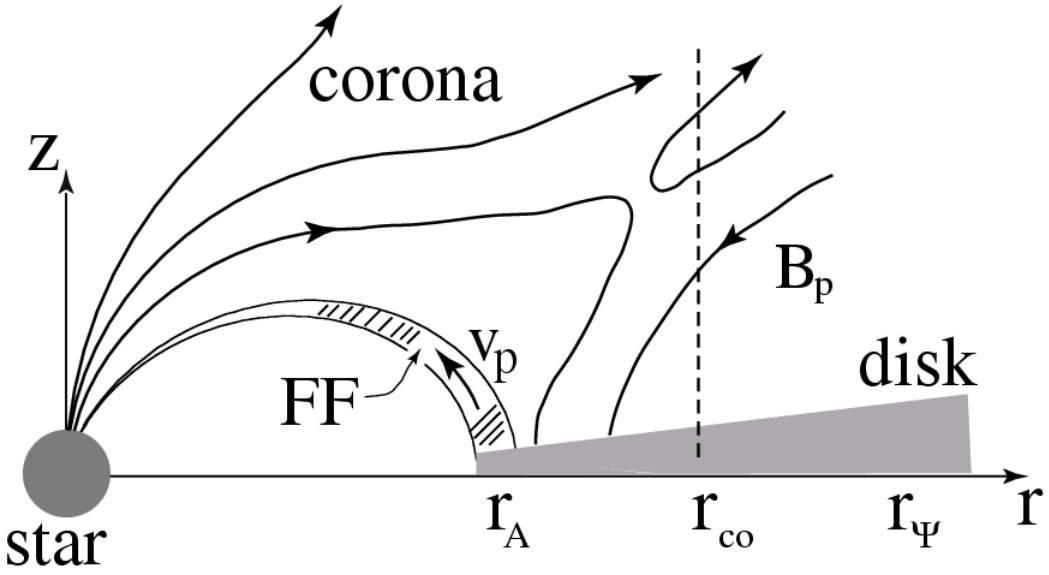

Figure 3.1: Sketch of disk accretion to a star with an aligned dipole magnetic field, where r_A is the Alfvén radius, r_{co} is corotation radius, r_Ψ is the deviation radius where a significant deviation from Keplerian rotation occurs for $r < r_\Psi$ due to the magnetic force on the disk. The dashed line divides the rapidly rotating region and the slowly rotating region. FF denotes the funnel flow.

sketched in Figure 3.1, the initial Keplerian accretion disk is threaded by the star's magnetic field. The inner radius of the disk, referred to as the Alfvén radius r_A, occurs at the radial distance where the energy-density of matter in the disk equals to magnetic energy-density, or where the paramter (e.g., Lamb, Pethick & Pines 1973; Davidson & Ostriker 1973),

$$\beta = \frac{p + \rho v^2}{(B^2/8\pi)} = 1. \tag{3.2}$$

We observed from many simulations that the inner radius of the disk coincides with this radius. The Alfvén radius is usually derived analytically using a

number of approximations. For a dipole magnetic field of the star, $\mu \equiv B_* R_*^3 = B r^3$,

$$r_A = k_A r_A^{(0)} = k_A \frac{\mu^{4/7}}{(2GM)^{1/7} \dot{M}^{2/7}} \ . \tag{3.3}$$

Here, G is the gravitational constant, $\dot{M}$ is the mass accretion rate, M is the mass of the star, $r_A^{(0)}$ is the Alfvén radius for the spherical accretion (Elsner & Lamb 1977). The coefficient k_A accounts for the fact that the disk accretion is different from spherical accretion. Using values of the different parameters obtained from our simulations we obtained $r_A^{(0)}$ and then compared it with r_A. From this we obtained $k_A \approx 0.5$.

In a somewhat different approach, Wang (1995) suggested that the disk stops or disrupts at the radius r_0 where the magnetic and matter stresses are equal,

$$(-r^2 B_\phi B_z)_0 = \dot{M} [\mathrm{d}(r^2 \Omega)/\mathrm{d}r]_0, \tag{3.4}$$

where the 0−subscripts indicate evaluation at $r = r_0$, B_ϕ and B_z are the components of the magnetic field, Ω is the angular velocity of the disk. We took values of parameters from our simulations and derived the radius the radius r_0. We observed that this radius approximately coincides with r_A.

Whether a star spins up or spins down is due to angular momentum flow to or out of the star transported by the matter flow and the magnetic field. Some field lines of the star thread the disk and transport angular momentum between the disk and the star (e.g., GL79). Other field lines are inflated and become open, that is, not connected to the disk. These open field lines may transport angular momentum away from the star to the corona without direct interaction with the disk (Agapitou & Papaloizou 2000; Matt & Pudritz 2004). We observed that both closed and open field lines contribute to the angular momentum transport to the star.

For the case where the poloidal field lines connect the star and the disk, the field lines passing through the disk within the corotation radius r_{co} spin up the star, while the field lines passing through the disk at large distances spin it down (GL79). The dashed vertical line in Figure 3.1 at r_{co} divides the regions which provide positive and negative torques. There is also a region $r \lesssim r_\Psi$ where the magnetic interaction modifies the Keplerian rotation of the disk, and where the angular momentum transport between the star and the disk is important (GL79, RUKL). If some of the magnetic field lines are open, then angular momentum may be also transported outward from the disk and from the star through twisting of open magnetic field lines. Thus part of the angular momentum flux may be transported by the matter flow, part by the open field lines, and part by closed field lines connecting the star and the disk.

In order to investigate the rotational equilibrium states, we performed simulations with two types of initial conditions, type I and type II. For type I initial conditions we have a magnetic field which is relatively weak, $\mu = 2$, the disk is relatively thick with fiducial density $\rho_d = 1$, and relatively high coronal density, $\rho_{cor} = 0.005$. The initial inner disk radius is $r_d = 6$. The outer radius of the simulation domain corresponds to $18R_0$, that is, about $54R_*$. Results for this case are described in §3.3. For type II initial conditions the star's magnetic field is much stronger, $\mu = 10$, the coronal density is much lower $\rho_{cor} = 0.001$, the disk is thinner, and the initial inner disk radius is $r_d = 5$. The outer radius of the simulation domain corresponds to $68R_0$, that is, about $136R_*$. These initial conditions, which are more favorable for inflation and opening of the coronal field lines, are described in §3.4.

3.3 The Equilibrium State of Disk Accretion for Initial Conditions of Type I

3.3.1 Search for Rotational Equilibrium State

Whether the star spins up or spins down is determined by the net flux of angular momentum to the surface of the star, $\dot{L}$. This flux is composed of two parts, the flux carried by the matter, $\dot{L}_m$, and that carried by the magnetic field, $\dot{L}_f$:

$$\dot{L} = \dot{L}_m + \dot{L}_f \ , \tag{3.5}$$

$$\dot{L}_m = -\int \mathrm{d}\mathbf{S} \cdot \rho r v_\phi \mathbf{v}_p \ , \tag{3.6}$$

$$\dot{L}_f = \frac{1}{4\pi} \int \mathrm{d}\mathbf{S} \cdot r B_\phi \mathbf{B}_p \ , \tag{3.7}$$

where the $p-$subscript denotes the poloidal component, and $\mathrm{d}\mathbf{S}$ is the outward pointing surface area element of the star. We performed a set of simulations for different angular velocities of the star, Ω_*, to find the critical value of Ω_*, corresponding to the rotational equilibrium state, that is, the state when $\dot{L} \approx 0$. Other parameters $(\dot{M}, \mu)$ were fixed.

We observed that $\dot{L}_f$ is always dominant over $\dot{L}_m$ for all cases (as in RUKL) and thus we compared $\dot{L}_f$ for these cases. This was predicted in earlier theoretical research (e.g., GL79). We narrowed the set of Ω_* (or, r_{co}) values so that $\dot{L}_f$ was very small on average (see Figure 3.2a). Among these we picked the ones for which $\dot{L}_f \approx 0$ that is those corresponding to the rotational equilibrium state, $\Omega_* = \Omega_{eq}$. We found that equilibrium state corresponds to values $(r_{co})_{eq} \approx 1.7 - 1.8$.

In addition, we calculated matter flux to the star,

$$\dot{M} = -\int d\mathbf{S} \cdot \rho \mathbf{v}_p. \tag{3.8}$$

Figure 3.2b shows the mentioned fluxes in the rotational equilibrium state. Note that this state is typically reached at $T > 50$ because initially the disk is far from the magnetosphere and it takes time for the disk to move inward. One can see that the angular momentum flux carried by the field $\dot{L}_f$ fluctuates around zero.

3.3.2 Disk-Magnetosphere Interaction in Equilibrium State

We now discuss in more detail the rotational equilibrium state where $r_{co} = 1.7$. Figure 3.3a shows the evolution of matter and the magnetic flux with time. One can see that initially the disk matter moves inward, then it stops near magnetosphere and goes to the star through a funnel flow which is driven up by pressure gradient force (RUKL; Koldoba et al. 2002). The funnel flow is quasi-stationary after a time $t \sim 50$. The bold red line divides the regions where magnetic and matter energy densities dominate, that is, the line where $\beta = 1$. The corresponding Alfvén radius is $r_A \approx 1.2 - 1.3$. We also estimated the radius r_0 derived from the equality of magnetic and matter stresses. We observed that this radius is close to r_A, $r_0 \approx 1.3 - 1.4$.

Figure 3.3a shows that the magnetic field for $r > r_A$ is strongly non-dipolar, and the structure of the field is complicated. The magnetic field lines initially inflate for $T < 30$; however, later some of them reconnect forming closed field lines and thus enhancing the dipole component in the closed magnetosphere.

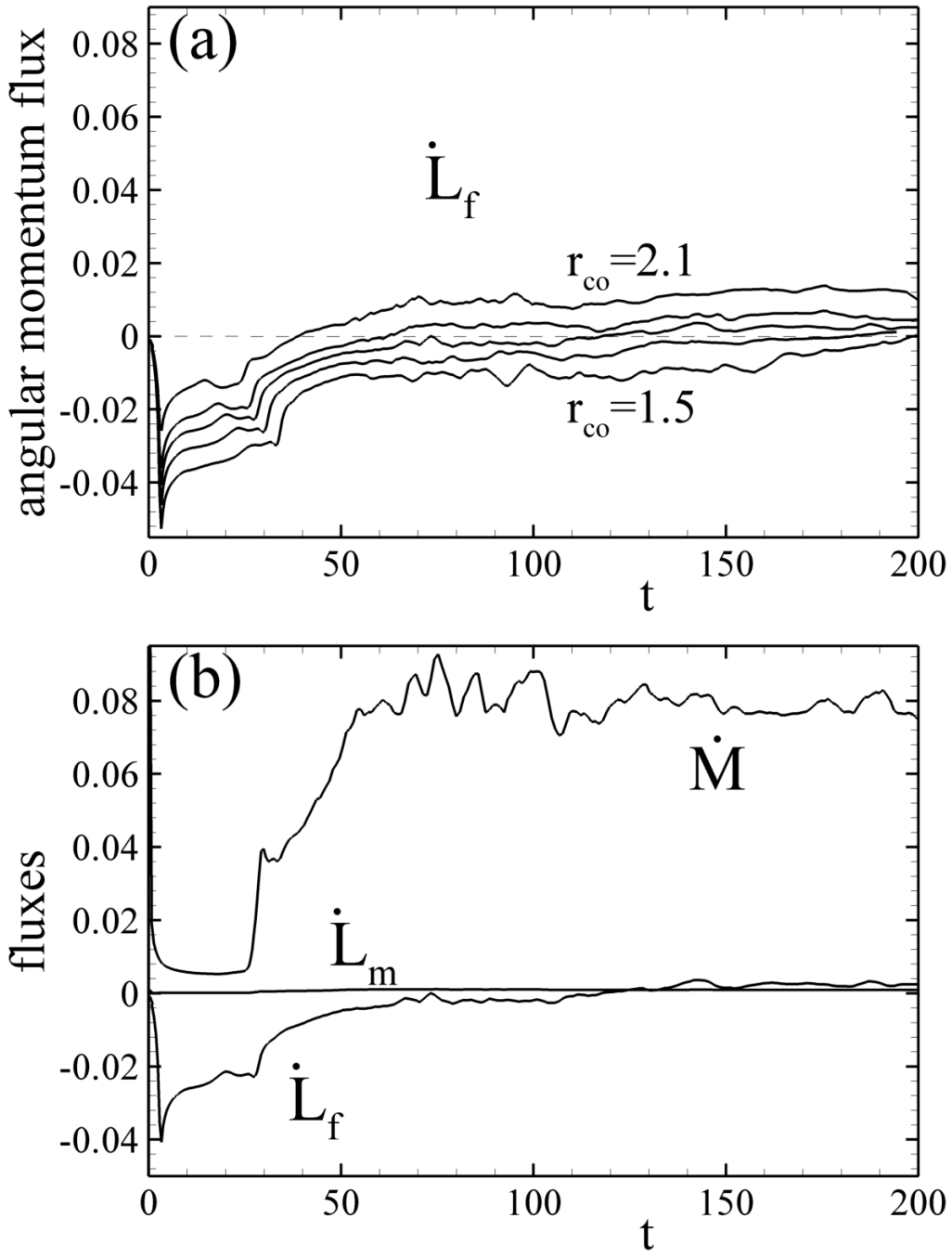

Figure 3.2: (a) The evolution of $\dot{L}_f$ for different corotation radii r_{co} = 1.5, 1.6, 1.7, 1.8, 2.1; (b) The evolution of $\dot{M}$ and the angular momentum fluxes carried by matter $\dot{L}_m$ and the magnetic field $\dot{L}_f$ in rotational equilibrium state, $r_{co} \approx 1.7$. Time scale is P_0.

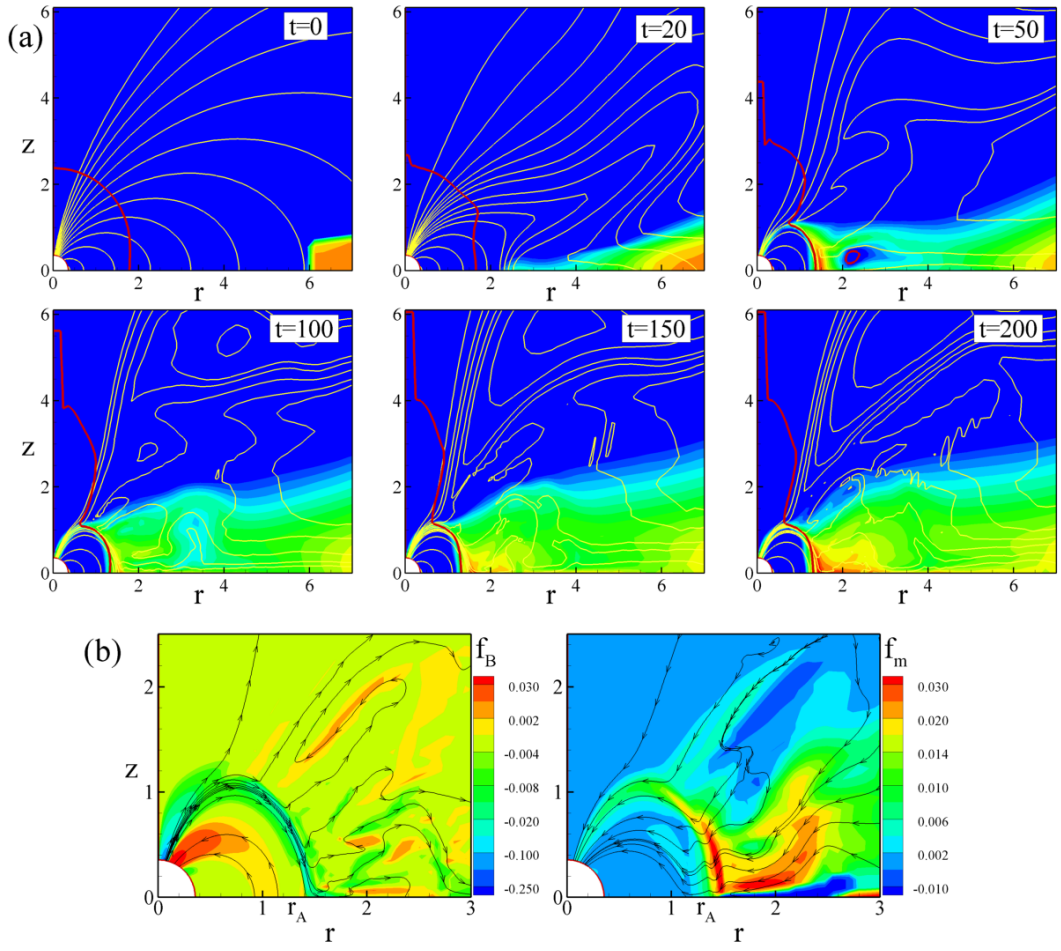

Figure 3.3: (a). Evolution of the density (color background), and the magnetic field (yellow lines) in rotational equilibrium state for type I initial conditions for $t = 0 - 200$ rotations. The density changes from $\rho = 2$ in the disk to $\rho = 0.005$ in the corona. The bold red line corresponds to $\beta = 1$. (b). Fluxes of angular momentum carried by magnetic field $\mathbf{f}_B$ (left panel) and by matter $\mathbf{f}_m$ (right panel) at $t = 200$. Color background shows value of the fluxes, the streamlines with arrows - the direction of the angular momentum flow.

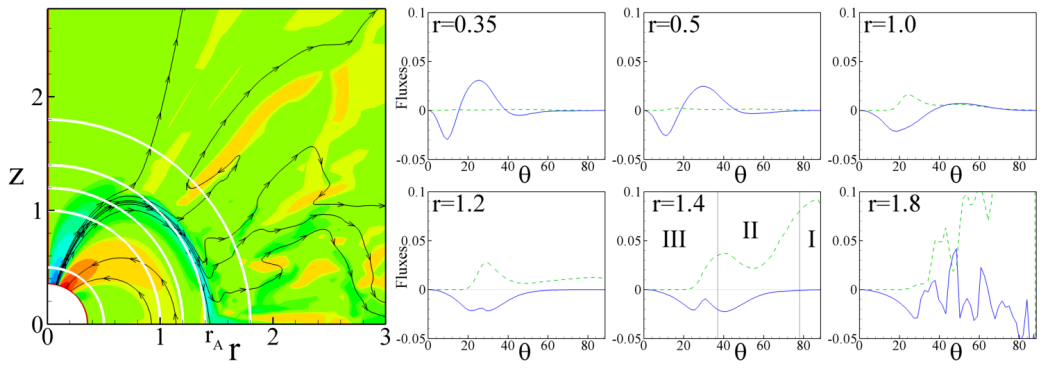

Figure 3.4: Angular distribution of fluxes for type I initial conditions. The left-hand panel shows radii along which the angular momentum fluxes are calculated. The right-hand panel shows the angular momentum fluxes carried by the magnetic field $F_B(r,\theta)$ (solid lines) and the matter $F_m(r,\theta)$ (dashed lines) at different radii r. The numbers show the regions where the angular momentum flux carried by the field is carried mostly by the closed (I), radial (II), or open (III) field lines.

Other field lines, which are near the axis stay open and represent the lines of "magnetic tower", which is often observed in different simulations of the disk-magnetosphere interaction (e.g., Kato et al. 2004; Romanova et al. 2004). Many field lines are radially stretched by the accreting matter. These field lines are located in the disk and above the disk. Most of these field lines are connected to the star. The field lines above the closed magnetosphere continue to open and reconnect in quasi-periodic manner. In case of the lower density corona, inflation is more efficient, and this leads to larger quasi-periodic oscillations of the magnetic flux and associated fluxes.

We analyzed the angular momentum transport between the star and the disk and corona. Figure 3.3b shows the distribution of the angular momentum

fluxes carried by the field $\mathbf{f}_B = rB_\phi \mathbf{B}_p/4\pi$ (left panel) and carried by the matter $\mathbf{f}_m = -\rho r v_\phi \mathbf{v}_p$ (right panel). One can see that for $r > r_A$, most of the angular momentum flux is carried by the matter (see the region with the high positive angular momentum at the right panel). However, for $r \lesssim r_A$ it is mainly transported by the magnetic field (see left panel of Figure 3.3b). The streamlines in the Figure 3.3b show direction of the flow of angular momentum. One can see that matter always carries positive angular momentum towards the star, which tends to spin up the star. Magnetic field lines carry angular momentum out of the star through the field lines threading the area of the funnel flow and corona. The situation with the angular momentum transport seems to be more complicated compared to one described by GL79.

The angular momentum fluxes change with distance and with angle. We calculated the angular distribution of fluxes

$$F_B(r,\theta) = 2\pi r^2 \sin\theta \mathbf{f}_B \cdot \hat{r} \tag{3.9}$$

and

$$F_m(r,\theta) = 2\pi r^2 \sin\theta \mathbf{f}_m \cdot \hat{r} \tag{3.10}$$

through the spheres of different radii r. Figure 3.4 shows that at a large radius, $r = 1.8$, matter carries most of the angular momentum, while the magnetic field also contributes but with the opposite sign. At smaller radii, the fluxes become smaller and the largest flux is in the region of the funnel flow. At the surface of the star, the flux associated with matter is very small. The flux associated with the field has two components of the opposite sign which cancel each other approximately.

The distribution of angular momentum flux is more complicated compared to that of theoretical models. However, the equilibrium state does exist and the

ratio r_{co}/r_A is not very much larger than unity. This means that the rotation of the star is efficiently locked to the rotation of the inner regions of the disk.

One can see from Figure 3.3a, that a significant part of the disk is disturbed by the disk-magnetosphere interaction. Figure 3.5 shows the distribution of the angular velocity of the disk in the equatorial plane. We observed that the angular velocity varies around the Keplerian value and is usually slightly smaller then Keplerian. The magnetic field is strongly wound up in the disk so that the azimuthal field dominates. The inner regions of the disk $r \lesssim r_\Psi \sim 4$ are appreciably influenced by the magnetic field.

3.3.3 Dependence on μ and α

Next, we took a star in a state at $r_{co} = 1.8$, which is close to rotational equilibrium state, and varied the magnetic moment of the star μ. Figure 3.3.3a shows that when μ increases, the rate of change of angular momentum of the star becomes more negative, that is a star spins-down. This is connected with the fact that for larger μ, the magnetosphere is larger and the flux of the positive angular momentum to the star is smaller than in the equilibrium state. For example, for $\mu = 4$, the inner disk radius is at $r_A \approx 1.6$. At this inner radius, the disk rotates much slower than the star and a star strongly spins down. Roughly, the dependence is

$$\dot{L}_f \sim -0.02\mu + 0.04. \tag{3.11}$$

The balance between spin-up and spin-down torques is similar to that suggested by the GL79 model, where positive and negative torques are associated with regions within and beyond the corotation radius. We also observed dif-

ferent regions contributing positive and negative angular momentum fluxes. However now the distribution of the external to the Alfvén surface field lines is more complicated.

We calculated the average value of r_A for each μ and obtained the dependence $r_A \sim \mu^\kappa$, with $\kappa = 0.36$. This coefficient κ is somewhat different from that of equation 3.3 where $k = 4/7 \approx 0.57$. The difference may be connected with the fact that in the theoretical analysis the magnetic field is assumed to be a pure dipole field everywhere, whereas the simulations show that the actual field is different from a dipole for $r \gtrsim r_A$. In this and all above simulations, the viscosity coefficient was fixed at the value $\alpha = 0.02$.

We also performed simulation runs for different values of the disk viscosity, $\alpha = 0,\ 0.01,\ 0.02$, and 0.03, with other parameters fixed. We observed that for larger α the accretion rate is larger, and the Alfvén radius r_A is smaller. Thus, the region of positive torque becomes larger than the region of negative torque, and $\dot{L}_f$ is larger. In other words, at a higher accretion rate $\dot{M}$, incoming matter brings more of positive angular momentum, which is transferred to larger angular momentum flux carried by the field $\dot{L}_f$. The angular momentum flux increases with α (see Figure 3.3.3b) as about

$$\dot{L}_f \sim \alpha^{1.9} \quad (\alpha \geq 0.01). \tag{3.12}$$

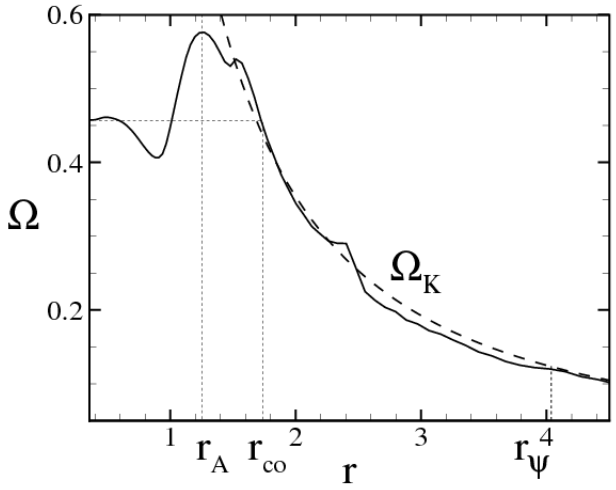

Figure 3.5: Radial distribution of angular velocity of the disk along in the equatorial plane at $t = 180$. The dashed line shows Keplerian angular velocity.

3.4 Equilibrium State of Disk Accretion for Initial Conditions of Type II

Here we consider another case corresponding to quite different initial conditions referred to as type II. This case has a stronger magnetic field, $\mu = 10$, and a much lower coronal density, $\rho_{cor} = 0.001$. The density in the corona influences the evolution of the magnetic field in the corona, namely, the inflation and opening of the magnetic field lines is favored. As discussed earlier, the angular momentum transport between the disk and star occurs in part through the magnetic field. In addition, we took a different structure of the disk, which is thinner and located initially at $r_d = 5$, which is closer to the star for such a strong field. We were able to model the stronger magnetic field because we increased the radius of the star (the inner boundary) to $R_* = 0.5$ (versus $R_* = 0.35$ in other

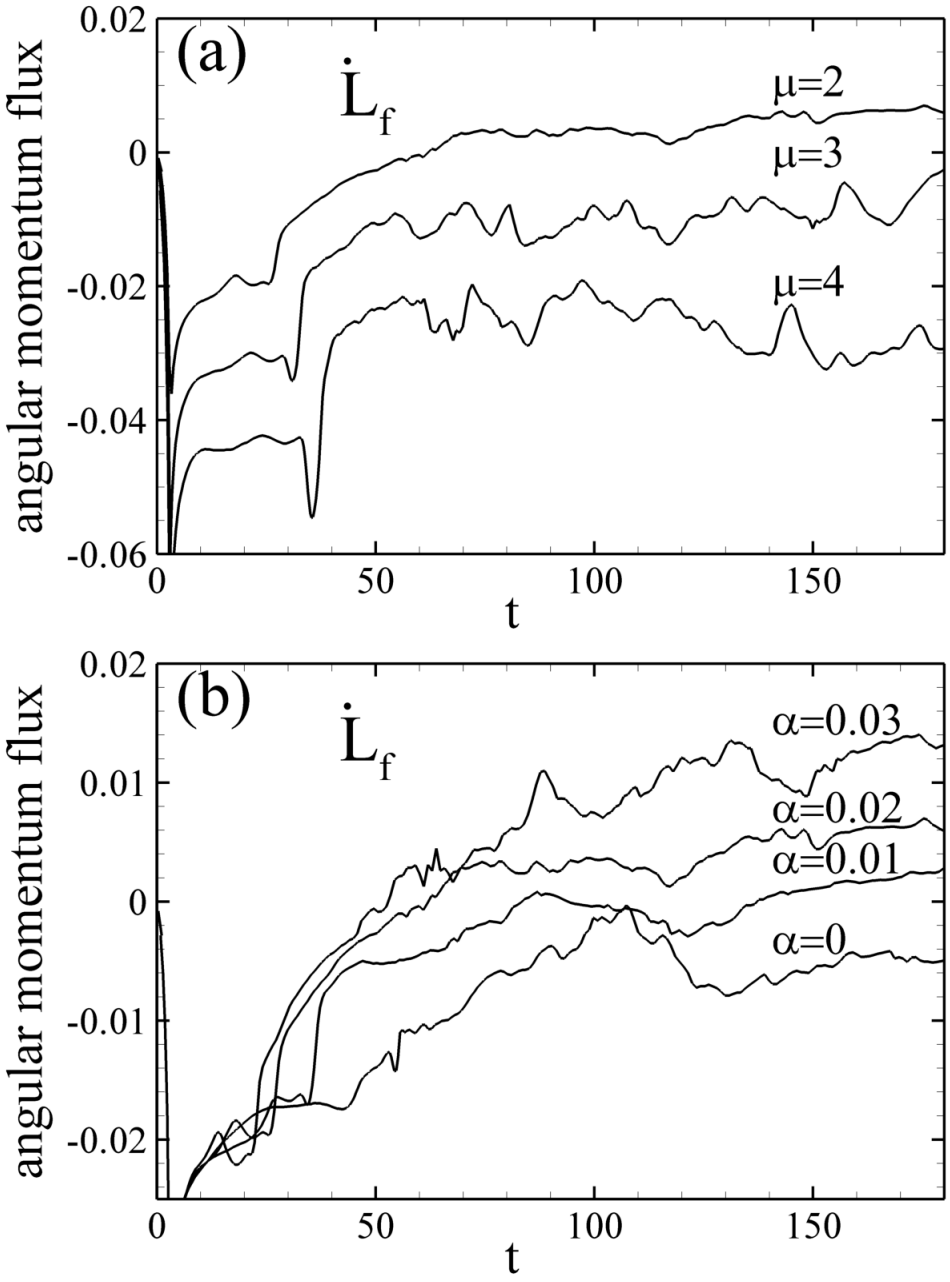

Figure 3.6: (a) The evolution of the angular momentum flux to the star carried by the magnetic field $\dot{L}_f$ for different magnetic moments of the star μ with other parameters fixed. (b) The evolution of the angular momentum flux carried by magnetic field $\dot{L}_f$ for different values of of the disk viscosity α with other parameters fixed.

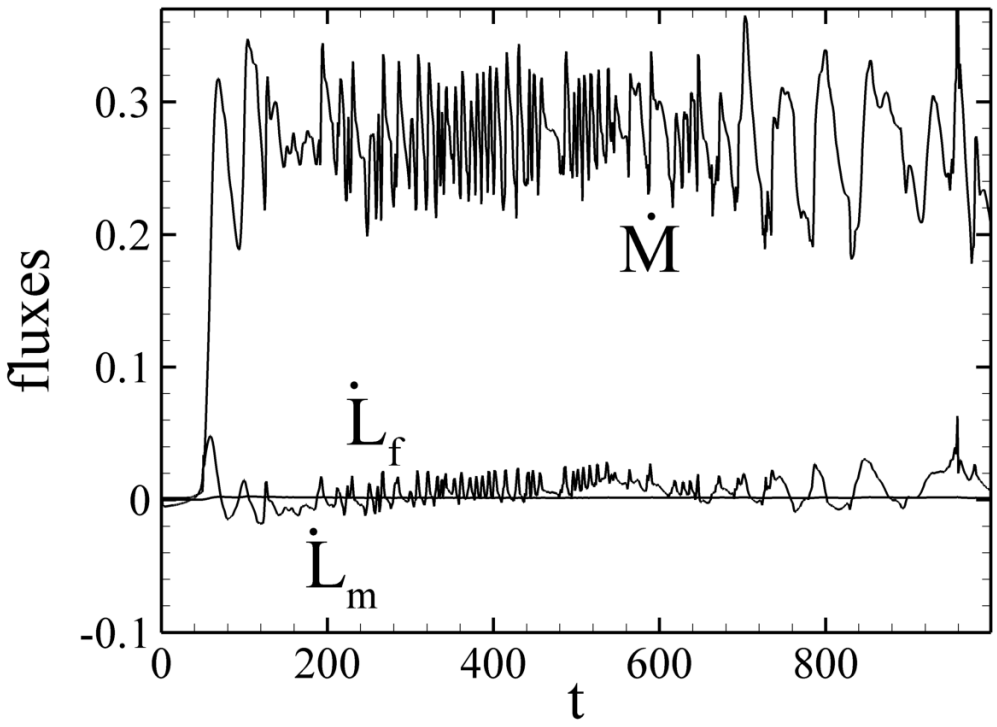

Figure 3.7: The evolution of the matter flux $\dot{M}$ and the angular momentum fluxes carried by matter $\dot{L}_m$ and magnetic field $\dot{L}_f$ in the rotational equilibrium state for the type II initial conditions.

simulation runs). In addition, we were able to use a grid $N_R \times N_\theta = 91 \times 31$ which speeded up the simulations and allowed longer runs, up to 1000 P_0.

For this case, we also performed a set of simulations for different corotation radii and found the state which gives torqueless accretion, $\dot{L} \approx 0$. We found that this state corresponds to a corotation radius $r_{co} \approx 4.6$. Figure 3.7 shows the evolution of the fluxes in this case. The angular momentum flux associated with the matter is very small as in our main case. The flux due to the magnetic field, $\dot{L}_f$, varies more strongly than in the main case. This is because the coronal density is lower so that variations of the magnetic field in the corona are larger.

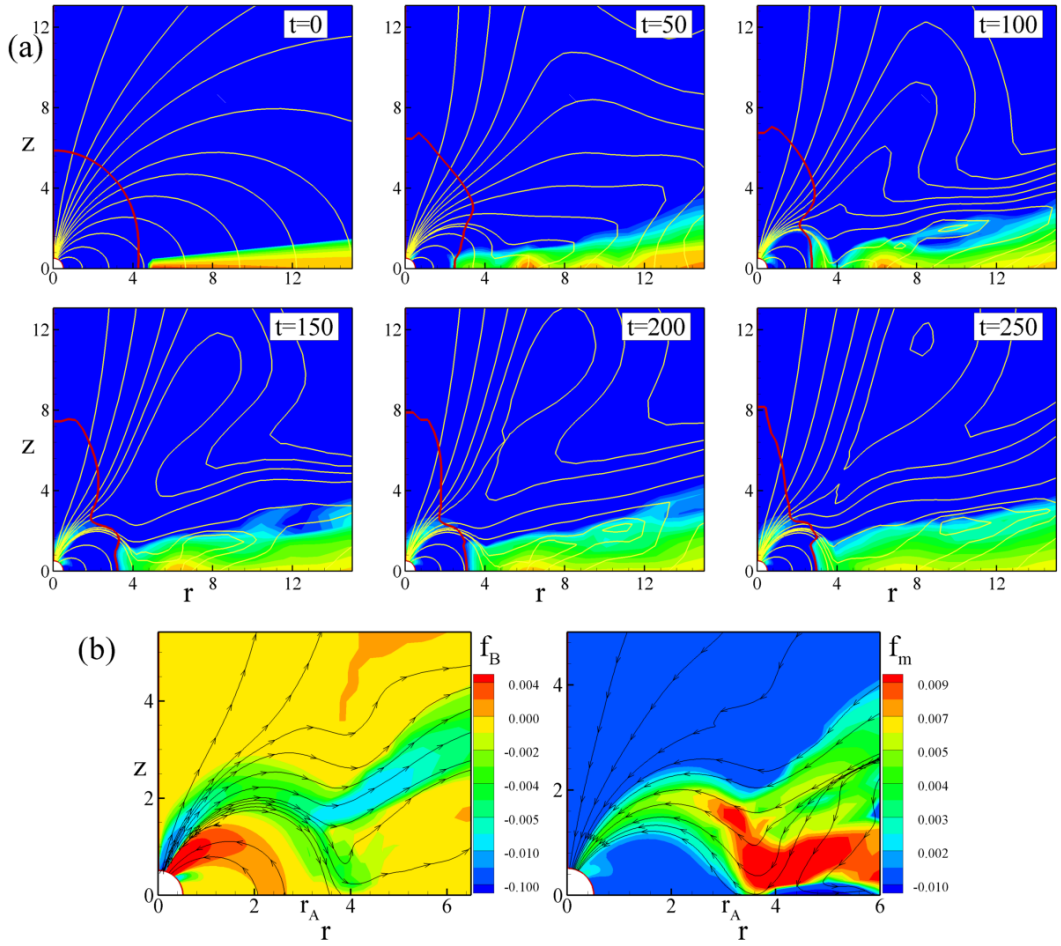

Figure 3.8: (a). Evolution of the density (color background), and the magnetic field lines (yellow lines) in rotational equilibrium state of type II initial conditions for $t = 0 - 250$ rotations. The density changes from $\rho = 2$ in the disk to $\rho = 0.001$ in the corona. The bold red line corresponds to $\beta = 1$. (b). Fluxes of angular momentum carried by magnetic field $\mathbf{f}_B$ (left panel) and by matter $\mathbf{f}_m$ (right panel) at $t = 250$. Color background shows value of the fluxes, the streamlines with arrows - the direction of the angular momentum flow.

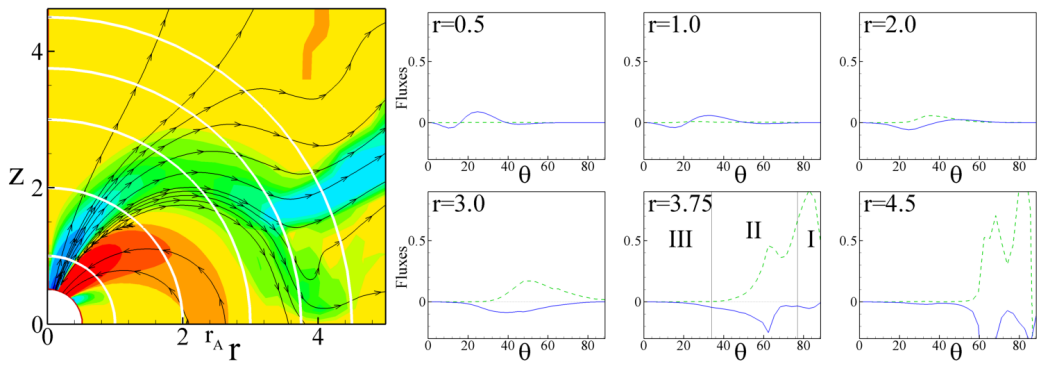

Figure 3.9: Angular distribution of fluxes for initial conditions of type II. The left-hand panel shows radii along which the angular momenta are calculated. The right-hand panel shows angular momentum fluxes carried by magnetic field $F_B(r,\theta)$ (solid lines) and matter $F_m(r,\theta)$ (dashed lines). The numbers show the regions where the angular momentum flux carried by the field is carried mostly by the closed (I), radial (II), or open (III) field lines.

In addition, the accretion rate $\dot{M}$ is several times larger than that for our main case, because the disk is different compared to the main case.

We analyzed the rotational equilibrium state in detail. Figure 3.8a shows the evolution of the disk and magnetic field in the inner part of the simulation region. We observed that the accretion disk stopped at much larger distances, $r_A \approx 3.1$, compared to our main case ($r_A \sim 1.2 - 1.3$) because of much stronger magnetic field. This radius again coincides with the $\beta = 1$ line (see the bold red line on figure 8a). We also estimated the radius r_0 derived from comparison of magnetic and matter torques. Again, we obtained similar but a somewhat larger radius, $r_0 \approx 3.2$. We observed that in type II case, the ratio $r_{co}/r_A \sim 1.4 - 1.5$. This number is slightly larger than that in the main case ($r_{co}/r_A \sim 1.3 - 1.4$) which may be connected with contribution of the inflated field lines to the negative torque.

Figure 3.8b shows the angular momentum fluxes carried by the field $F_B(r,\theta)$ and by the matter $F_m(r,\theta)$. One can see that the disk matter brings positive spin-up torque (right panel), while magnetic field carries both negative and positive torques (left panel). In this case a significant part of the spin-down flux is carried by the inflated and radially stretched field lines. This is different from the type I initial conditions case.

Figure 3.9 shows angular distribution of fluxes $F_B(r,\theta)$ and $F_m(r,\theta)$ along the spheres of different radii r from $r = 0.5$ to $r = 4.5$. One can see, that at large distances, $r = 4.5$, there is a large positive angular momentum flux carried by the matter of the disk, and there is a large negative angular momentum flux carried by the radially stretched field lines located above the disk and in the disk. Field lines above the disk are inflated field lines which connect to the disk at large radii $r > 20$. They carry both, positive matter flux, and negative spin-down flux. In this region the density is smaller than in the disk, however, the field lines are strongly wound and azimuthal velocity is large, this is why both fluxes associated with matter and the field are large in this region. The plot at $r = 3.75$ shows relative input from different sets of field lines. It shows that in the region of the closed field lines (region I) matter carries positive torque while field lines carry only small negative torque. Most of both torque is carried by the radially stretched field lines (region II), while the role of vertically inflated field lines of "magnetic tower" (region III) is very small. At even smaller radii, $r = 3, 2, 1$ and 0.5, both torques become smaller, like in type I case.

3.5 Equilibrium State in Applications to Different Stars

The rotational equilibrium state is expected to be the most probable state for different disk accreting magnetized stars. These include Classical T Tauri Stars, cataclysimic variables, and X-ray pulsars. For example, the slowly rotating CTTSs have spin rates as low as $\sim$ 10% of breakup speed (Bouvier et al. 1993). The fact that CTTSs rotate slowly strongly suggests that they are in rotational equilibrium state.

Below we estimate periods of rotation for different weakly magnetized stars. Our simulations were performed for cases $r_A/R_* = 4-6$ and can be applied to systems with different scales in which this ratio is satisfied. Observations show that in CTTS this ratio is in the range $r_A/R_* = 4-8$ (Bouvier et. al., 1993, Edwards et al., 1993), or, $r_A/R_* = 3-10$ (Kenyon, Yi & Hartmann, 1996). Similar or smaller magnetospheres are expected in accreting millisecond pulsars (van der Klis 2000) and dwarf novae cataclysmic variables (Warner 2004).

For our example we take $r_A/R_* = 4$, take obtained from simulation ratio $r_{co} = 1.4r_A$ and derive the angular velocity for rotational equilibrium, Ω_{eq}:

$$\frac{\Omega_{eq}}{\Omega_{*K}} = \left(\frac{R_*}{r_{co}}\right)^{3/2} \approx 0.09 \,, \tag{3.13}$$

which is about $\sim$ 10% of breakup speed of the star. Here, Ω_{*K} is the Keplerian angular speed at R_*. The value of Ω_{eq}/Ω_{*K} we find is close to the one observed in CTTSs.

3.5.1 Classical T Tauri Stars (CTTSs)

The angular velocity of the star can be written as $\Omega_* = (GM/r_{co}^3)^{1/2}$. Combining this with the rotational equilibrium condition $r_{co}/r_A \sim 1.3 - 1.5$ (an average 1.4 was taken here) and using Eqn. 1 for the Alfvén radius, we can get the critical value of angular velocity Ω_{eq} or rotation period $P_{eq} = 2\pi/\Omega_{eq}$. For the CTTS we obtain the equilibrium rotation period,

$$P_{eq} \approx 4.6 \text{ days} \Big(\frac{0.8M_\odot}{M}\Big)^{5/7} \Big(\frac{10^{-7}M_\odot/\text{yr}}{\dot{M}}\Big)^{3/7} \times \Big(\frac{B}{10^3\text{G}}\Big)^{6/7} \Big(\frac{R_*}{2R_\odot}\Big)^{18/7}, \tag{3.14}$$

where B is the surface magnetic field of the star. Our result is in the range of an observational bimodal distribution of rotation at period with peaks near 3 and 8 days (Attridge & Herbst 1992). Edwards et al. (1993) proposed that the distribution near 8 days may be caused by the disk locking. We should note that both peaks may be connected with the disk locking, but at different parameters, say, $\dot{M}$ and B.

3.5.2 Cataclysmic Variables

We next consider dwarf novae which belong to a subtype of the cataclysmic variables where the magnetic field is expected to be small but still possibly dynamically important for the accretion. The accretion disks are stopped at small radii by the white dwarf magnetosphere. The accreting material then leaves the disk and follows the magnetic field lines down to the star's surface in the vicinity of the magnetic poles. Taking typical values for the white dwarf and ac-

cretion disk, we obtain the period of these stars in rotational equilibrium state,

$$P_{eq} \approx 57 \text{ s} \Big(\frac{M_\odot}{M}\Big)^{5/7} \Big(\frac{10^{-8} M_\odot/\text{yr}}{\dot{M}}\Big)^{3/7} \times \Big(\frac{B}{10^5 \text{G}}\Big)^{6/7} \Big(\frac{R}{7.0 \times 10^8 \text{cm}}\Big)^{18/7}. \quad (3.15)$$

The observed periods of Dwarf Novae Oscillations (DNOs) are in the range of 7 – 70 s (Warner, 2004).

3.5.3 Millisecond Pulsars

Our simulations are also applicable to millisecond X-ray pulsars, which are the accreting low-magnetic-field neutron stars (van der Klis, 2000). The period of such a star in the rotational equilibrium is

$$P_{eq} \approx 1.8 \text{ ms} \Big(\frac{1.4 M_\odot}{M}\Big)^{5/7} \Big(\frac{10^{-9} M_\odot/\text{yr}}{\dot{M}}\Big)^{3/7} \times \Big(\frac{B}{10^8 \text{G}}\Big)^{6/7} \Big(\frac{R}{10^6 \text{cm}}\Big)^{18/7}. \quad (3.16)$$

For all accretion-powered millisecond X-ray pulsars we have known, the spin frequencies range from 185Hz to 435Hz (Wijnands, R. 2004), or, the spin rate is in range of 2.3-5.2 ms. These values may be obtained from equation 3.16 at smaller $\dot{M}$ or larger B.

3.6 Discussion

We investigated the conditions for the rotational equilibrium or"torqueless" accretion state using axisymmetric MHD simulations. In such a state the total angular momentum flux to the star is approximately zero. We found the equilibrium states by gradually changing the angular velocity of the star with the

other parameters fixed. We considered two main cases: One with relatively low magnetic field and dense corona and second with much stronger field and lower density corona. We observed that in both cases the rotation of the star is approximately locked to the rotation of the inner radius of the disk such that a star rotates somewhat slower than the inner radius of the disk. In the first case the ratio between corotation radius of the star and the Alfvén radius r_A (where the disk is disrupted) is $r_{co}/r_A \sim 1.3 - 1.4$. In the second case, where stronger inflation of the magnetic field was observed, this ratio is only slightly larger, $r_{co}/r_A \sim 1.4 - 1.5$. We observed that in the first case, the angular momentum transport is associated with the closed field lines at the inner radii of the disk. Open field lines spin down the star, but the role of this spin-down is small. In the second case outflow of angular momentum along the inflated field lines is more significant than in the first case, however this did not change the result, which probably means that the angular momentum transport associated with the inner regions of the disk and the region of the funnel flow is more significant. Thus, in both cases the magnetic interaction effectively locks the rotation rate of the star to a value which depends mainly on the mass accretion rate and the star's magnetic moment. We should note that most of coronal region is still matter dominated. This is connected with the fact that the magnetic energy-density of the dipole decreases with distance as $\sim R^{-6}$ so that it is difficult to set up a magnetically dominated corona. Goodson et al. (1997, 1999) were able to model such a corona by arranging fast fall-off of coronal density with the distance. However, their initial conditions are sufficiently far from equilibrium that the torqueless accretion was not established. Future simulations with even lower coronal densities will help to understand whether a star is always locked to the rotation rate of the inner radius of the disk. Our simulations for two very

different initial conditions have shown very similar results for the rotational equilibrium which may be a sign that the disk-locking may be a similar for all slowly rotating stars.

We applied our simulation results to Classical T Tauri stars, where disk locking may explain their slow rotation. Also, we estimated the probable periods of rotation of other accretion powered systems, such as dwarf novae and X-ray millisecond pulsars.

CHAPTER 4

ACCRETION TO STARS WITH NON-DIPOLE MAGNETIC FIELDS*

Disc accretion to a rotating star with a non-dipole magnetic field is investigated for the first time in full three-dimensional (3D) magnetohydrodynamic (MHD) simulations. We investigated the cases of (1) pure dipole, (2) pure quadrupole, and (3) dipole plus quadrupole fields. The quadrupole magnetic moment $\mathbf{D}$ is taken to be parallel to the dipole magnetic moment $\boldsymbol{\mu}$, and both are inclined relative to the spin axis of the star $\boldsymbol{\Omega}$ at an angle Θ. Simulations have shown that in each case the structure of the funnel streams and associated hot spots on the surface of the star have specific features connected with the magnetic field configuration. In the pure dipole case matter accretes in two funnel streams which form two arch-like spots near the magnetic poles. In the case of a pure quadrupole field, most of the matter flows through the quadrupole "belt" forming a ring-shaped hot region on the magnetic equator. In the case of a dipole plus quadrupole field, magnetic flux in the northern magnetic hemisphere is larger than that in the southern, and the quadrupole belt and the ring are displaced to the south. The stronger the quadrupole, the closer the ring is to the magnetic equator. At sufficiently large Θ, matter also flows to the south pole, forming a hot spot near the pole. The light curves have a variety of different features which makes it difficult to derive the magnetic field configuration from the light curves. There are specific features which are different in cases of dipole and quadrupole dominated magnetic field: (1) Angular momentum flow between the star and disk is more efficient in the case of the dipole field; (2) Hot spots are hotter and brighter in case of the dipole field because the matter

*This chapter is based on the published paper by Long et al. 2007, the Monthly Notices of the Royal Astronomical Society, 374, 436. It is rewritten here with minor changes.

accelerates over a longer distance compared with the flow in a quadrupole case.

4.1 Introduction

Many accreting stars have a strong magnetic field which disrupts the accretion disk and channels accreting matter to the star's surface. For such stars many spectral and photometric properties are determined by the magnetic field. Examples include young solar-type stars (Classical T Tauri stars, hereafter CTTS, e.g., Hartmann 1994), neutron stars in binary systems (X-ray pulsars and millisecond pulsars, e.g. Ghosh & Lamb 1978; Chakrabarty et al. 2003), white dwarfs in the binary systems (cataclysmic variables, e.g. Wickramasinghe et al. 1991; Warner 1995, 2000), and also brown dwarfs (e.g., Scholz & Ray 2006). The properties of such accretion will depend on the structure of the magnetic field of the star.

In early models it was assumed that the star's intrinsic magnetic field was a pure *dipole* (Ghosh & Lamb 1979a,b; Camenzind 1990; Königl 1991). Recently, 2D and full 3D MHD numerical simulations of magnetospheric accretion were performed which confirmed many predicted features and revealed many new details of accretion to a star with a dipole field (Romanova et al. 2002, 2003, 2004; Long et al. 2005; Kulkarni & Romanova 2005). Different aspects of the disc-magnetosphere interaction were also investigated numerically (Hayashi et al. 1996; Hirose et al. 1997; Miller, & Stone 1997; Goodson, Winglee & Böhm 1997, 1999; von Rekowski & Brandenburg 2004, 2006) and theoretically (e.g., Lovelace, Romanova & Bisnovatyi-Kogan 1995; Uzdensky, Königl & Litwin 2002; Matt & Pudritz 2004, 2005).

However, the actual configuration of the magnetic field of strongly magnetized stars may depart from the dipole one. For example, Safier (1998) presented a number of arguments pointing to a non-dipolar magnetic fields in some CTTSs. The Zeeman measurements of the magnetic field of a number of CTTSs based on the photospheric lines show that the magnetic field at the surface of CTTSs is strong (1-3 kGs) but not ordered, which means that close to the star the magnetic field is non-dipole (e.g., Johns-Krull et al. 1999; Johns-Krull, Valenti, & Koresko 1999; Johns-Krull & Gafford 2002; Smirnov et al. 2003).

The measurements of the magnetic fields of rapidly rotating low-mass stars with the Zeeman-Doppler imaging technique have shown that in a number of stars the magnetic field has a complicated multipolar topology close to the star (Donati & Cameron 1997; Donati et al. 1999; Jardine et al. 2002). If the multipolar component dominates in the disc-accreting binary systems, then the matter flow to the star and the hot spots will be different from those in the case of a pure dipole field (e.g., Jardine et al. 2006).

The dipole magnetic field may of course dominate in some stars, and it will dominate at larger distances from stars with complex surface magnetic fields. There are observational signs that the dipole component possibly disrupts the disc. In many cases there is evidence that the dipole field dominates at all distances, giving periodic light curves in X-ray binaries, intermediate polars, and some CTTSs. In addition, direct measurements of the magnetic field using polarization of some spectral lines shows evidence of the pure dipole field in a number of the CTTSs (Valenti & Johns-Krull 2004; Symington et al. 2005). An remarkable result was recently obtained by Gregory et al. (2006) who recovered the magnetic field of the convective low- mass star v374Peg and obtained a pure

dipole configuration. Thus the magnetic field configuration is likely to be different in stars with varying levels of importance of the dipole component. Bouvier et al. (2006) argued that there are many signs of magnetospheric accretion in CTTSs and that the field is probably dipolar at larger distances from the star, but may have a strong multipolar component close to the star.

Recently, the first theoretical and numerical research was done on accretion to a star with a non-dipole magnetic field. Jardine et al. (2006) investigated the possible paths of the accreting matter in the case of a multipolar field derived from observations. Donati et al. (2006) developed a simplified stationary model for such accretion. von Rekowski and Brandenburg (2006) performed axisymmetric simulations of the disc-magnetosphere interaction in case when magnetic field is generated by the dynamo processes both, in the star and in the disc. They obtained a time-variable magnetic field of the star with a complicated multipolar configuration which shows that the dynamo may be responsible for a complex magnetic field structure.

In this paper we show the first results of full 3D MHD simulations of accretion to a star with a non-dipole magnetic field frozen to the stellar surface. As a first step, we take a combination of the dipole and quadrupole fields with aligned axes and investigate properties of the funnel streams and hot spots at the surface of the star. More complicated structures of the field will be considered in future simulations. Analytical analysis of accretion to a non-rotating star with a pure quadrupole magnetic field was done by Lipunov (1978). Combination of dipole and multipole fields was discussed by Lovelace et al. (2005). However, no numerical simulations of such accretion have been performed so far.

In this chapter, first, we describe the magnetic field configurations used in the simulations. We present simulation results and study the dependence on different parameters in following sections, and give a summary at the end.

4.2 Magnetic Fields of the Star

In the absence of plasma outside the star, the space is current free, we would have

$$\nabla \times \mathbf{B} = 0, \tag{4.1}$$

so that the intrinsic magnetic field of the star can be written as

$$\mathbf{B} = -\nabla\varphi, \tag{4.2}$$

where the scalar potential of the magnetic field is

$$\varphi(\mathbf{r}) = \Sigma m_a/|\mathbf{r} - \mathbf{r}_a|, \tag{4.3}$$

and m_a is an analogy of the magnetic "charge", $\mathbf{r}$ and $\mathbf{r}_a$ are the positions of the observer and the magnetic "charges" respectively. The scalar potential can be represented as a multipole expansion in powers of $1/r$ (e.g. Landau & Lifshitz 1983),

$$\varphi = \Sigma\frac{m_a}{|\mathbf{r} - \mathbf{r}_a|} = \varphi^{(0)} + \varphi^{(1)} + \varphi^{(2)} + \ldots \ . \tag{4.4}$$

The first term $\varphi^{(0)} = 0$ because there are no monopoles. The second term is the dipole component, $\varphi^{(1)} = \mu\cos\theta/r^2$, where μ is the dipole moment. The third term is the quadrupole component,

$$\varphi^{(2)} = \frac{D_{\alpha\beta}}{6}\frac{\partial^2}{\partial x_\alpha \partial x_\beta}\left(\frac{1}{r}\right),$$

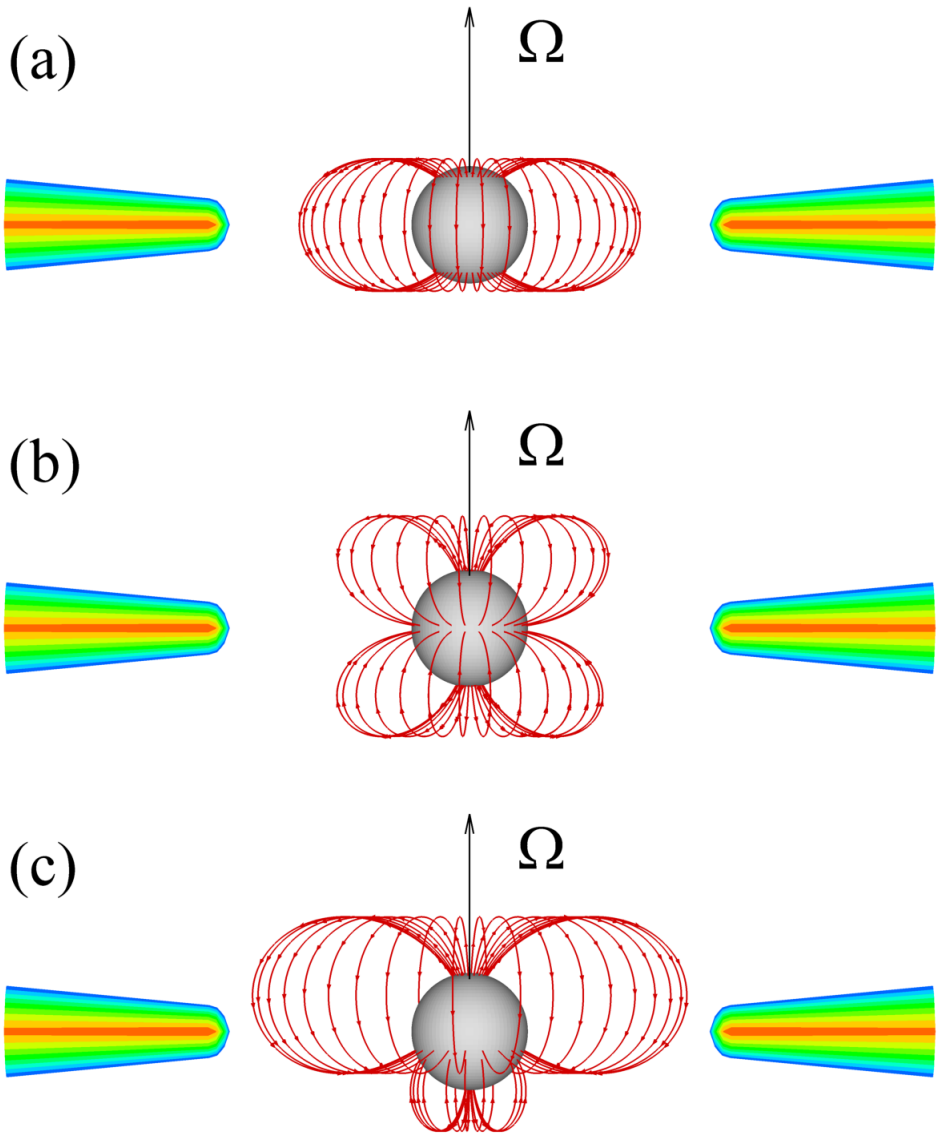

Figure 4.1: Initial configurations of the magnetic fields used in simulations. (a) Pure dipole field with $\mu \neq 0$, $D = 0$; (b) Pure quadrupole field $D \neq 0$; (c) Dipole plus quadrupole field, $\mu \neq 0$, $D \neq 0$. The inner region of the accretion disk is also seen in the figures.

where x_α, x_α are the components of $\mathbf{r}$, $D_{\alpha\beta}$ is the magnetic quadrupole moment tensor, and the sum over repeated indices is implied. Because

$$D_{\alpha\alpha} = 0, \tag{4.5}$$

we have,

$$\varphi^{(2)} = D_{\alpha\beta} n_\alpha n_\beta / 2r^3, \tag{4.6}$$

where $n_\alpha = x_\alpha / r$, $n_\beta = x_\beta / r$.

Considering the *axisymmetric* case where $D_{11} = D_{22} = -D_{33}/2$, we call $D = D_{33}$ the quadrupole moment and refer to the axis of symmetry as the "direction" of the quadrupole moment. In spherical coordinates (r, θ, ϕ), we have,

$$\varphi^{(2)} = \frac{D}{4r^3}(3\cos^2\theta - 1) = \frac{D}{2r^3} P_2(\cos\theta) \ , \tag{4.7}$$

where P_2 is a Legendre polynomial. Then we can get the quadrupole magnetic field $\mathbf{B}$ and the flux function Ψ:

$$B_r \equiv -\frac{\partial\varphi}{\partial r} = \frac{3D}{4r^4}(3\cos^2\theta - 1) \ , \tag{4.8}$$

$$B_\theta \equiv -\frac{1}{r}\frac{\partial\varphi}{\partial\theta} = \frac{3D}{2r^4}\sin\theta\cos\theta \ , \tag{4.9}$$

$$\Psi = \frac{3D}{4r^2}\sin^2\theta\cos\theta \ . \tag{4.10}$$

In our simulations we use a combination of dipole and quadrupole magnetic fields:

$$B_r = \frac{2\mu\cos\theta}{r^3} + \frac{3D}{4r^4}(3\cos^2\theta - 1) \ , \tag{4.11}$$

$$B_\theta = \frac{\mu\sin\theta}{r^3} + \frac{3D}{2r^4}\sin\theta\cos\theta \ , \tag{4.12}$$

$$\Psi = \frac{\mu\sin^2\theta}{r} + \frac{3D}{4r^2}\sin^2\theta\cos\theta \ . \tag{4.13}$$

The star has fixed dipole and/or quadrupole magnetic fields with moments μ and D respectively. For simplicity, they are in the same direction and are inclined with respect to the rotational axis Ω at an angle Θ. We investigated accretion at angles $\Theta = 0^\circ$, $\Theta = 30^\circ$, and $\Theta = 60^\circ$. Spin axes of the star and the disk coincide.

We vary the value of the quadrupole moment from a pure dipole case, $D = 0$, up to a pure quadrupole case, $\mu = 0$. Figure 4.1 shows the main initial configurations of the magnetic field considered in the paper: (a) pure dipole configuration, $D = 0$; (b) pure quadrupole case $\mu = 0$; and (c) the case when the dipole and quadrupole fields are of the same order. One can see that when both dipole and quadrupole fields are present, the field is not symmetric relative to the equatorial plane: the magnetic flux Ψ is larger in the northern hemisphere where the dipole field is added to the quadrupole field, and smaller in the southern hemisphere where the dipole field is subtracted from the quadrupole field. Simulations have shown that this feature of the dipole plus quadrupole field leads to results different from the pure dipole case.

4.3 Results of Simulations

4.3.1 Accretion to a Star with Pure Dipole and Pure Quadrupole Magnetic Fields

First, for reference we show the results of simulations of accretion to a star with a pure dipole field with $\mu = 0.5$ inclined relative to the spin axis at an angle

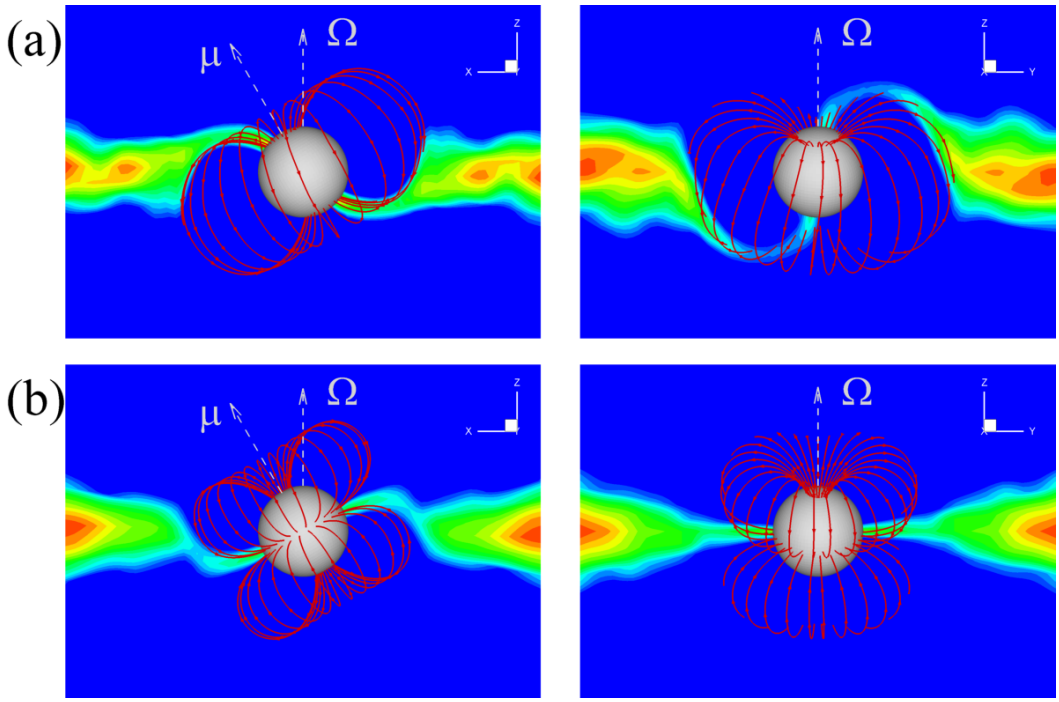

Figure 4.2: Disc accretion to a star with (a) pure dipole and (b) pure quadrupole magnetic configurations at $\Theta = 30°$ and at time $t = 5$. The left panels show projections in the $x - z$ ($\mu\Omega$) plane, and the right panels show projections in the $y - z$ plane. The background shows density contours, and the red lines show the outermost closed field lines.

$\Theta = 30°$. Figure 4.2a (left panel) shows the density distribution in the $x - z$ plane (this is also the $\boldsymbol{\mu} - \boldsymbol{\Omega}$ plane). One can see that most of the matter flows through symmetric funnel streams to the nearest magnetic pole. A smaller amount of matter flows to the opposite pole. The right panel shows the cross- section in the $y - z$ plane, where similar but weaker streams are observed. In fact at sufficiently low density levels the matter blankets the magnetosphere completely (Romanova et al. 2003) so that at these levels any cross-section will show the funnel streams.

Figure 4.2b shows the results of accretion to a pure quadrupole magnetic configuration with $\mu = 0$, and $D = 0.5$, which is inclined at an angle $\Theta = 30^{\circ}$. The left panel shows that in the $x - z$ cross-section, matter is slightly lifted above the equatorial plane and flows through the quadrupole belt to the equatorial region of the star. The right panel shows that in the $y - z$ plane, matter flows straight to the equatorial belt without being lifted.

Figure 4.3a shows the three-dimensional distribution of matter flow around a star with a pure quadrupole field, where one of density levels is shown in green color. The left projection demonstrates that the matter flows in a thin sheet approximately in the plane of the magnetic equator. The right panel shows that this flow is wide and is not axisymmetric. Thus, in the pure quadrupole case matter flows to the star in a thin, wide sheet in the region of the magnetic equator.

4.3.2 Accretion to a Star with a Dipole plus Quadrupole Magnetic Field

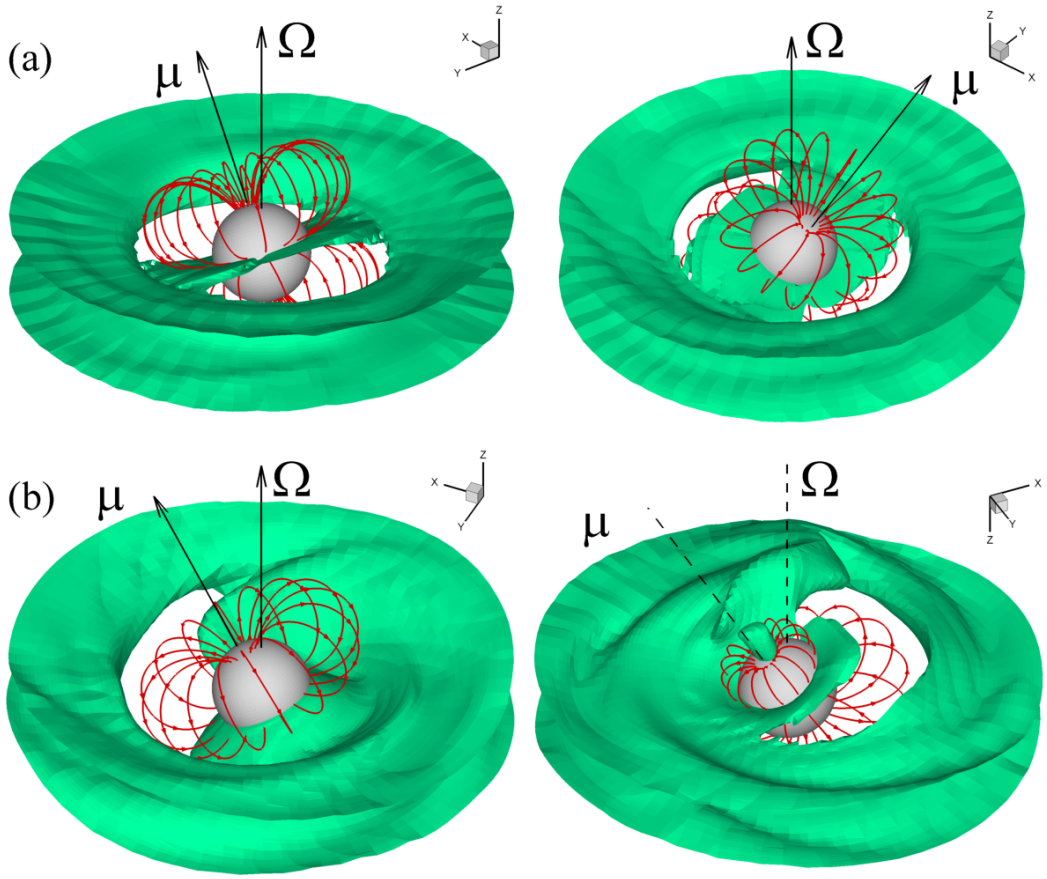

Figure 4.3: Three-dimensional picture of matter flow around the star for the pure quadrupole case (top panels -a) and for a dipole plus quadrupole case at $\mu = 0.5$, $D = 0.5$ (bottom panels -b). In both cases $\Theta = 30°$. The background shows one of the density levels, $\rho = 0.2$. Red lines are the outermost closed field lines. In (b), the dashed lines mean the south part of the rotation axis and magnetic axis.

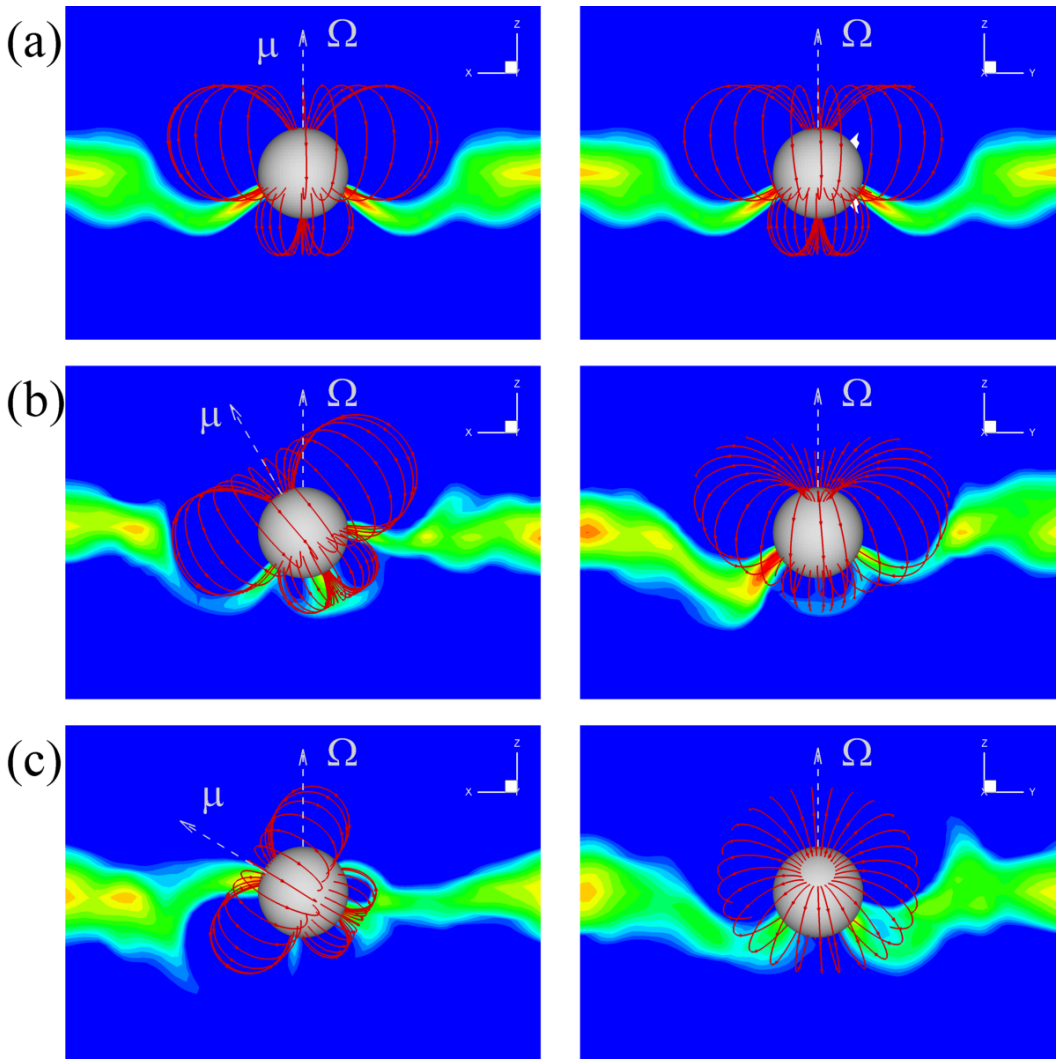

Figure 4.4: Disc accretion to a star with a dipole plus quadrupole magnetic field $\mu = 0.5$, $D = 0.5$ for different misalignment angles: (a) $\Theta = 0°$; (b) $\Theta = 30°$; (c) $\Theta = 60°$ at time $t = 5$. The left panels show projections in the $x - z$ ($\mu\Omega$) plane, and the right panels show projections in the $y - z$ plane. The background shows density contours, and the red lines show the outermost closed field lines.

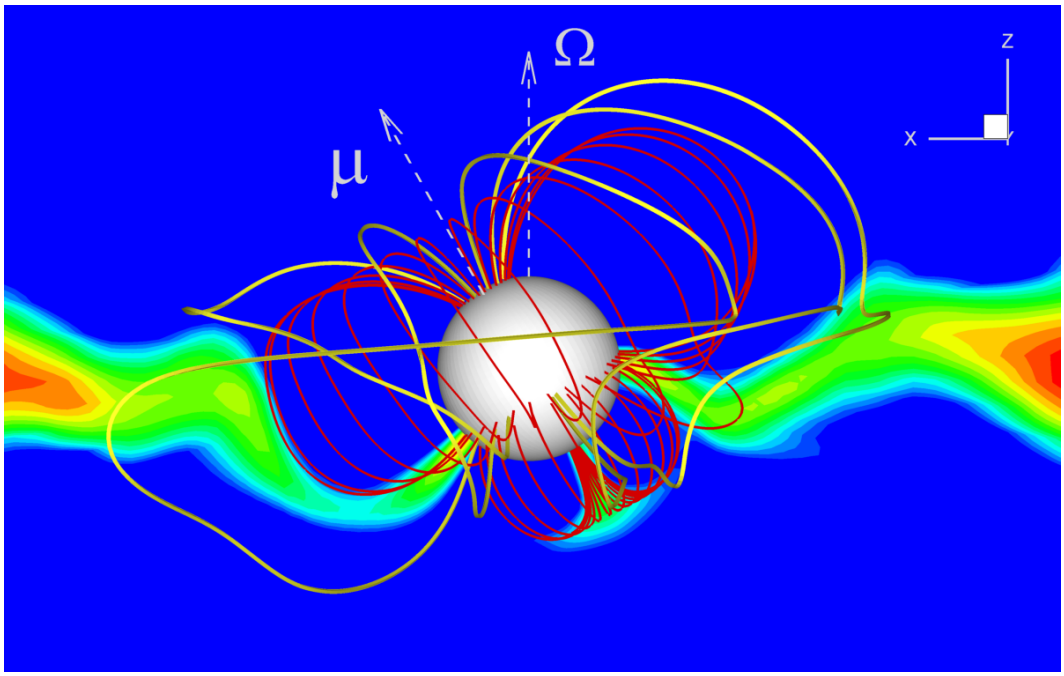

Figure 4.5: The detailed structure of disk accretion to a star with a dipole plus quadrupole field, with $\mu = 0.5$, $D = 0.5$, $\Theta = 30°$. In addition to the closed field lines (red lines), a number of sample open field lines (yellow lines) are shown.

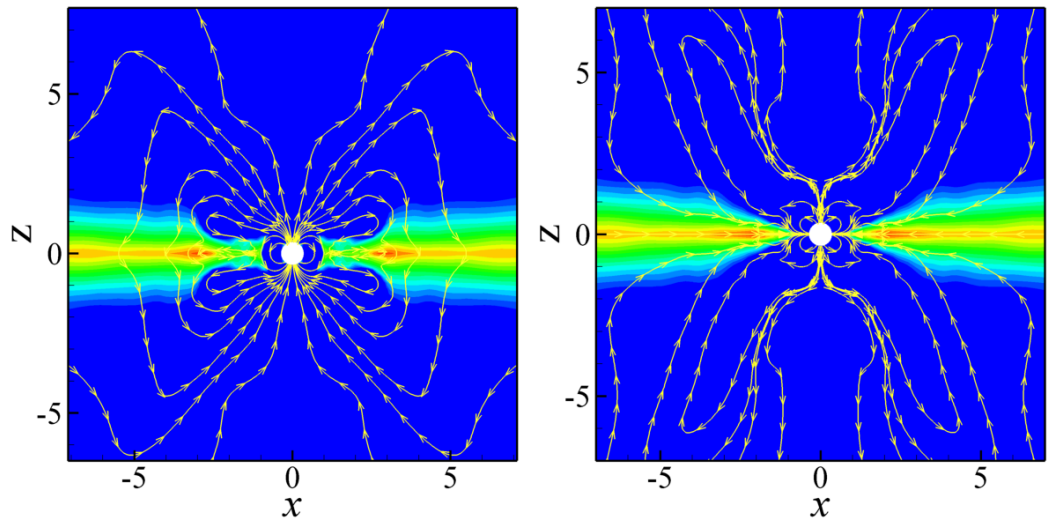

Figure 4.6: The large-scale structure of the magnetic field (yellow lines) in the cases of pure dipole at $\mu = 0.5$ (left panel) and pure quadrupole $D = 0.5$ (right panel) at $\Theta = 0$. The background shows the density distribution where density varies from $\rho = 2$ (red) to $\rho = 0.01$ (blue).

We calculated the case of the dipole plus quadrupole magnetic field at three misalignment angles, $\Theta = 0°$, $\Theta = 30°$, and $\Theta = 60°$. In all cases we took $\mu = 0.5$ and $D = 0.5$. This magnetic configuration is not symmetric relative to the equatorial plane. In the northern hemisphere the magnetic flux of the dipole is added to that of the quadrupole, so that magnetic flux is larger than the pure dipole one. In the southern hemisphere, the magnetic flux of the dipole is subtracted from that of the quadrupole, so that the flux is smaller than the dipole flux.

Figure 4.4a shows the $x-z$ (left panels) and $y-z$ (right panels) cross-sections of accretion to a star with $\Theta = 0°$. One can see that the matter flows axisymmetrically to the quadrupole equatorial belt, which is now located in the southern hemisphere.

Figure 4.4b shows the case $\Theta = 30°$. Here, part of the matter flows to the

south polar region. Figure 4.3b shows the 3D view of such a flow in the northern hemisphere. One can see that matter flows through the quadrupole belt, but the flow is not symmetric relative to the $z-$axis. The right panel shows the flow as seen from the southern hemisphere, where part of the matter flows to the south pole region.

Figure 4.4c shows that at $\Theta = 60^\circ$, the flow is even more complicated: some matter flows to the north pole, some matter flows to the south pole, and some matter flows through the belt.

So, one can expect that in the case of $\Theta \approx 0^\circ$, accretion to a quadrupole or a combined dipole-quadrupole field will go through a quadrupole belt and will form a ring-like spot at the surface of the star. However, at large misalignment angles Θ the structure of the accreting streams is more complicated.

4.3.3 Disc-Magnetosphere Interaction and Magnetospheric Radius

Here we chose one of typical cases with mixed dipole and quadrupole fields, $\mu = 0.5$, $D = 0.5$, and $\Theta = 30^\circ$, and consider it in greater detail. First, we estimate the modified plasma β parameter,

$$\beta = \frac{p + \rho v^2}{B^2/8\pi} \approx \frac{\rho v_\phi^2}{B^2/8\pi},$$

where we took into account that the ram pressure of matter in the disk is much larger than the thermal pressure. The surface $\beta = 1$ separates the regions of magnetically dominated and matter dominated plasma. This surface crosses the equatorial plane at the magnetospheric radius r_m, which is $r_m \approx 1.14$. One

can see from Figure 4.5 that this is the radius where the disk is disrupted and matter goes to the funnel streams. Both dipole and quadrupole components contribute to the magnetosphere and to the disruption of the disc.

For $r < r_m$, the magnetic energy-density dominates, and the field lines are closed. However, at larger radii the field lines are dragged by the disk and also inflate and open in the corona. Figure 4.5 shows the outermost closed field lines (red lines) and also some open field lines (yellow lines) in the corona.

Opening and inflation of the field lines is somewhat different between the dipole-dominated and quadrupole-dominated fields. Figure 4.6 shows the large-scale structure of the magnetic field in the dipole case at $\mu = 0.5$, $D = 0$ (left panel) and in the quadrupole case at $D = 0.5$, $\mu = 0$ (right panel). One can see that in both cases there is a closed magnetosphere close to the star and a set of inflated field lines at larger distance. We should note that in our 3D simulations, inflation is somewhat suppressed by relatively dense corona and in reality it may be more efficient. From the other side, these plots are shown for $t = 8$ and at longer time inflation of the external field lines may progress further. In spite of that, the typical pattern of the inflated field lines is different for the dipole and for the quadrupole. In both cases the open field lines participate in the spin-down of the star (see Section 5).

4.4 Hot Spots and Light Curves

The inflowing matter of the funnel streams falls onto the star and forms hot spots on the stellar surface. The shape of the hot spots reflects the shape of the funnel streams. Earlier 3D simulations of accretion to a star with a misaligned

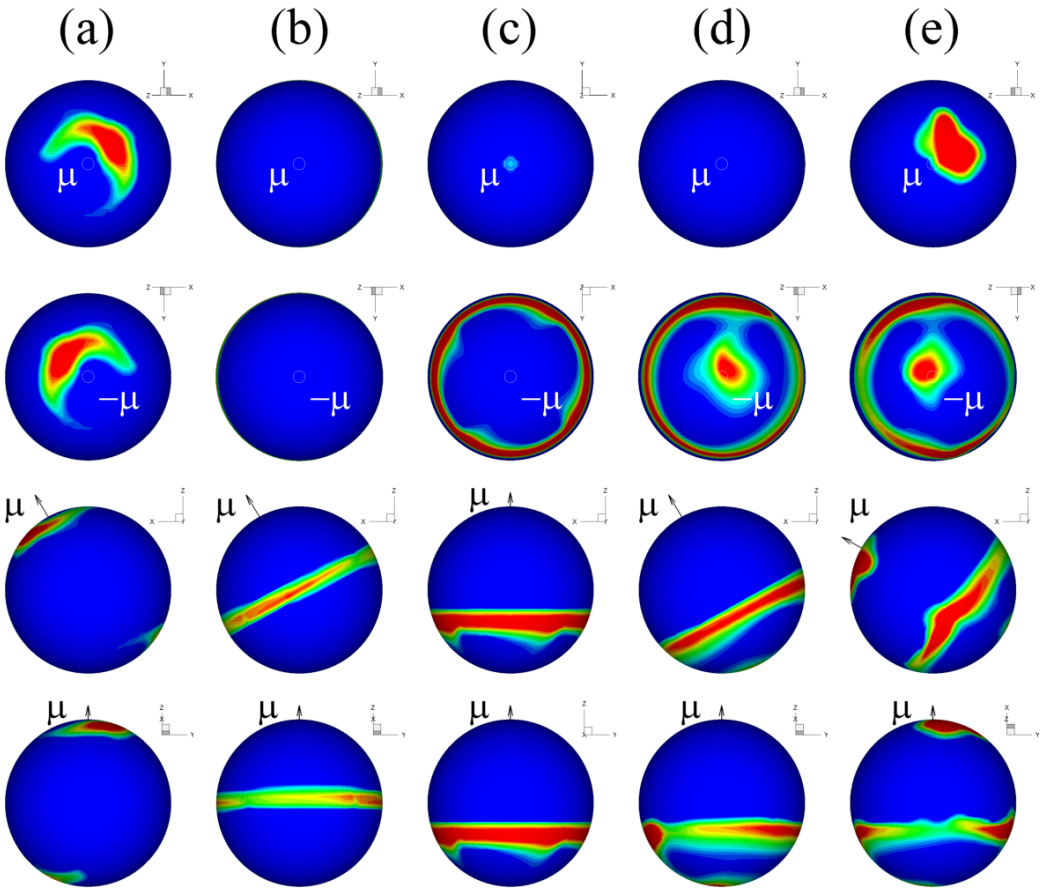

Figure 4.7: The hot spots at t=5 shown at different projections: from the top to the bottom, each column shows views from the north and south magnetic poles, the $x-z$ projection and the $\mu-y$ projection respectively. The background shows density contours. Red color corresponds to the maximum density ($\rho = 2.5$) and dark blue corresponds to the minimum density $\rho = 0.01$. (a) pure dipole case, $\mu = 0.5$, $D = 0$ at $\Theta = 30°$; (b) pure quadrupole case, $\mu = 0$, $D = 0.5$ at $\Theta = 0°$. Columns (c), (d) and (e) show spots for the $\mu = D = 0.5$ case for $\Theta = 0°$, $\Theta = 30°$ and $\Theta = 60°$ respectively.

dipole magnetic field have shown that hot spots are always similar in the northern and southern hemispheres (Romanova et al. 2004). Our present simulations with a dipole plus quadrupole magnetic fields have shown that hot spots are always *different* in the northern and southern hemispheres.

Figure 4.7 shows the hot spots for different magnetic configurations at $t = 5$. From the top to the bottom, each column shows view from the north and south magnetic poles, the $x - z$ projection and the $\mu - y$ projection respectively.

Column (a) represents the results for a pure dipole magnetic field with $\mu = 0.5$ and misalignment angle $\Theta = 30^\circ$. One can see that there are two hot spots near the magnetic poles which are similar to each other. Column (b) shows the results for a pure quadrupole configuration at $\Theta = 30^\circ$. The inflowing matter forms a ring near the magnetic equatorial plane in the region of the quadrupole belt. The ring has two density enhancements from two opposite sides because the flow is not axisymmetric (See also Figure 4.3a). Columns (c), (d) and (e) show the results for a dipole plus quadrupole field, $\mu = 0.5$, $D = 0.5$, for misalignment angles $\Theta = 0$, $\Theta = 30^\circ$ and $\Theta = 60^\circ$ respectively. In the case of $\Theta = 0^\circ$, (column c), the hot spot has the shape of the ring located below the equatorial plane. The ring is below the equator because the magnetic field in the northern hemisphere is much stronger than that in the southern hemisphere and the quadrupole belt is displaced to the south. The ring is symmetric relative to $\mathbf{\Omega}$ axis because $\Theta = 0^\circ$. There are no hot spots near the poles (see also Figure 4.4a). Column (d) shows the case when $\Theta = 30^\circ$. One can see that the magnetic flux in northern hemisphere is still strong enough to stop the flow to the north magnetic pole, so there is no hot spot. However, some matter flows to the south magnetic pole along closed field lines of the southern part of the magnetosphere. Column

(e) shows the results for $\Theta = 60^\circ$. Now the magnetic axis is tilted more towards the disc, which leads to matter flow to both the north and south magnetic poles. We can still see the belt in the southern hemisphere.

Consider now the light curves from hot spots on the star for different magnetic configurations. We assume that the kinetic energy of the inflowing matter is converted into black-body radiation and is radiated isotropically (e.g. Romanova et al. 2004). The variation in the light curve is associated with the position and shape of the hot spots. This means that the evolution of the hot spots can affect the light curves. After several rotations of the star, the shape and position of hot spots do not vary significantly. Therefore, as a first approximation we calculate the light curves by fixing the hot spots at $t = 5$ and rotating the star.

The observed intensity of radiation in the direction $\hat{\mathbf{k}}$ is $J = \int f(\mathbf{R}, \mathbf{k}) \mathrm{d}S$, where $f(\mathbf{R}, \hat{\mathbf{k}})$ is the intensity of the radiation from a unit area into the solid angle element $d\Omega$ in the direction $\hat{\mathbf{k}}$, dS is an element of the surface area of the star, $\mathbf{R}$ is the radius vector. It can be calculated from our simulations (see details in Romanova et al. 2004).

Figure 4.8 shows the light curves for a pure dipole, pure quadrupole and a dipole plus quadrupole case at $\Theta = 30^\circ$ at different inclination angles from $i = 15^\circ$ to 90°. The inclination angles are measured relative to the star's rotation axis. One can see that for the pure dipole case (top panel) the observer will see only one peak per period, excluding the case of very high inclination angles, $i \geq 70^\circ$. In the pure quadrupole case (middle panel), the observer will see two peaks per period starting from smaller inclination angle, $i \geq 40^\circ$. In the case of the mixed dipole plus quadrupole field, there are also two peaks per period at $i \geq 40^\circ$.

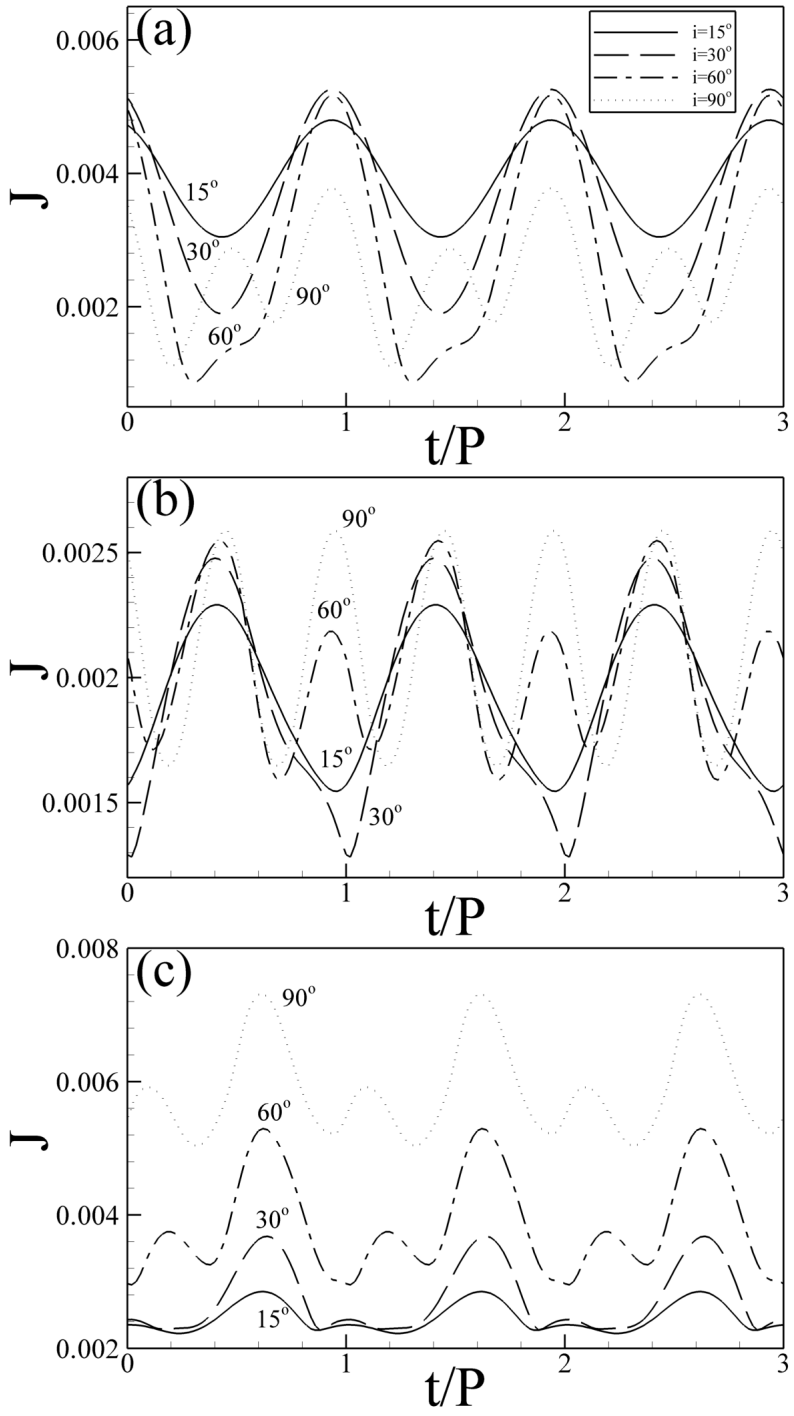

Figure 4.8: Light curves for different magnetic field configurations at misalignment angle $\Theta = 30°$ for different inclination angles i. The inclination angle is measured relative to the star's rotation axis. Solid, dash, dash-dot and dotted lines represent the results for $i = 15°$, $i = 30°$, $i = 60°$, $i = 90°$ respectively. (a) Pure dipole case $\mu = 0.5$, $D = 0$; (b) Pure quadrupole case $\mu = 0$, $D = 0.5$; (c) dipole plus quadrupole case at $\mu = 0.5$, $D = 0.5$.

Also, when the inclination angle is changed, the change in amplitude is stronger in this case. If the inclination angle of the star is known, one can derive the magnetic configurations by varying Θ. However, there may be several possible configurations of the field and Θ which give similar light curves.

4.5 Dependence on the Strength of the Quadrupole Component

Here, we consider the dependence of different features of the accretion flow and hot spots on the strength of the quadrupole component. We fixed the dipole component at $\mu = 0.5$ and varied the quadrupole component between $D = 0$ and $D = 2.5$. First, we calculated the mass accretion rate $\dot{M} = -\int d\boldsymbol{S} \cdot \rho \boldsymbol{v}_p$ along the surface of the star $\boldsymbol{S}$ and observed that accretion rate varies by different way but on average it does not depend on the value of the quadrupole component (see Figure 4.9a). This is an expected result, because the accretion rate should depend on the viscous properties of the disk but not on magnetic configurations of the star. All simulations were done at the same parameters of the disk and fixed value of $\alpha-$viscosity, $\alpha = 0.04$. We should note that initially, during the first 1-2 rotations accretion rate is very small. This is the time when matter moved towards the disk and reached the surface of the star through the funnel streams. Later, the structure of the spots establishes and varies only slightly with time. At present, we are able to simulate accretion to a star with a quadrupole field during $5 - 50$ rotations. We show the plot in Figure 4.9 up to $t = 5$ because the spots do not change appreciably for longer times.

We also calculated the spinning torque to the star from the disc-

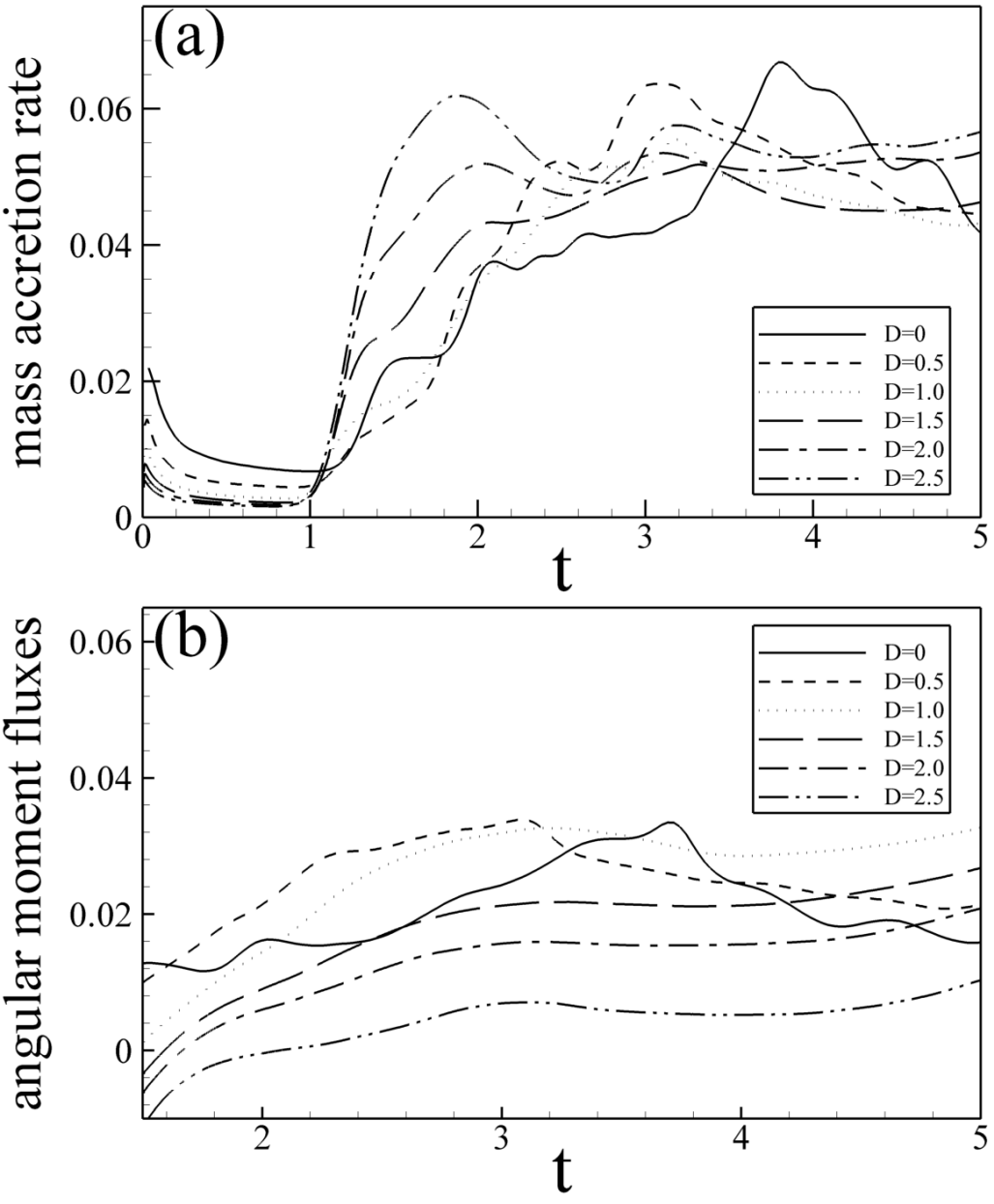

Figure 4.9: Mass accretion rate $\dot{M}$ (a) and angular momentum fluxes $\dot{L}_f$ (b) for stars with different strength of quadrupole moment which changes from $D = 0$ to $D = 2.5$, while $\mu = 0.5$, $\Theta = 30^\circ$ and other parameters are fixed.

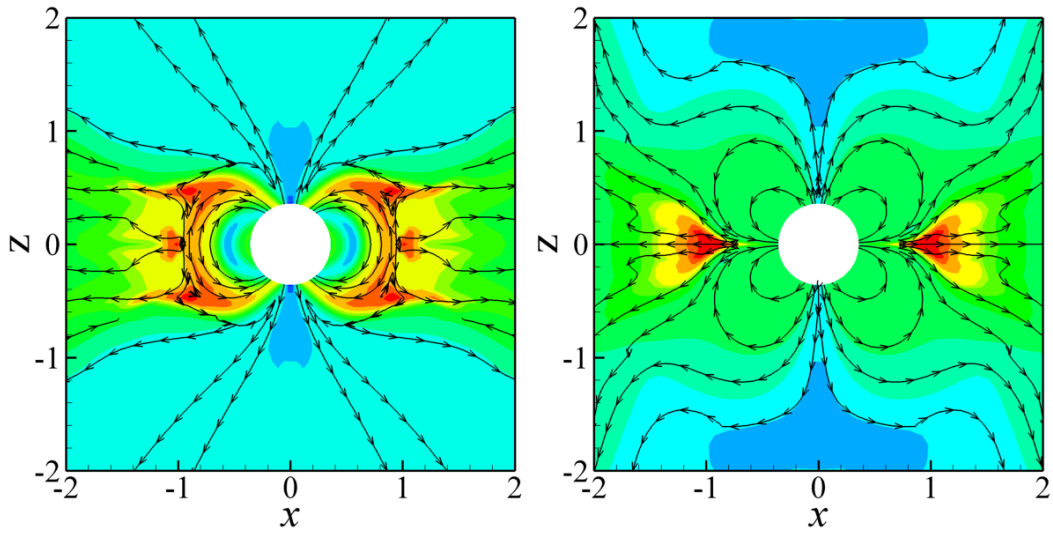

Figure 4.10: Figure shows streamlines of angular momentum flux carried by the magnetic field lines $\boldsymbol{f_B} = rB_\phi \boldsymbol{B}_p/4\pi$ in the cases of the pure dipole field at $\mu = 0.5$ (left panel) and pure quadrupole field $D = 0.5$ (right panel) at $\Theta = 0$. The background shows the angular velocity distribution where angular velocity varies from $\Omega = 0.4$ (red) to $\Omega = 0.01$ (blue).

magnetosphere interaction. The main spinning torque comes from the magnetic field lines connecting a star with the disk and corona $\dot{L}_f = \int d\boldsymbol{S} \cdot rB_\phi \boldsymbol{B}_p/(4\pi)$ (see also Figures 4.5 and 4.6). A star rotates relatively slowly (co-rotation radius is $r_{cr} = 2$) and magnetospheric radius is smaller than co-rotation radius ($r_m \approx 1$) so that the inner regions of the disk rotates faster than the star and accreting matter spins the star up through the closed field lines connecting a star with the disc.

There is also a negative torque from the open field lines which start in the polar regions and connect a star with slowly rotating corona. This torque leads to spinning-down, but this torque is smaller compared to the spin-up torque. Figure 4.9b (solid line) shows the torque in the case of the pure dipole star. When we added small quadrupole component, then torque stayed approximately the

same. However, when we added the largest quadrupole component ($D = 2$ and 2.5) then the positive torque decreased significantly. Analysis of angular momentum fluxes in the pure dipole and quadrupole cases have shown that in the dipole case the main positive torque comes through the inner closed field lines which connect the disk and the star. Disc rotates faster than the star and angular momentum flows to the star. In the quadrupole case disk matter flows through the equatorial belt and there is less "communication" between the star and the disc. This is why in quadrupole case the positive torque is smaller. This explains the fact that at very large quadrupole component the spinning torque is smaller: the field structure becomes very similar to a pure quadrupole topology and the disk accretes through a quadrupole belt.

We investigated the angular momentum flow in greater detail in the cases of pure dipole field ($\mu = 0.5$, $D = 0$) and pure quadrupole field ($D = 0.5$, $\mu = 0$). Figure 4.10 shows the distribution of the angular velocity (background) and streamlines of the angular momentum fluxes carried by the magnetic field $\boldsymbol{f_B} = rB_\phi \boldsymbol{B}_p/4\pi$. One can see that in the dipole case, angular momentum flows in from the disk to the star (the star spins-up), and flows out through the open polar field lines into the corona. In the case of the quadrupole field, angular momentum flows to the star from the quadrupolar equatorial belt, where the disk matter accretes and is threaded by some closed field lines of the quadrupole. This is the region where the inward angular momentum flux is the largest. Again, there is angular momentum outflow from the star through the open polar field lines. In both cases the total angular momentum transferred to the star is positive and the star spins-up. We should note that the angular momentum carried to the star by matter is much smaller than that associated with the field, by a factor of 20-100 in the dipole case and 10-20 in the quadrupole case.

In addition we investigated different properties of the hot spots in cases of aligned ($\Theta = 0^\circ$) pure dipole and pure quadrupole configurations at equal magnetic moments, $\mu = 0.5$ and $D = 0.5$. In the case of an accreting dipole the matter of the funnel stream is lifted above the magnetosphere and then is accelerated towards the surface of the star, so that significant part of gravitational energy is released thus increasing the temperature of the hot spots (see Romanova et al. 2004). In the case of predominantly quadrupole field matter flows through the equatorial belt without such dramatic falling to the surface of the star. The simulations show that the velocity of the flow and the Mach number are about two times smaller in the quadrupole case. The luminosity of hot spots depends on the density and velocity. The density is similar in both dipole and quadrupole-dominated cases, difference in velocities leads to conclusion that the hot spots are expected to be $(v_d/v_q)^2$ times dimmer in the quadrupole case. The temperature of the hot spots is expected to be smaller in the quadrupole case by the factor $(v_d/v_q)^{3/4}$ (about 1.7 times) which follows from equating of the kinetic energy flux to the black-body radiation flux. In both cases the maximum energy and highest temperature are in the middle of the spot. Thus, a star with pure dipole case is expected to have hotter and more luminous spots.

4.6 Summary

We investigated for the first time disk accretion to a star with a dipole plus quadrupole field in full 3D MHD simulations. The simulations show that for relatively small misalignment angles Θ, matter flows in a thin wide sheet to the quadrupole's belt. This flow forms a ring-like hot spot at the surface of the star. The position of the ring coincides with magnetic equator in the case of the pure

quadrupole field, and is displaced into the southern hemisphere in the case of the dipole plus quadrupole fields. At large Θ, most of matter may accrete to one or both magnetic poles. In quadrupole case the light curves typically show two peaks per period for the majority of inclination angles *i*. This might be a sign of the significant quadrupole component. However in the case of pure dipole field two peaks per period are typical for the case of high inclination of the system (Romanova et al. 2004). If inclination of the systems is known, then the light curves may help to suggest the possible role of the quadrupole component.

The simulations show that the torque on the star is larger in the case of the dipole field, where angular momentum is transferred through the closed field lines connecting the star and the disc. In the quadrupole case the torque is smaller because matter of the disk accretes directly to the star through the quadrupole belt, that is, between field lines. There is a positive torque associated with the disc-magnetosphere interaction, however it is much smaller than in pure dipole case.

In the case of the dominant quadrupole field, the hot spots are expected to be cooler with smaller total energy released because in the quadrupole belt the funnel flow hits the star with smaller velocities compared to the pure dipole case. To apply these predictions, one needs to know the accretion rate and the value of the magnetic field on the surface of the star.

In reality the star's magnetic field may be even more complicated and may include higher order multipoles. In such a field multiple funnel streams are expected to form (Donati et al. 2006; Jardine et al. 2006). Such multipolar fields were recently modeled by von Rekowski and Brandenburg (2006) in the axisymmetric time-dependent simulations which incorporated the dynamo processes

of the field formation both in the disk and in the star. In the case of multipolar fields the light curves are expected to be even more complicated. The light curves obtained in this paper and the light curves obtained earlier for pure dipole field (Romanova et al. 2004) may help to distinguish the cases where the magnetic field is highly ordered (dipole or dipole plus quadrupole) from the cases of the multipolar field where the light curves are expected to be much less ordered. In the future research we plan to investigate the case where the dipole and quadrupole are misaligned and also the case of accretion to a star with higher order multipolar magnetic field.

CHAPTER 5

ACCRETION TO STARS WITH COMPLEX MAGNETIC FIELDS*

Disk accretion to rotating stars with complex magnetic fields is investigated using full three-dimensional magnetohydrodynamic (MHD) simulations. The studied magnetic configurations include superpositions of misaligned dipole and quadrupole fields and off-centre dipoles. The simulations show that when the quadrupole component is comparable to the dipole component, the magnetic field has a complex structure with three major magnetic poles on the surface of the star and three sets of loops of field lines connecting them. A significant amount of matter flows to the quadrupole "belt", forming a ring-like hot spot on the star. If the maximum strength of the magnetic field on the star is fixed, then we observe that the mass accretion rate, the torque on the star, and the area covered by hot spots are several times smaller in the quadrupole-dominant cases than in the pure dipole cases. The influence of the quadrupole component on the shape of the hot spots becomes noticeable when the ratio of the quadrupole and dipole field strengths $B_q/B_d \gtrsim 0.5$. It becomes dominant in determining the shape of the hot spots when $B_q/B_d \gtrsim 1$. We conclude that if the quadrupole component is larger than the dipole one, then the shape of the hot spots is determined by the quadrupole field component. In the case of an off-centre dipole field, most of the matter flows through a one-armed accretion stream, forming a large hot spot on the surface, with a second much smaller secondary spot. The light curves may have simple, sinusoidal shapes, thus mimicking stars with pure dipole fields. Or, they may be complex and unusual. In some cases the light curves may be indicators of a complex field, in

*This chapter is based on the paper by Long et al. 2008 (arxiv:0802:2308), accepted for publication in the Monthly Notices of the Royal Astronomical Society. It is rewritten here with minor changes.

particular if the inclination angle is known independently. We also note that in the case of complex fields, magnetospheric gaps are often not empty, and this may be important for the survival of close-in exosolar planets.

5.1 Introduction

The magnetic field of a rotating star can have a strong influence on the matter in an accretion disk. The field can disrupt the disk and channel the accreting matter to the star along the field lines. The associated magnetic activity can be observed through photometric and spectral measurements of different types of stars, like young solar-type Classical T Tauri stars (CTTSs) (Hartmann et al. 1994), X-ray pulsars and millisecond pulsars (Ghosh & Lamb 1978; Chakrabarty et al. 2003), cataclysmic variables (Wickramasinghe et al. 1991; Warner 1995, 2000), and also brown dwarfs (e.g., Scholz & Ray 2006). The topology of the stellar magnetic field plays an important role in disk accretion and in the photometric and spectral appearance of the stars.

The dipole magnetic model has been studied since Ghosh & Lamb (1979a,b), both theoretically and with 2D and 3D MHD simulations. However, the intrinsic field of the star may be more complex than a dipole field. Safier (1998) argued that the magnetic field of CTTSs may be strongly non-dipolar. Zeeman measurements of the magnetic field of CTTSs based on photospheric spectral lines show that the strong (1 – 3 kG) magnetic field is probably not ordered, and indicates that the field is non-dipolar close to the star (Johns-Krull et al. 1999, 2007). Other magnetic field measurements with the Zeeman-Doppler imaging technique have shown that in a number of rapidly rotating low-mass stars, the magnetic field has a complicated multipolar topology close to the star (Donati

& Cameron 1997; Donati et al. 1999; Jardine et al. 2002). Recently, observations from the ESPaDOnS/NAVAL spectropolarimeter (Donati et al. 2007a) revealed that the magnetic field geometry of CTTSs BP Tau, V2129 Oph and SU Aur is more complex than dipole.

Theoretical and numerical research has been done on accretion to a rotating star with a non-dipole field. Jardine et al. (2006) investigated the possible paths of the accreting matter in the case of a multipolar field derived from observations. Gregory et al. (2006) developed a simplified stationary model for such accretion. von Rekowski and Brandenburg (2006) did axisymmetric simulations, and von Rekowski and Piskunov (2006) did 3D simulations of the disk-magnetosphere interaction in the case where the magnetic field is generated by dynamo processes in both the star and the disk. They obtained a time-variable magnetic field of the star with a complicated multipolar configuration which shows that the dynamo may give rise to a complex magnetic field structure. Recent observations and analysis of the magnetic field and brightness distribution on the surface of CTTSs suggest that the magnetic field is predominantly octupolar with strength $B_{oct} \sim 1.2$ kG and a much smaller dipole component $B_d \sim 0.35$ kG (Donati et al. 2007b). Most of the accretion luminosity is concentrated in a large spot close to the magnetic pole. Such observations are interesting and can be compared with different 3D MHD simulation models. Here we investigate, using 3D MHD simulations, disk accretion to rotating stars with dipole plus *quadrupole* fields and off-centre dipole fields.

In our earlier work we performed full 3D simulations of disk accretion to stars with pure quadrupole and *aligned* dipole plus quadrupole fields (Long, et al. 2007) and found that the funnel streams and associated hot spots have

different features compared with the case of accretion to a star with pure dipole field. When the quadrupole component is significant, matter always accretes to a quadrupole "belt" and forms a ring-like hot spot on the surface of the star.

In this paper we show the results of full 3D MHD simulations of accretion to stars with more complex magnetic fields. Compared with Long et al. (2007), we consider the more general case where the dipole and quadrupole are *misaligned*. Also, we consider the case of accretion to a star with internal point dipoles displaced from the star's center. Further, we performed a set of simulations with the aim of understanding the properties of stars with different contributions from the dipole and quadrupole components.

One point of interest is to determine the how the area of the star's surface covered by hot spots depends on the the quadrupole/dipole ratio. A further point of interest is to determine how the torque on the star depends on the structure of the field. That is, we can compare the torque for cases with a complex field with those having a dipole field. We discuss all these points in §5.4. We calculate the light curves and discuss the use of the light curves to investigate the structure of the magnetic field of the star. The conclusions and discussion of possible applications of our results are given in §5.5. Some high resolution figures and animations are available at http://www.astro.cornell.edu/~long.

5.2 The Magnetic Configurations

Combination of Dipole and Quadrupole Fields: The intrinsic magnetic field of the star is $\mathbf{B} = -\nabla\varphi$, where the scalar potential of the magnetic field is $\varphi(\mathbf{r}) = \Sigma m_a/|\mathbf{r} - \mathbf{r}_a|$, m_a is the magnetic "charge" analogous to the electric charge, and $\mathbf{r}$

and $\mathbf{r}_a$ are the positions of the observer and the magnetic "charges" respectively. The scalar potential can be represented as a multipole expansion in powers of $1/r$ and the quadrupole term is

$$\varphi^{(2)} = D_{\alpha\beta} n_\alpha n_\beta / 2r^3,$$

where $n_\alpha = x_\alpha / r$, x_α are the components of $\mathbf{r}$, $D_{\alpha\beta}$ is the magnetic quadrupole moment tensor, summation over repeated indices is implied, and $D_{\alpha\alpha} = 0$. In the *axisymmetric* case where $D_{11} = D_{22} = -D_{33}/2$, let $D = D_{33}$ be the value of the quadrupole moment and refer to the axis of symmetry as the "direction" of the quadrupole moment, so we have the quadrupole moment $\boldsymbol{D}$. The combination of dipole and quadrupole magnetic fields can be written as:

$$\mathbf{B}(\mathbf{r}) = \frac{3(\boldsymbol{\mu} \cdot \hat{\mathbf{r}})\hat{\mathbf{r}} - \boldsymbol{\mu}}{r^3} + \frac{3D}{4r^4}(5(\hat{\mathbf{D}} \cdot \hat{\mathbf{r}})^2 - 1)\hat{\mathbf{r}} - \frac{3D}{2r^4}(\hat{\mathbf{D}} \cdot \hat{\mathbf{r}})\hat{\mathbf{D}}, \tag{5.1}$$

where $\hat{\mathbf{r}}$ and $\hat{\mathbf{D}}$ are the unit vectors for the position and the quadrupole moment respectively. In general, the dipole and quadrupole moments $\boldsymbol{\mu}$ and $\boldsymbol{D}$ are misaligned relative to the rotational axis $\boldsymbol{\Omega}$, at angles Θ and Θ_D respectively. In addition, they can also be in different meridional planes with an angle Φ between the $\boldsymbol{\Omega} - \boldsymbol{\mu}$ and $\boldsymbol{\Omega} - \boldsymbol{D}$ planes.

The values of μ and D determine the magnetic field strength on the star's surface. For example, if $\boldsymbol{\mu}$ and $\boldsymbol{D}$ are aligned with the rotational axis $\boldsymbol{\Omega}$, and $\mu = 0.5$, $D = 0.5$, then the strength of the dipole component on the north pole of the star is $B_{*d} = 0.32$ kG, and the quadrupole one is $B_{*q} = 0.68$ kG.

Off-centre Magnetic Configurations: The magnetic field of a star may deviate from the center of the star. Such displacement naturally follows from the dynamo mechanism of magnetic field generation. If the dipole and quadrupole moments are displaced by $\boldsymbol{a}$ and $\boldsymbol{b}$ from the center of the star, we can replace $\boldsymbol{r}$

with $(\boldsymbol{r} - \boldsymbol{a})$ and $(\boldsymbol{r} - \boldsymbol{b})$ in the corresponding terms in Eqn. 1 to obtain the magnetic field around the star. In this paper we investigate accretion to a displaced dipole and to a set of displaced dipoles.

5.3 Accretion to Stars with Different Complex Magnetic Fields Configurations

In Long et al. (2007), we have shown results of accretion to stars with dipole plus quadrupole fields with aligned axes. In this section, we present simulation results of accretion to a star with *misaligned* dipole plus quadrupole magnetic fields. First, we consider the configuration when the dipole magnetic moment $\boldsymbol{\mu}$ is aligned with the stellar spin axis $\boldsymbol{\Omega}$, that is, $\Theta = 0^\circ$, but the quadrupole magnetic moment $\boldsymbol{D}$ is inclined relative to the spin axis at an angle $\Theta_D = 45^\circ$. Next, we consider a more general configuration when $\boldsymbol{\mu}$, $\boldsymbol{D}$ and $\boldsymbol{\Omega}$ are all misaligned relative to each other, and there is an angle Φ between the $(\boldsymbol{\Omega} - \boldsymbol{\mu})$ and $(\boldsymbol{\Omega} - \boldsymbol{D})$ planes. To ensure that the case is general enough to represent a possible situation in nature, we choose $\Theta = 30^\circ$, $\Theta_D = 45^\circ$ and $\Phi = 90^\circ$.

The strengths of the dipole and quadrupole moments are the same in both cases, $\mu = D = 0.5$. Here we choose a quite strong quadrupole component to get an example of a complex magnetic field, so that the disk is disrupted not by the dipole component only but by the superposition of the dipole and quadrupole fields. Figure 5.1 shows the distribution of magnetic fields for these two cases in $+x$ direction. We can see that the quadrupole component is still comparable to the dipole component at $r \sim 1$ where the disk is stopped by the magnetosphere (see Figure 5.5). This means that both dipole and quadrupole contribute to stop

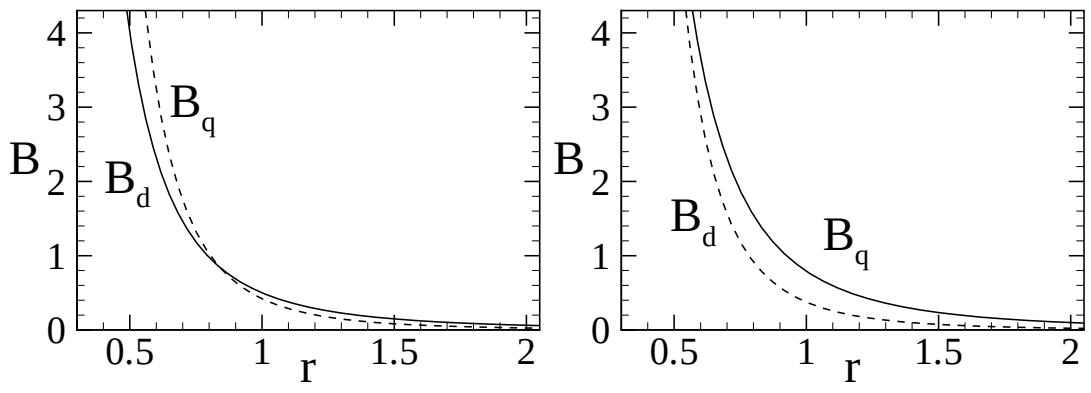

Figure 5.1: The distribution of dipole and quadrupole components of magnetic fields. The left-hand panel represents the case when $\mu = D = 0.5$, $\Theta = 0°$,$\Theta_D = 45°$; the right-hand panel represents the case when $\mu = D = 0.5$, $\Theta = 30°$, $\Theta_D = 45°$, $\Phi = 90°$. The strengths of the quadrupole and dipole are comparable at $r \sim 1$ where the disk is stopped by the magnetosphere.

the disk.

5.3.1 Misaligned Dipole plus Quadrupole Configurations

Now we consider the configuration when the ($\boldsymbol{\Omega - \mu}$) and ($\boldsymbol{\Omega - D}$) planes coincide: $\mu = D = 0.5$, $\Theta = 0°$, $\Theta_D = 45°$. Figure 5.2 shows the strength of the magnetic field on the surface of the star in different projections. One can see that the field is not symmetric and shows three strong magnetic poles and a much weaker magnetic pole with different polarities on the surface, due to the asymmetry of the misaligned dipole plus quadrupole configuration. The left-hand panel shows a strong positive magnetic pole (red) with $B = 67$ (dimensionless value) and a strong negative pole (dark blue) with $B = -41$. The middle panel shows a second strong positive pole (yellow) with $B = 35$, and in fact a very weak

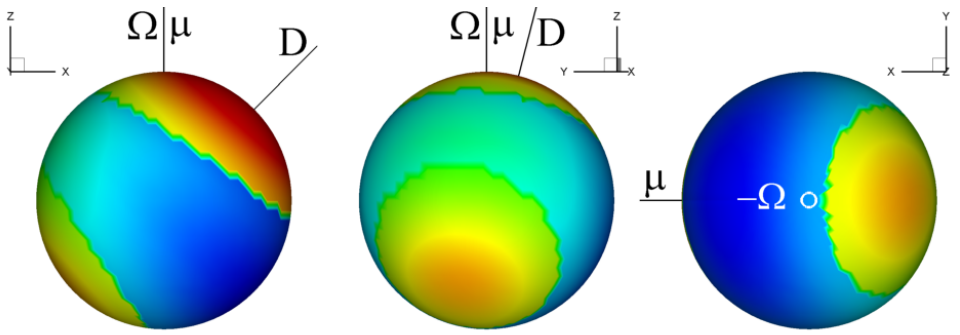

Figure 5.2: The strength of the magnetic field on the surface of the star for the case $\mu = 0.5$, $D = 0.5$, $\Theta = 0°$, $\Theta_D = 45°$ at different projections: from the equatorial plane (left-hand panel), close to the *yz* plane (middle panel), and from the south pole (right-hand panel). The red and blue regions represent different strength and polarities. The strength varies from the most blue point $B = -41$ to the most red point $B = 67$ (dimensionless value, see Tab. 2.1) and reaches $B = 0$ at the boundary between the yellow and green areas.

and small negative pole in the middle of the surface with $B = -7$ (dark green). We should note that the strength of the magnetic field around this weak pole is more negative than at the pole. The right-hand panel shows both the strong negative pole (dark blue) which is extended and the second strong positive pole (yellow).

Figure 5.3 shows a three-dimensional (3D) view of the structure of the magnetic field lines. The color shows the different strengths and polarities of the magnetic field lines, from maximum positive (red) to maximum negative (blue) values. The magnetic field lines are more complex than in the aligned dipole plus quadrupole case. Now we see three sets of loops of closed field lines in the region near the star, connecting the three major poles and the weaker pole on the star, which is different from the one big and one small loops of field lines

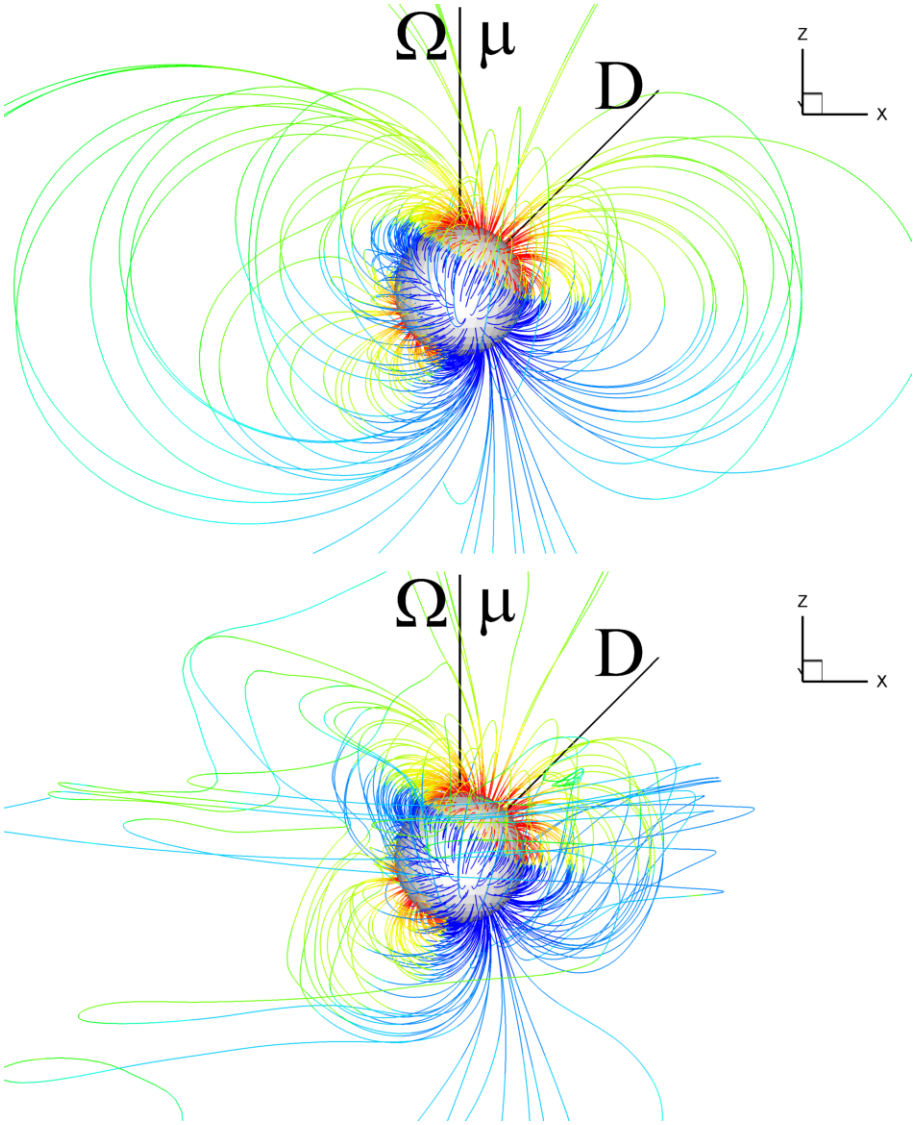

Figure 5.3: The complex magnetic field lines for the case $\mu = 0.5$, $D = 0.5$, $\Theta = 0°$, $\Theta_D = 45°$, at $t = 0$ (top panel) and $t = 8$ (bottom panel). The strength of the magnetic field along the field lines varies from red (positive magnetic pole) to blue (negative pole).

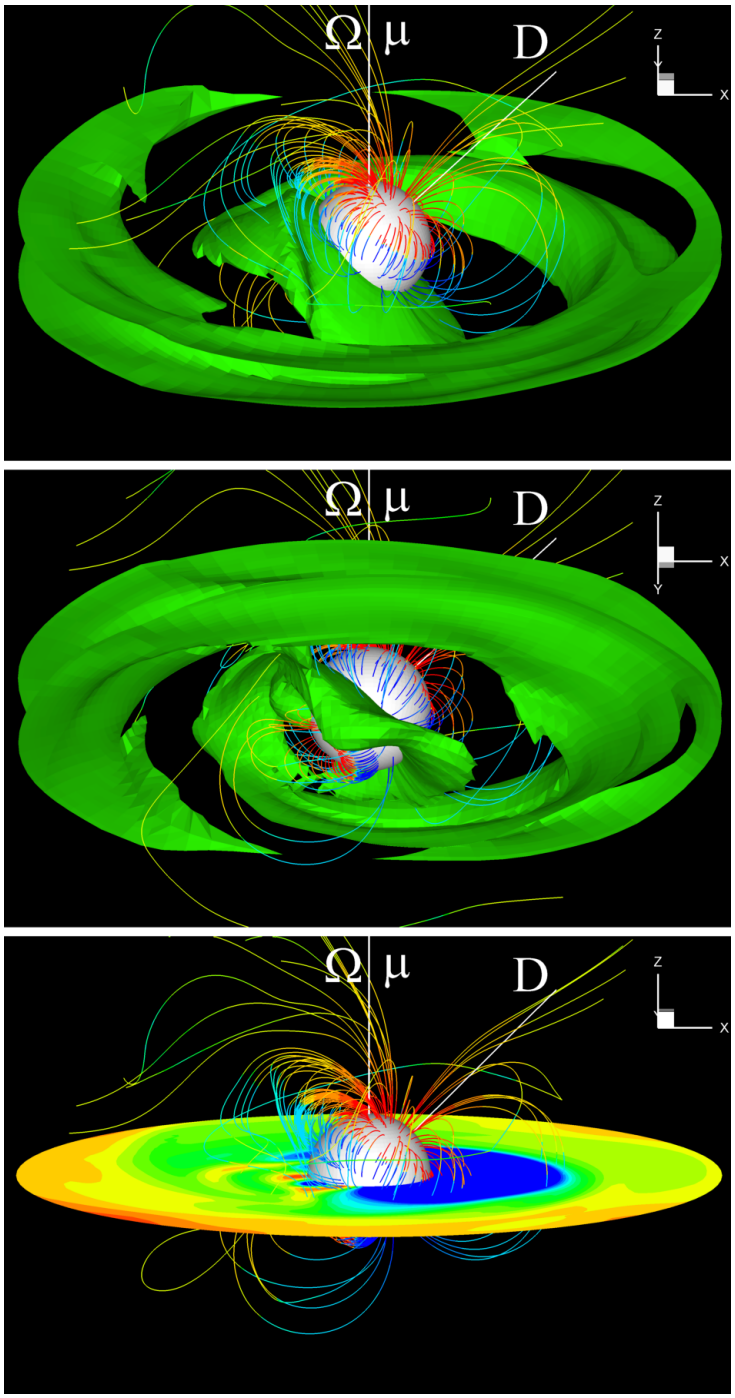

Figure 5.4: 3D views of matter flow to the star for the case $\mu = 0.5$, $D = 0.5$, $\Theta = 0°$, $\Theta_D = 45°$, at $t = 8$. The top panel shows the view from the north, the middle panel from the south. The green surface is a constant density surface, $\rho = 0.27$ (dimensionless value). The bottom panel shows the equatorial plane. The colors of the magnetic field lines correspond to those in Figure 5.3. Only the inner part of the simulation region is shown.

shown in the aligned dipole plus quadrupole case (Long et al. 2007).

Figure 5.4 shows a 3D view of matter flow around the star. The disk matter is disrupted by the complex field and is lifted above the equatorial plane at the magnetospheric radius $r = r_m$, where the magnetic stress balances the matter stress, $\beta = (p + \rho v^2)/(B^2/8\pi) = 1$. We can see that most of the matter flows between the loops of field lines to the extended negative magnetic pole by choosing the shortest path which is energetically favorable, forming a modified quadrupole "belt". This "belt" has a different shape from that in the case of aligned dipole plus quadrupole configurations (see Long et al. 2007), which looks like a more "regular" sheet perpendicular to the magnetic axis. Here, the "belt" is twisted, although it is approximately perpendicular to the quadrupole axis. The bottom panel shows a slice in the equatorial plane, and we can see that in the $-x$ direction, the matter penetrates between field lines to the surface of the star.

Figure 5.5 shows different projections of the accretion flow. One can see that the matter flow is not symmetric in the *xz* and *xy* planes. The *xz* projection shows that in $-x$ direction, the magnetic stress is weak due to the combination of the dipole and tilted quadrupole components, so that the matter is not lifted, and flows almost directly to the surface of the star, and the equatorial plane does not have the magnetospheric gap which is typical for pure dipole cases. Because the quadrupole moment is inclined at 45° relative to the $z-$ axis in *xz* plane, in the $+x$ direction, there is one set of closed loops of magnetic field lines, which stops the disk and forms a magnetospheric gap. Comparison of the dipole and quadrupole components in the $+x$ direction shows that in the region where the disk stops ($\beta = 1$), the dipole and quadrupole components are approximately

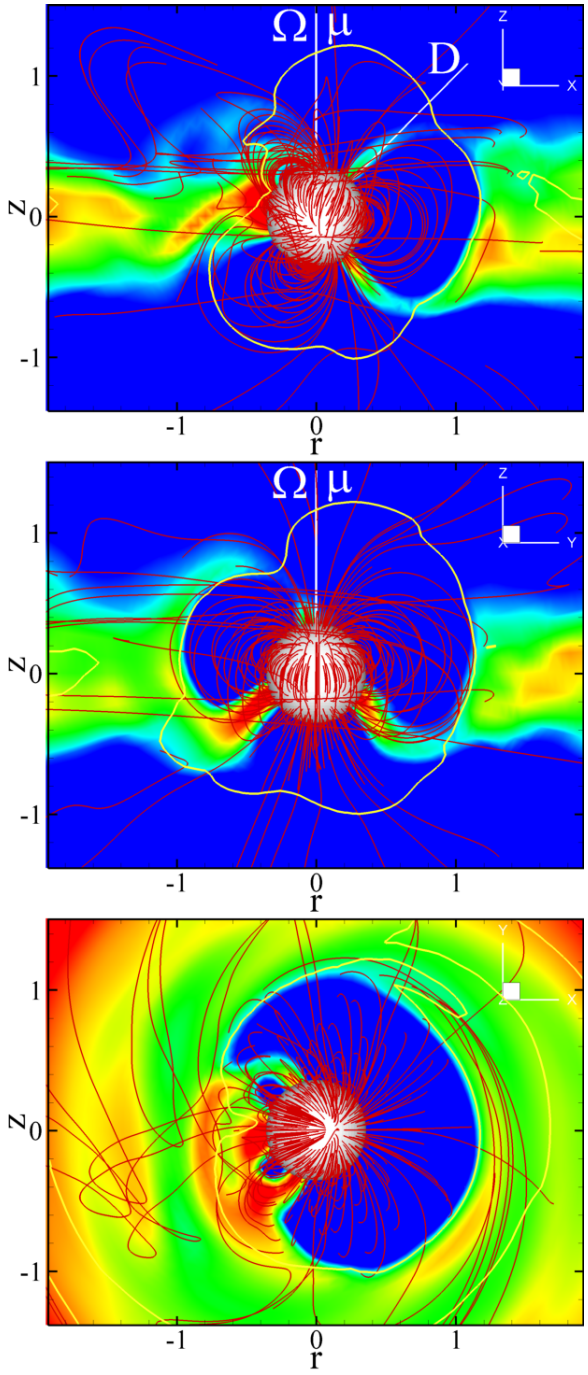

Figure 5.5: Disk accretion viewed from different projections for the case of μ = 0.5, D = 0.5, Θ = 0°, Θ_D = 45°. The top panel shows the projection in xz plane, the middle panel in the yz plane, and the bottom panel in the xy plane. The color background shows the density distribution varying from ρ = 0.01 (blue) to ρ = 1.9 (red), and the magnetic field lines are shown in red. The yellow lines correspond to β = 1.

equal, so that the quadrupole has a strong influence on the matter flow, which is clearly seen from the above figures. In the *yz* projection, the matter flow is relatively symmetric because $\boldsymbol{\Omega}$, $\boldsymbol{\mu}$ and $\boldsymbol{D}$ are all in the *xz* plane. In the *xy* projection, we can see that there is a gap in $+x$ direction where there is no direct matter flow, but there is no gap in the $-x$ direction.

Figure 5.6 shows the hot spots on the surface of the star at $t = 8$. One can see that there is a ring-like hot spot and a small round hot spot nearby. There is no clear hot spot near the positive part of the $\boldsymbol{D}$ and $\boldsymbol{\Omega}$ axes, due to the weak funnel stream in the northern hemisphere. The ring-like hot spot comes from accretion to the quadrupole "belt", which is approximately symmetric relative to $\boldsymbol{D}$ because the quadrupole magnetic component B_q is stronger than the dipole component B_d in the region close to the star. A small round spot forms as a result of the connection of field lines between the weak magnetic pole ($B = -7$) and the nearby region where B is positive. Part of the matter flows to the south and forms this round hot spot.

We calculated the light curves from the hot spots on the rotating star's surface. Assuming the total energy of the inflowing matter is radiated isotropically as blackbody radiation, we obtain the flux of the radiation in a direction $\hat{\boldsymbol{k}}$,

$$J = r^2 F_{obs} = \int I(\boldsymbol{R}, \hat{\boldsymbol{k}}) \cos\theta \mathrm{d}S, \tag{5.2}$$

where r is the distance between the star and the observer, F_{obs} is the observed flux, $I(\boldsymbol{R}, \hat{\boldsymbol{k}})$ is the specific intensity of the radiation from a position $\boldsymbol{R}$ on the star's surface into a solid angle element $\mathrm{d}\Omega$ in the direction $\hat{\boldsymbol{k}}$, $\theta = \arccos(\boldsymbol{R} \cdot \hat{k})$, $\mathrm{d}S$ is an element of the surface area. The specific intensity can be obtained as

$$I(\boldsymbol{R}, \hat{\boldsymbol{k}}) = \frac{1}{\pi} F_e(\boldsymbol{R}) \cos\theta, \tag{5.3}$$

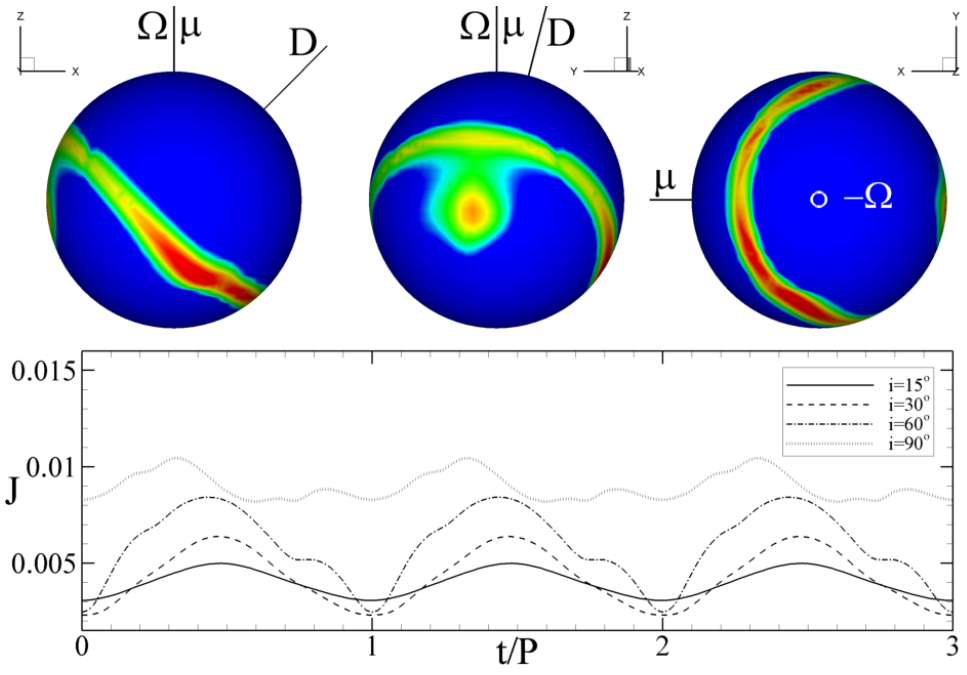

Figure 5.6: The hot spots viewed at different angles: from the rotational equatorial plane (left-hand panel); from near the *yz* plane (middle panel); and from the south pole (right-hand panel). The red color corresponds to the densest region with maximum density $\rho = 1.4$ (dimensionless value). The bottom panel shows the light curves for different inclination angles.

where $F_e(\boldsymbol{R})$ is the total energy flux of the inflowing matter. In our simulations, J is the received energy per unit time, and the dimensionless value of J is in units of $\dot{E}_0$ which is shown in Tab. 2.1 and discussed in §2.3.5. The hot spots constantly change their shape and location. However, our 3D simulations show that the changes are relatively small. So we choose the hot spots at some moment of time, fix them, and rotate the star to obtain the light curves. The bottom panel of Figure 5.6 shows the light curves at $t = 8$ for different inclination angles $i = \arccos(\hat{\boldsymbol{\Omega}} \cdot \hat{\boldsymbol{k}})$. One can see that the light curve is approximately sinusoidal for small inclination angles. This is because the observer can only see a part of

the ring-like hot spots at this time and the sinusoidal shape is determined by the rotation of the spots with the star. One can see that the shapes of the light curves at $i = 60°$ and $90°$ are unusual and do not correspond to any pure dipole field case (Romanova et al. 2004). When i increases, the small round hot spot and more of the ring-like hot spots can be observed, and consequently the peak intensity and variability of the light curves are larger.

5.3.2 A more general case: $\boldsymbol{\mu}$, $\boldsymbol{D}$, $\boldsymbol{\Omega}$ all misaligned

Next we investigate the more general case when the dipole moment $\boldsymbol{\mu}$, quadrupole moment $\boldsymbol{D}$ and spin axis $\boldsymbol{\Omega}$ of the star are all misaligned relative to each other: $\mu = 0.5$, $D = 0.5$, $\Theta = 45°$, $\Theta_D = 30°$ and $\Phi = 90°$.

Figure 5.7 shows the distribution of the magnetic field on the surface of the star. We can again see that there are three dominant magnetic poles with magnetic strengths $B = 65, B = 37$ and $B = -44$ respectively. There is another weak magnetic pole in the middle region shown in the middle panel, but it shrinks and partially merges into the boundary of the nearby pole and looks smaller than that in the previous case.

Figure 5.8 shows 3D plots of matter flow at $t = 8$. In the top panel, one can see that again, a significant amount of matter flows through the quadrupole "belt" below the loops of field lines, because the quadrupole component dominates near the star. And a single strong stream flows to the region nearby the north pole. So it could be expected that ring-like hot spots and round hot spots form on the surface of the star. The bottom panel shows a slice in the xy plane. One can see that some matter can flow to the star directly without leaving the

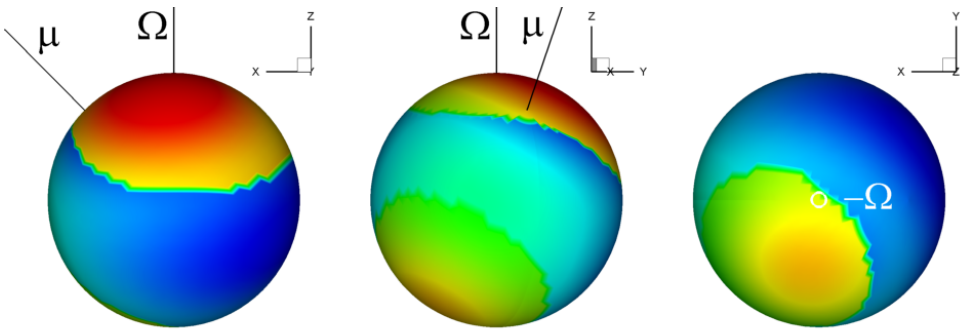

Figure 5.7: Distribution of the magnetic field strength on the star's surface for the case $\mu = 0.5$, $D = 0.5$, $\Theta = 45°$, $\Theta_D = 30°$ and $\Phi = 90°$ at different projections: from the equatorial plane (left-hand panel), from near the *yz* plane (middle panel), and from the south pole (right-hand panel). Red and blue colors show positive and negative polarities. The magnetic strength varies from $B = -44$ to $B = 65$.

equatorial plane. We also can see three sets of loops of field lines.

Figure 5.9 shows different projections of the matter flow. The matter flow is no longer symmetric in any projection which is expected due to the magnetic configuration. In the *xy* and *yz* planes, we also can see that there are three sets of loops of field lines which regulate the shape of the accretion flow. In the northern hemisphere, some matter is lifted from the equatorial plane and flows to the high-latitude area near the dipole axis. This is because the accretion disk is close to one of the major magnetic poles in this direction. In the southern hemisphere, matter penetrates the β line between loops of field lines, and forms a modified quadrupole "belt". The magnetosphere is not empty in the *xy* plane, and matter can go directly to the star in some directions.

Figure 5.10 shows the hot spots and the associated light curves. We can see

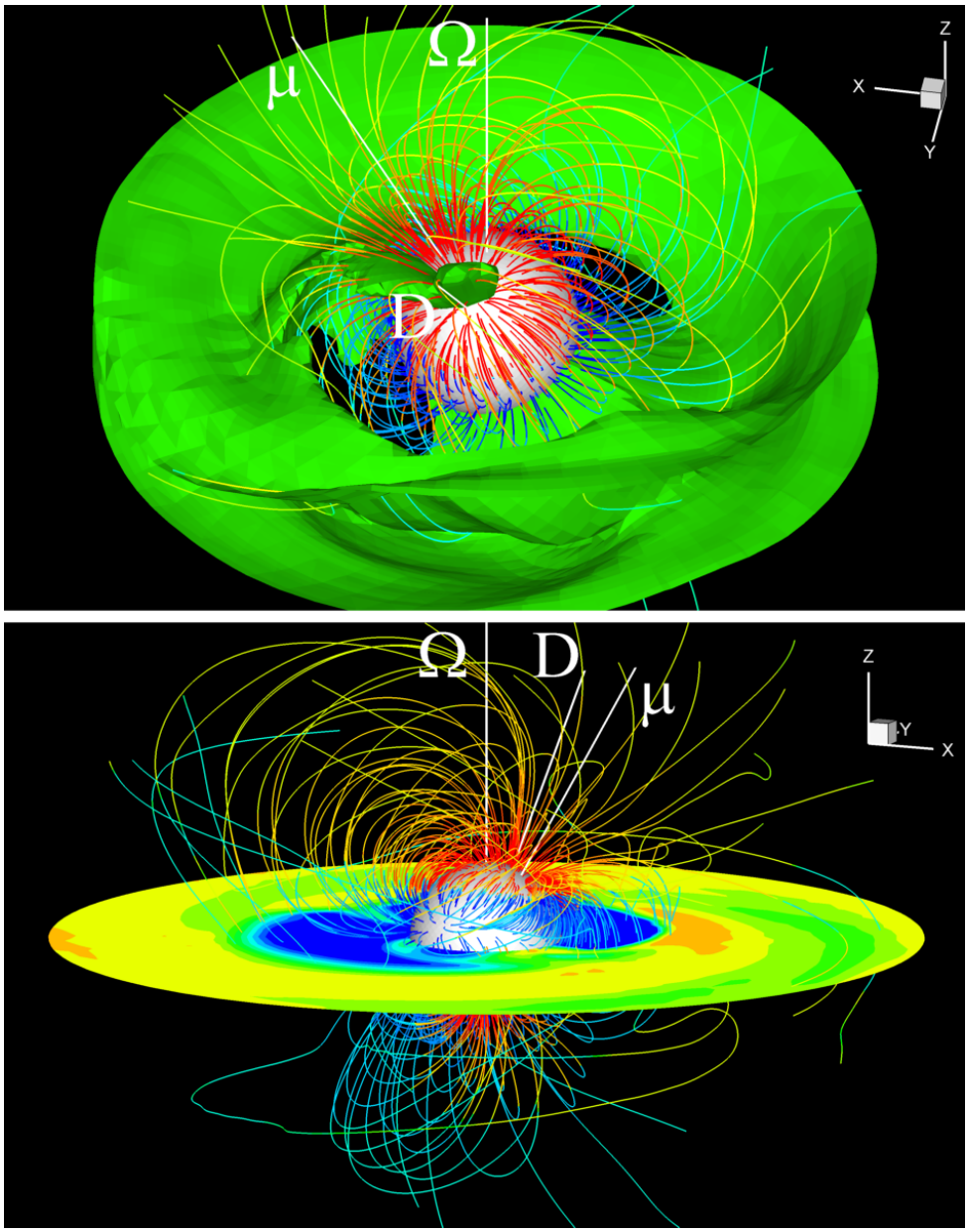

Figure 5.8: 3D views of disk accretion to a star in the more general misaligned dipole plus quadrupole case at $t = 8$, when $\mu = 0.5$, $D = 0.5$, $\Theta = 45°$, $\Theta_D = 30°$ and $\Phi = 90°$. A constant density level ($\rho = 0.25$, dimensionless value) of the disk is shown in green in the top panel; different density levels in the equatorial plane are shown in the bottom panel. The field lines are shown in multiple colors.

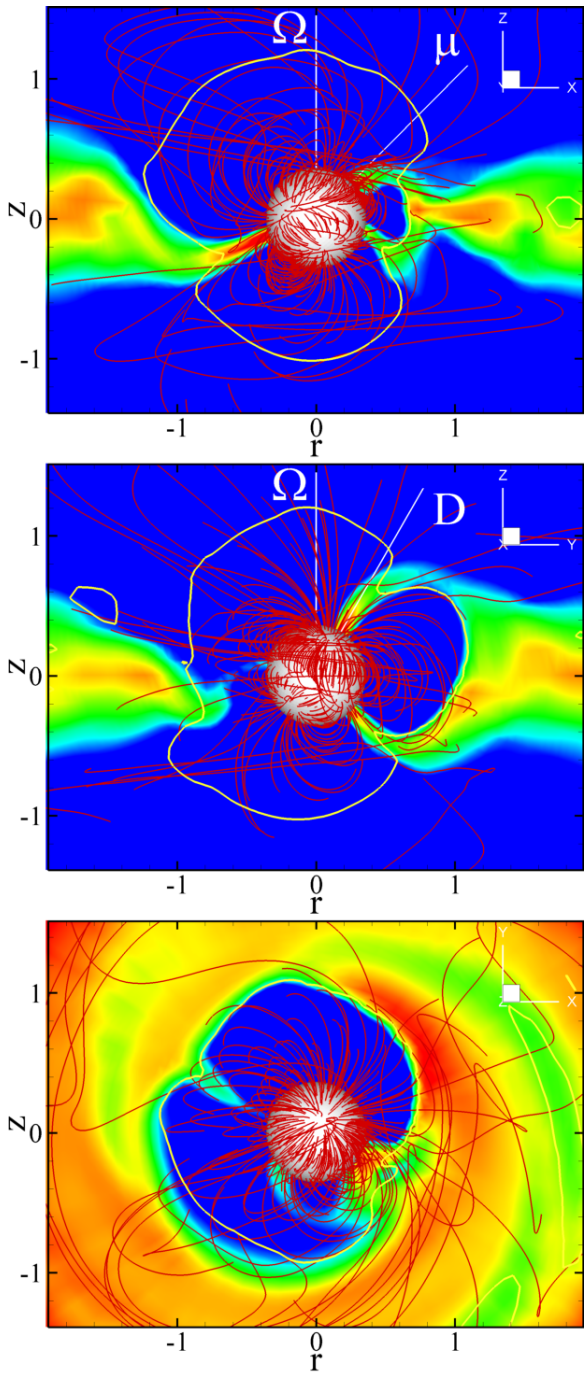

Figure 5.9: Different projections of density distribution for a more general case (μ = 0.5, D = 0.5, Θ = 45°, Θ_D = 30°, Φ = 90°). The top, middle and bottom panels show the projection in the *xz*, *yz* and *xy* planes respectively. The color background shows the density distribution varying from ρ = 0.01 (blue) to ρ = 2.1 (red). The magnetic field lines are shown in red. The yellow lines shows where β = 1.

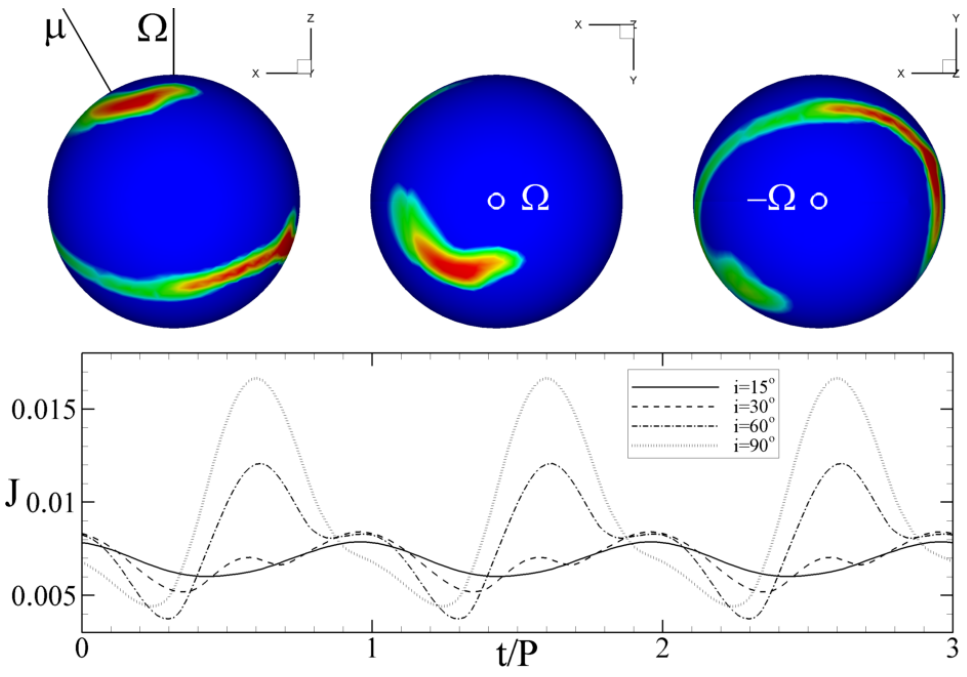

Figure 5.10: Hot spots from different angles at $t = 8$ for the case of $\mu = 0.5$, $D = 0.5$, $\Theta = 45°$, $\Theta_D = 30°$ and $\Phi = 90°$. The left-hand, middle and right-hand panels represent edge-on, top and bottom views respectively. The red color corresponds to the densest region with maximum density $\rho = 2.3$. The bottom panel shows the light curves for different inclination angles.

there is one strong arc-like hot spot near the dipole magnetic axis, but not at the magnetic pole. This hot spot comes from the one-armed stream shown in Figure 5.9. Another ring-like hot spot is below the equatorial plane but not symmetric with respect to either the $\boldsymbol{\Omega}$, $\boldsymbol{\mu}$ or $\boldsymbol{D}$ axis. The light curve is sinusoidal for the small inclination angle $i = 15°$. At larger i beside the round north spot, part of the ring-like spot becomes visible to the observer, so the light curves depart from the sinusoidal shapes and have a larger amplitude.

5.3.3 Off-centre Dipole Fields

Until now, all we discussed are cases in which the dipole and quadrupole magnetic moments are located at the center of the star. The interior convective circulations may be displaced from the center and lead to off-centre magnetic configurations. Therefore we now consider disk accretion to a star with an off-centre pure dipole field, with $\mu = 0.5$. The magnetic moment is located at $x = 0.5R_*$, $y = 0$, $z = 0$, that is, it is shifted from the centre of the star by half radius of the star. The misalignment angle is $\Theta = 30^\circ$. Figure 5.11 shows the 3D plot of disk accretion for this case. One can see that the north and south magnetic poles are not symmetric on the surface of the star. Due to the shift and the tilt of the dipole moment, the north magnetic pole is closer to the accretion disk than the south pole, so that most of the matter flows to the north magnetic pole. Figure 5.12 shows the hot spots on the surface of the star and the corresponding light curves. The light curves are sinusoidal at $i = 15^\circ, 30^\circ$, and have unusual shapes at $i = 60^\circ, 90^\circ$.

In another set of runs, we chose a superposition of several dipoles placed at different places in the star, and with different orientations of their axes. Figure 5.13 illustrates the considered configurations of three off-centre dipoles of equal value $\mu = 0.5$, displaced by $0.4R_*$ from the center of the star in the equatorial plane and azimuthally separated by 120°. In configuration (a), all moments are misaligned relative to the rotation axis at $\Theta = 30^\circ$, and in configuration (b), they are arranged in the equatorial plane in an anti-clockwise manner.

Figure 5.14 shows the distribution of the magnetic field on the surface of the star. One can see that there are six poles on the star. In case (a), three positive and three negative poles are in northern and southern hemispheres respectively. In

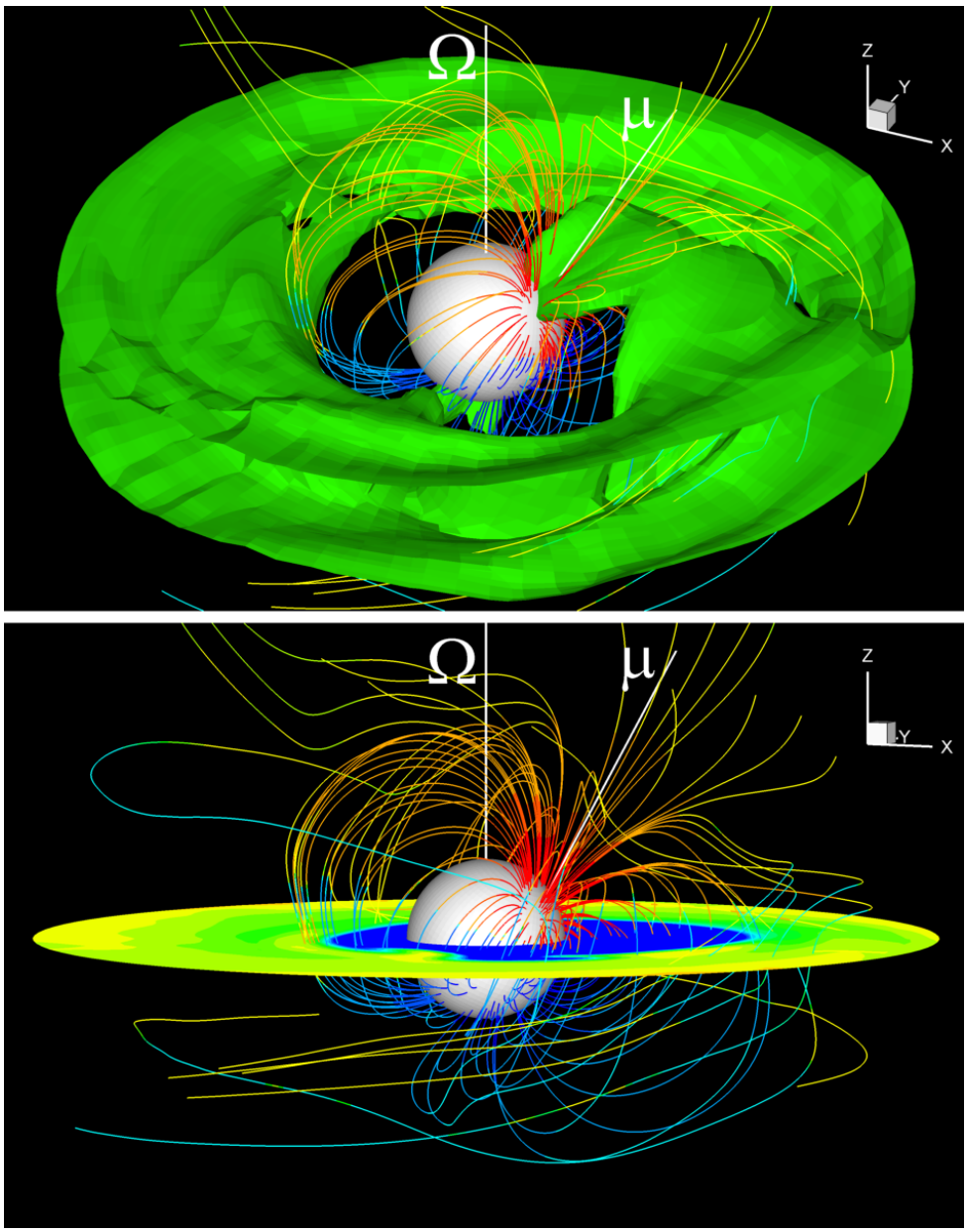

Figure 5.11: 3D views of matter flow to a star with an off-centre dipole at $t = 8$, where $\mu = 0.5$, $\Theta = 30°$ and the dipole moment is located at $x = 0.5R_*, y = 0, z = 0$. The green color in the top panel shows one of the density levels $\rho = 0.3$. The bottom panel shows the equatorial plane with different density levels. The field lines are shown in multiple colors.

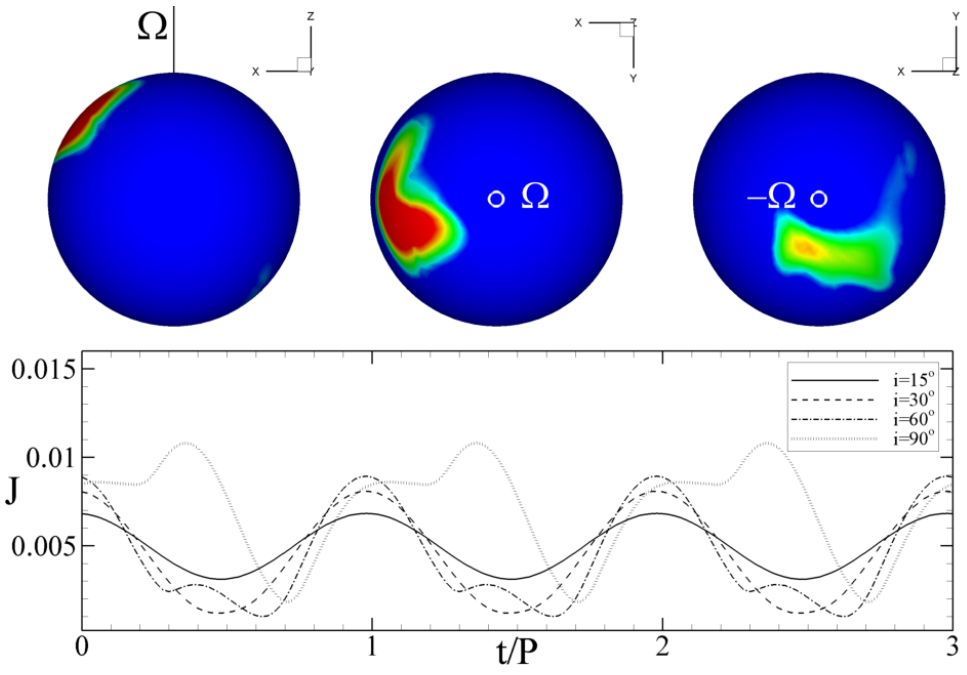

Figure 5.12: Top panel: hot spots for the off-centre case shown in Figure 5.11, at $t = 8$. The red color corresponds to the densest region with maximum density $\rho = 2.6$, and the yellow color in the right-hand panel represents the density $\rho = 0.7$. Bottom panel: the light curves.

case (b), all poles are in the equatorial planes and poles with different polarities alternate.

Figure 5.15 shows a 3D view of the matter flow for the cases (a) and (b). In case (a), most of the matter flows to the north poles which are closer to the accretion disk due to the inclination of the dipoles. The magnetospheric gap is empty in the equatorial plane. In case (b), all the matter flows between loops of the closed magnetic field lines in the equatorial plane and forms some interesting equatorial funnels.

Figure 5.16 shows the hot spots for the cases (a) and (b). There is a big trian-

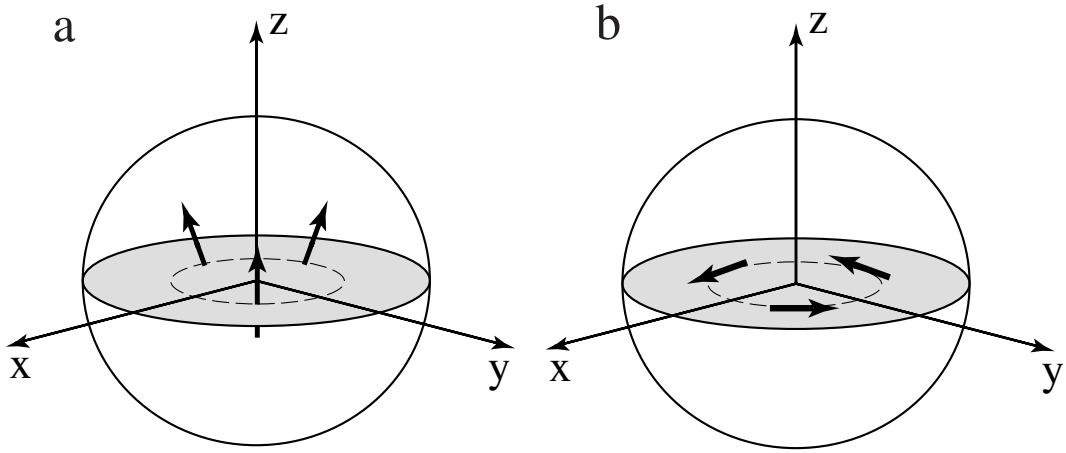

Figure 5.13: The configurations of three off-centre, equally separated dipole magnetic moments, which are $0.4R_*$ away from the center of the star in the equatorial plane, with $\mu_1 = \mu_2 = \mu_3 = 0.5$. (a) The magnetic moments are tilted away from the rotation axis at $\Theta = 30°$; (b) the magnetic moments are arranged in the equatorial plane in a circular fashion.

gular hot spot around the north pole for the case a, which spans the area near the magnetic poles. Another hot spot is present near the south pole but with very low densities. This confirms the asymmetric matter flow shown in Figure 5.15. We can also see that there are no polar hot spots for case (b). Only ring-like hot spots are present in the equatorial plane, which corresponds to what we observed in Figure 5.15.

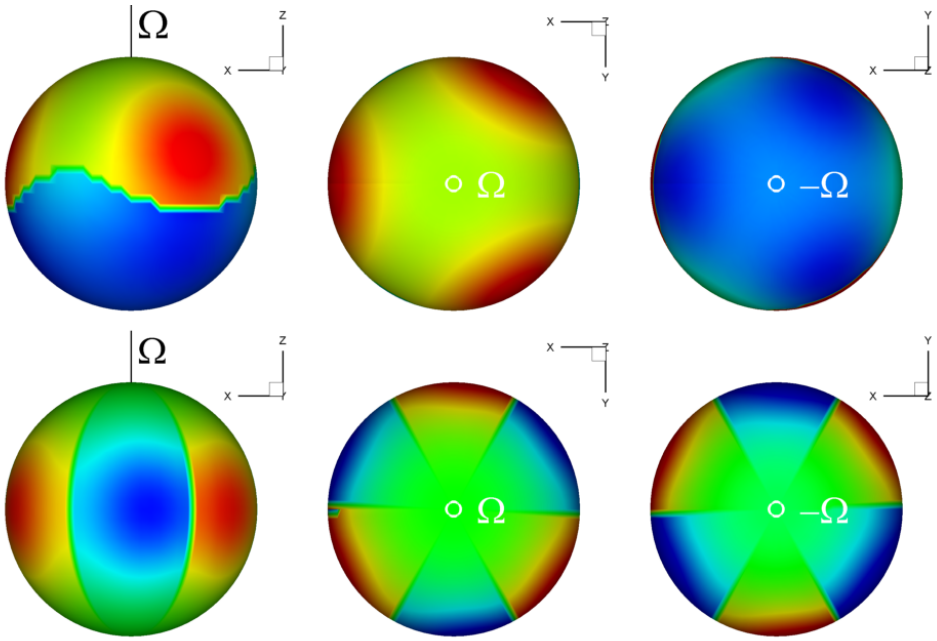

Figure 5.14: The surface magnetic field on a star with the three off-centre dipoles described in Figure 5.13. Top panel: case (a) shown in Figure 5.13; bottom panel: case (b) show in Figure 5.13.

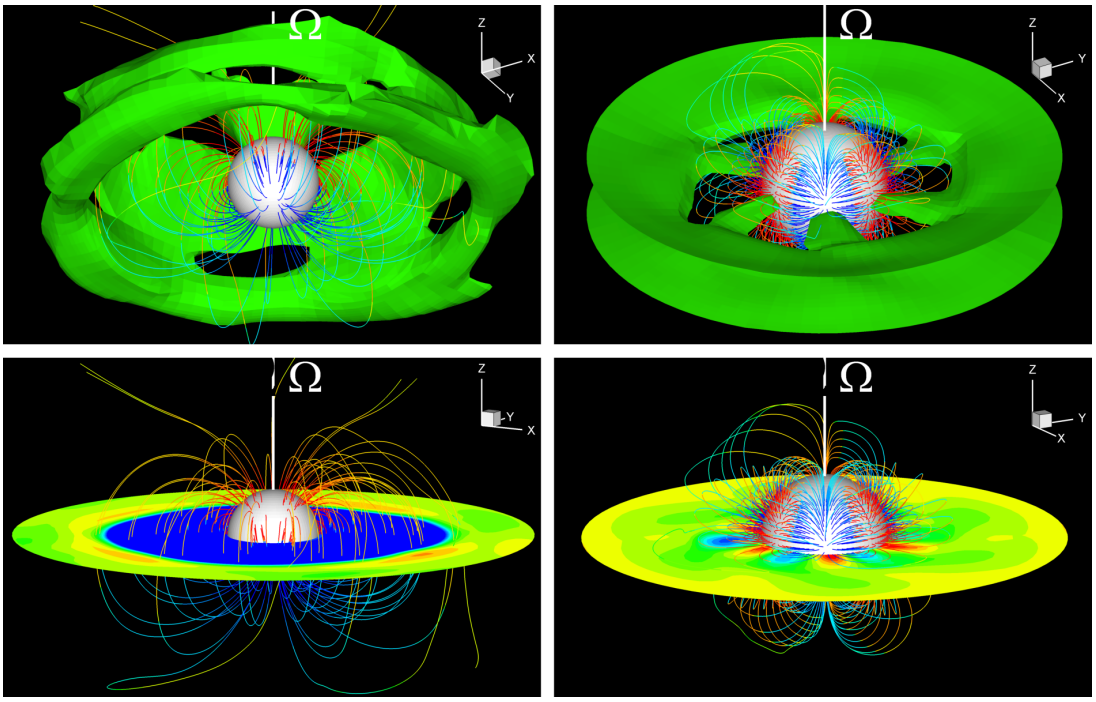

Figure 5.15: 3D views of disk accretion to a star with the three off-centered dipoles described in Figure 5.13, at $t = 8$. Left-hand panel: case (a) shown in Figure 5.13 ; Right-hand panel: case (b) shown in Figure 5.13.

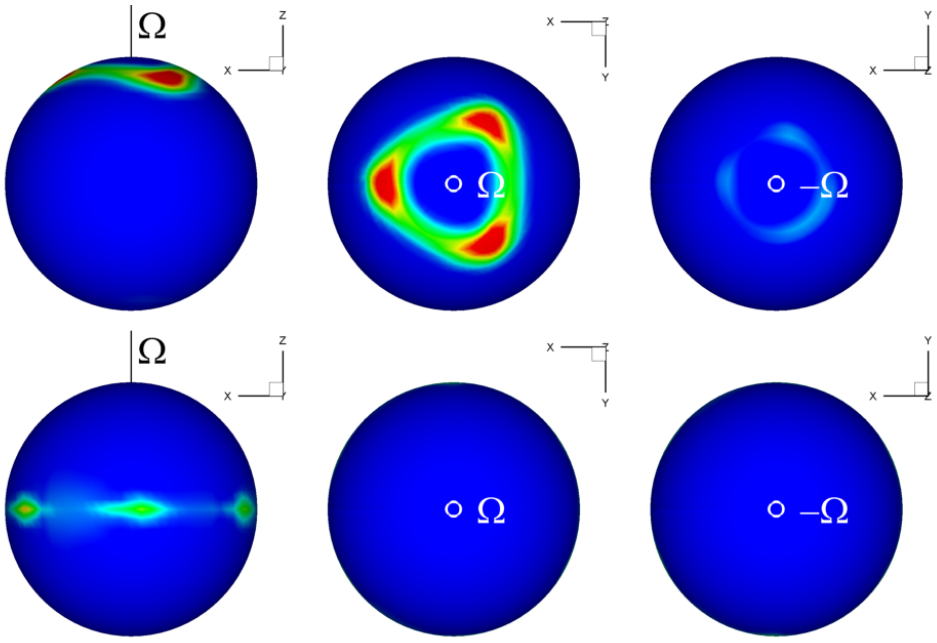

Figure 5.16: The hot spots from different angles for the cases described in Figure 5.13, at $t = 8$. Top panel: case (a), the maximum densities in the hot spots in the northern and southern hemispheres are $\rho = 1.4$ (red) and $\rho = 0.1$ (light blue) respectively. Bottom panel: case (b), the maximum density is $\rho = 0.8$.

5.4 Contribution of the Quadrupole to Properties of Magnetized stars

In this section we analyze properties of magnetized stars at different ratios between the dipole and quadrupole fields. First, we consider different configurations at the same maximum value of the field on the surface of the star. Then we analyze different properties such as the area covered by hot spots, mass accretion rate and spin torque. Next, we fix the dipole component but change the contribution of the quadrupole component with the main goal of understanding how strong the quadrupole should be compared with the dipole in order to change the shape of the hot spots from the pure dipole cases.

5.4.1 Area Covered by Hot Spots and Torque

In this section we compare properties of magnetized stars of different configurations under the condition that the maximum magnetic field on the surface of the star is the the same in all cases.

We choose a number of configurations ranging from purely dipole to purely quadrupole: (a) pure dipole field, with $\mu = 1.07$, $\Theta = 45^\circ$; (b) pure quadrupole field, with $D = 0.5$, $\Theta_D = 0^\circ$; (c) aligned dipole plus quadrupole field, with $\mu = 0.5$, $D = 0.27$, $\Theta = \Theta_D = 0^\circ$; (d) misaligned dipole plus quadrupole field, with $\mu = D = 0.37$, $\Theta = 0^\circ$, $\Theta_D = 45^\circ$. In all cases, the maximum strength of the surface magnetic field is the same, about $B_{\rm max} = 50$ (dimensionless value), but the contributions of the dipole and quadrupole components are different. In cases (a), (b) and (c), the field has a maximum value at the north pole, and in

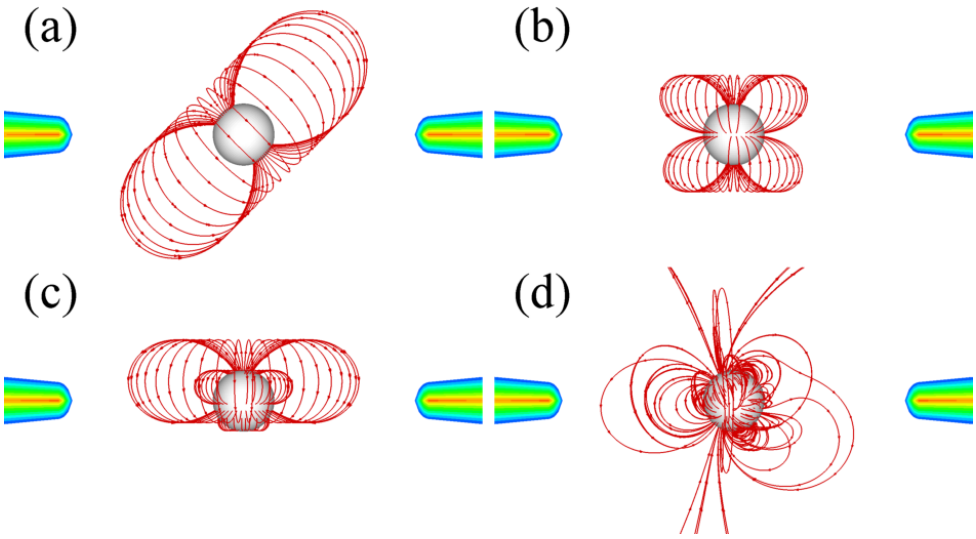

Figure 5.17: The configurations of different magnetic fields: case (a), pure dipole field; case (b), pure quadrupole field; case (c), aligned dipole plus quadrupole field; case (d), misaligned dipole plus quadrupole field.

case (d), it is near the quadrupole axis. Here, for case (a), we choose a relatively large Θ to avoid MHD instabilities (see Kulkarni & Romanova 2008, Romanova, Kulkarni & Lovelace 2008). The discussed configurations are shown in Figure 5.17. Below, we compare different properties of accretion to these stars.

Where Does the Disk Stop?

We calculated the magnetospheric radius r_m in $+x$ direction in the equatorial plane and obtained the value of r_m for above four cases: $r_{m,a} = 1.47$, $r_{m,b} = 0.62$, $r_{m,c} = 1.0$, $r_{m,d} = 1.05$ respectively. We can see that the disk stops closer to the star for the pure quadrupole case than for the pure dipole case, and r_m has intermediate values for the mixed cases. This result is expected because the quadrupole field decreases faster with distance than the dipole field, so the the disk comes

closer.

Area Covered by Hot Spots

We also calculated the area covered by hot spots in the above cases (a)-(d). Like in Romanova et al. (2004), we chose some density ρ and calculated the area $A(\rho)$ of the region where the density is larger than ρ. Then we obtain the fraction of the stellar surface covered by the spots,

$$f(\rho) = A(\rho)/A_*. \tag{5.4}$$

We also consider the temperature distribution on the surface of the star. In spite of the possible complex processes of radiation from the hot spots, we suggest that the total energy of the incoming stream is radiated approximately as a blackbody. The total energy flux carried by inflowing matter to the point $\mathbf{R}$ on the star is,

$$F_e(\mathbf{R}) = \rho \mathbf{n} \cdot \mathbf{v}(\frac{1}{2}v^2 + w), \tag{5.5}$$

where $\mathbf{n} = -\hat{\mathbf{r}}$, $\mathbf{v}$ is the matter velocity, and

$$w = \gamma(p/\rho)/(\gamma - 1) \tag{5.6}$$

is the specific enthalpy of the matter. So we have

$$F_e(\mathbf{R}) = \sigma T_{\rm eff}^4 \tag{5.7}$$

and the effective blackbody temperature,

$$T_{\rm eff} = \left[\frac{\rho \mathbf{n} \cdot \mathbf{v}}{\sigma}(\frac{1}{2}v^2 + w)\right]^{1/4}, \tag{5.8}$$

where σ is the Stefan-Boltzmann constant. Similarly, we obtain the area $A(T_{\rm eff})$ with effective temperature larger than $T_{\rm eff}$, and the fraction

$$f(T_{\rm eff}) = A(T_{\rm eff})/A_*. \tag{5.9}$$

Figure 5.18 shows the distributions of $f(\rho)$ and $f(T_{\rm eff})$ for cases (a)-(d). We can see that the area covered by spots in the pure quadrupole case (case b) is several times smaller than that in the dipole case (case a). The area covered by spots in the mixed dipole plus quadrupole cases (b and c) is in between. We conclude that if most of the field is determined by the quadrupole, the expected area covered by spots is smaller. We do not know exactly the reason for the smaller fraction f in the cases of quadrupole field. One of the factors which we should mention is that the mass accretion rate to the surface of the star is also smaller in the case of quadrupole configurations (see Figure 5.19). It seems that it is "harder" for matter to penetrate between the quadrupolar field lines to the poles compared with the dipole case, and matter accretes through a narrow quadrupole "belt" (Long et al. 2007), which leads to smaller accretion rates and smaller hot spots. Figure 5.18 also shows that for equal $f(\rho)$ or $f(T_{\rm eff})$, the density and temperature of the spots in the pure quadrupole case are smaller than in the pure dipole case.

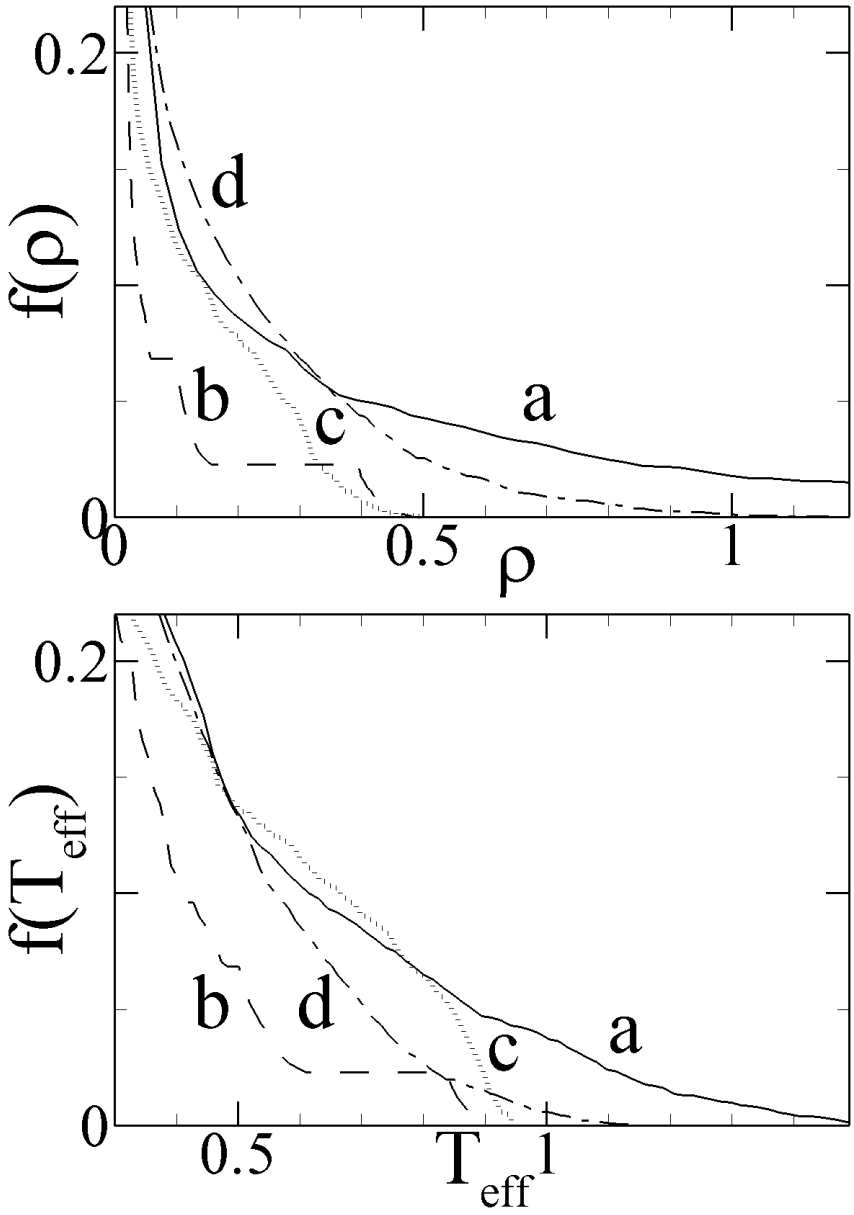

Figure 5.18: Top panel: area covered by the hot spots where the density is larger than ρ (in units of ρ_0); bottom panel: the area covered by the hot spots where the effective temperature is larger than $T_{\rm eff}$ (in units of $T_{\rm eff,0}$). The solid, dashed, dotted and dash-dotted lines represent the four cases (a)-(d) shown in Figure 5.17 respectively.

Mass Accretion Rate and Torque

As we mentioned above, matter accretion rate to the surface of the star

$$\dot{M} = -\int \mathrm{d}\boldsymbol{S} \cdot \rho \boldsymbol{v}_p \tag{5.10}$$

is several times smaller for the quadrupole case than for the dipole case ($\boldsymbol{v}_p$ is the poloidal component of the velocity). The mixed cases (c) and (d) have intermediate $\dot{M}$ (see Figure 5.19). We also calculated the angular momentum fluxes transported from the accretion disk and corona to stars for cases (a)-(d). The angular momentum flux carried by the matter

$$\dot{L}_m = -\int \mathrm{d}\boldsymbol{S} \cdot \rho r v_\phi \boldsymbol{v}_p \tag{5.11}$$

is about 10 times smaller than the angular momentum flux associated with the field

$$\dot{L}_f = \int \mathrm{d}\boldsymbol{S} \cdot r B_\phi \boldsymbol{B}_p / (4\pi). \tag{5.12}$$

So we only show $\dot{L}_f$ in Figure 5.19. When matter flows in, the magnetic field lines inflate from the initial configuration. Later, they reconnect, and the transport of angular momentum flux becomes strong. This process is longer in the pure dipole case (a). For corotation radius $r_{cor} = 2$ considered in the above cases, the star spins up mostly through the field lines connecting it to the inner part of the disk. Here we choose slowly rotating stars ($r_{cor} = 2$) for all magnetic configurations to make sure that the magnetospheric radius r_m is smaller than the corotation radius r_{cor}, and the star spins up in all cases. So we can compare the positive spin torques for different magnetic geometries. Figure 5.19 shows $\dot{M}$ and $\dot{L}_f$ for cases (a)-(d). One can see that the angular momentum flux is largest in the pure dipole case (a) and smallest in the pure quadrupole case (b). This is an interesting result because in the case of the quadrupole field, the disk comes

closer to the star and it rotates faster, so that one would expect larger angular momentum flux in the case of the quadrupole field. But we see the opposite. We can speculate that stars with predominantly multipolar fields may not spin up as fast as stars with a mainly dipole field. This can be explained by the smaller connectivity between closed multipolar field lines and the inner region of the disk (see also Long et al. 2007).

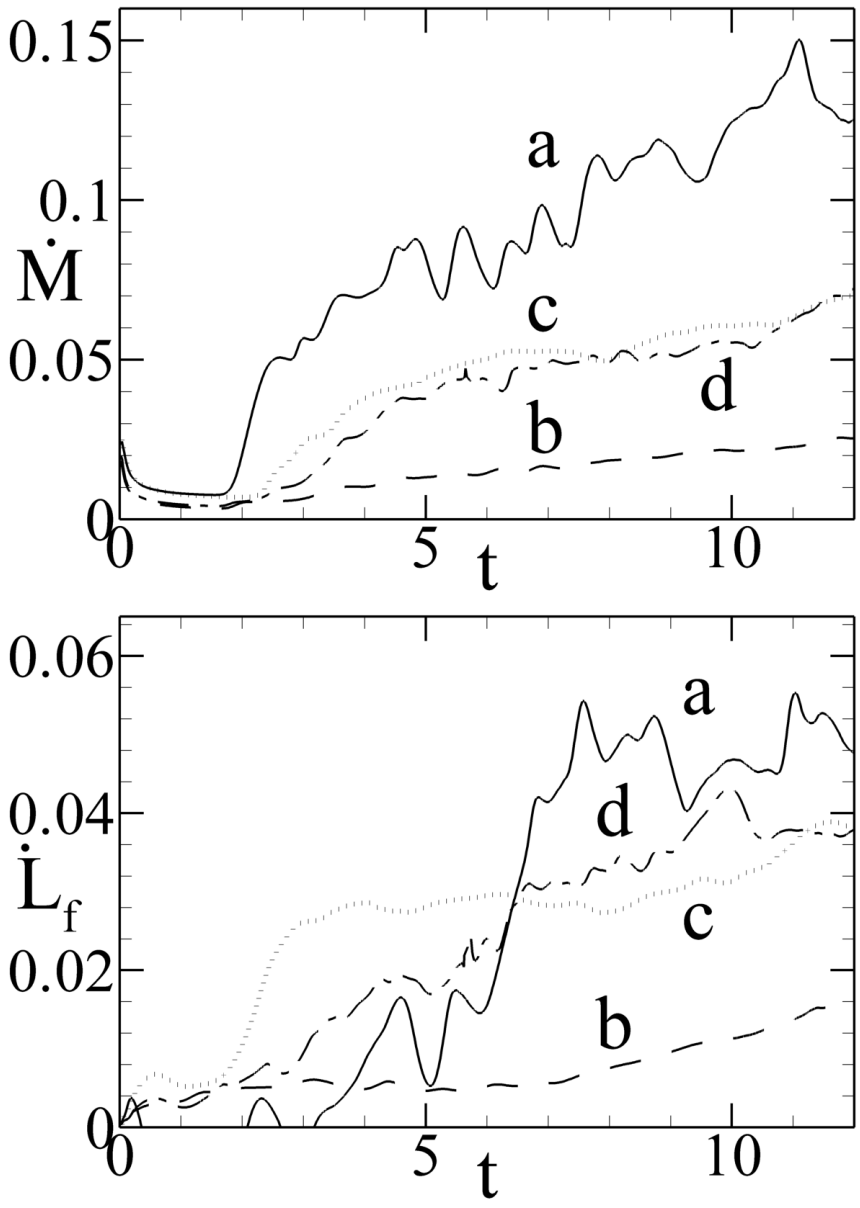

Figure 5.19: The mass accretion rate $\dot{M}$ (top panel) and the angular momentum fluxes associated with the magnetic fields $\dot{L}_f$ (bottom panel) for stars with different magnetic configurations. The solid, dashed, dotted and dash-dotted lines represent the four cases (a)-(d) shown in Figure 5.17 respectively.

5.4.2 The Shape of the Hot Spots

Next, we fix the dipole magnetic field at some relatively high value $\mu = 2$, the misalignment angle at some value $\Theta = 30^\circ$, and gradually increase the quadrupole component, $D = 0.5, 1, 1.5, 2$. In all cases, the quadrupole is aligned with the $\mathbf{\Omega}$ axis. The main goal is to understand the ratio D/μ at which the properties of hot spots will depart from the dipole ones, and the ratio D/μ at which the quadrupole will strongly influence the shape of hot spots.

Figure 5.20 shows that in the pure dipole case (left column), the hot spots have a typical arc-like shape. With the increase of the quadrupole component, the southern hot spot is stretched. When the quadrupole is strong enough, the southern hot spot forms a ring. We conclude that the influence of the quadrupole component on the shape of the hot spots becomes noticeable when the ratio of the quadrupole and dipole moments $D/\mu > 0.25$, and becomes dominant in determining the hot spot shape when $D/\mu > 0.5$. The corresponding ratios of the magnetic field strengths on the surface of the star are $B_q/B_d = 0.5$ and $B_q/B_d = 1$ respectively.

Figure 5.21 shows the light curves for the above cases. It is interesting to note that at $i = 30^\circ$ the amplitude is relatively small for the strong quadrupole case. This can be explained by the fact that part of the southern ring-like hot spot is not visible to the observers in this orientation. When the quadrupole component become more important, the intensity and amplitude of the light curves become smaller. The shape of the light curves is more irregular than in the pure dipole configuration. Light curves are complex but may provide information about the magnetic configuration of the star, if the inclination angle is known independently.

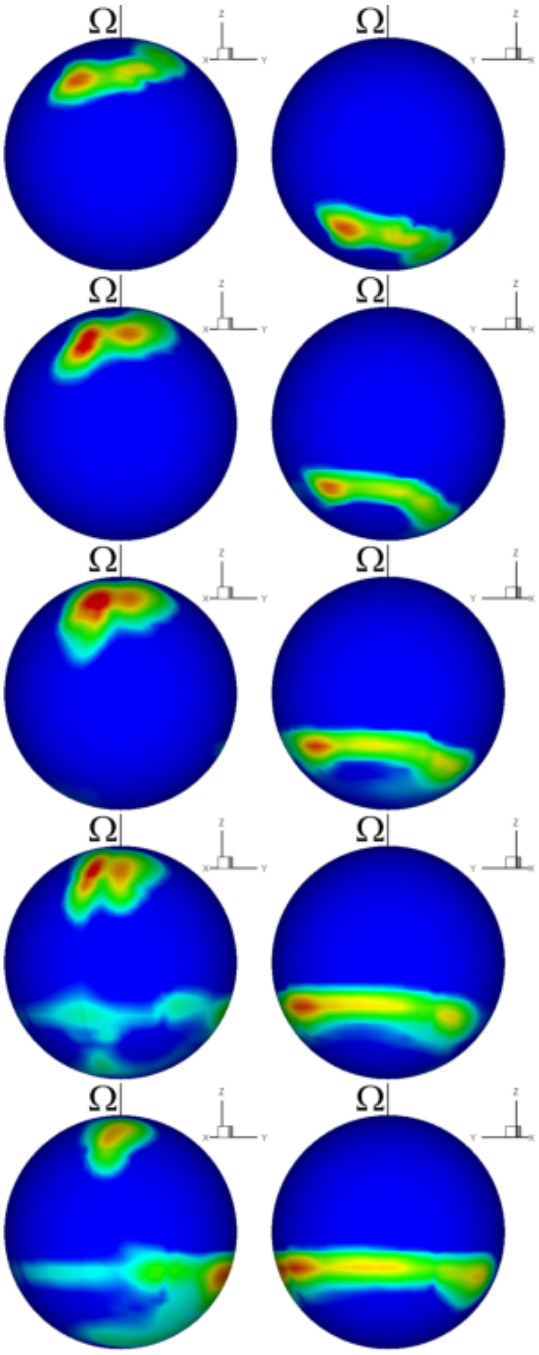

Figure 5.20: The hot spots for different cases at $t = 8$. The left column shows one side of the star, and the right column show the other. Each row represents different configurations $D = 0$, $D = 0.5$, $D = 1.0$, $D = 1.5$ and $D = 2.0$ from the left to the right respectively.

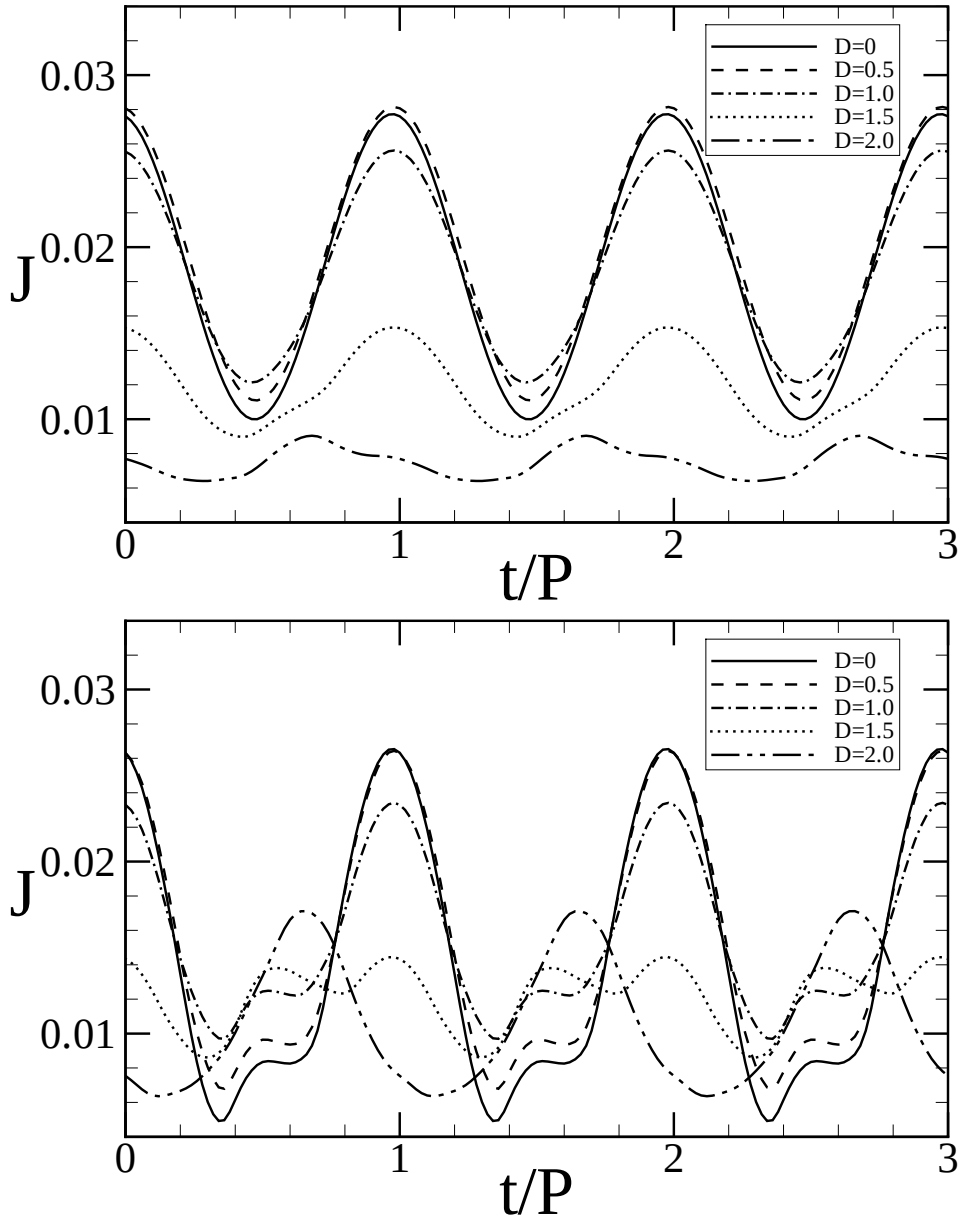

Figure 5.21: Light curves for inclination angle $i = 30°$ (top panel) and $i = 60°$ (bottom panel) at $t = 8$. The solid, dashed, dash-dotted, dotted and dash-dot-dotted lines represent the configurations $D = 0$, $D = 0.5$, $D = 1.0$, $D = 1.5$ and $D = 2.0$ respectively.

5.5 Summary and Discussion

We investigated disk accretion to rotating stars with different complex magnetic fields using full three-dimensional magnetohydrodynamic simulations. The main results of this work are the following:

1. We investigated accretion to a star with a dipole plus quadrupole field for general conditions where the moments of the dipole and quadrupole components are misaligned and also where they are in different meridional planes. We concentrated on the case where both dipole and quadrupole fields are strong so that the total field is complex. In this case, there are three major magnetic poles with different polarities on the surface of the star, and three sets of loops of closed magnetic field lines connecting these poles. The matter flow is not symmetric; it tends to flow to the star along the shortest path to the nearest magnetic pole. Most of the matter flows to the star through a narrow quadrupole "belt" between loops of field lines. Thus arc-like and ring-like hot spots typically form on the star.

2. We investigated cases with first one and then a set of off-centre dipoles. In the case of one displaced dipole, the matter flow is not symmetric. More matter flows through one stream than the others, and one hot spot is larger than the others. In the case of three displaced dipoles, there are three positive and three negative poles on the star. Depending on the directions of the dipole moments, matter flows through multiple streams and forms strong hot spots at the north pole or in the equatorial plane.

3. The mass accretion rate, the area covered by hot spots, and the torque on the star are several times smaller in the quadrupole-dominated case than in the

dipole cases (for conditions where the maximum strength of the magnetic field on the star's surface is the same).

4. The quadrupole component has a noticeable influence on the shape of hot spots if the magnetic field of the quadrupole component $B_{\rm q} \gtrsim 0.5 B_{\rm d}$ ($D/\mu \gtrsim 0.25$). The shape of hot spots is chiefly determined by the quadrupole field if $B_{\rm q} \gtrsim B_{\rm d}$ ($D/\mu \gtrsim 0.5$).

5. The light curves from hot spots of rotating stars with complex magnetic fields are often sinusoidal in the case of small inclination angles, $i \leqslant 30^\circ$, but are more complex for $i \geqslant 60^\circ$. Even for $i \geqslant 60^\circ$, the light curves often resemble those of misaligned dipoles at large i. However, in some cases they are very unusual. We conclude that, (a) very unusual, non-sinusoidal light curves may be sign of the complex fields; (b) simple sinusoidal light curves *do not* rule out complex fields; (c) light curves may be a tool for analyzing the complexity of the field, if the inclination angle is determined independently.

Many CTTSs show highly variable light curves. From our simulations we conclude that hot spots do not change their shape or position significantly and thus may not be responsible for such strong variability. The variability might be explained by some other mechanism, such as a highly variable accretion rate, or unstable accretion (Romanova, Kulkarni & Lovelace 2008; Kulkarni & Romanova 2008).

Results of 3D MHD simulations of accretion to stars with complex fields can be used to compare models with observations. For example, recently, Donati et al. (2007b) derived the magnetic topology on the surface of CTTS V2129 Oph, and found that it has a dominant octupole component with $B_{\rm oct} \sim 1.2$kG and a

weaker dipole component with $B_d \sim 0.35$kG. Most of the accretion luminosity is concentrated in a quite large high-latitude spot (5% of the total stellar surface) close to the magnetic pole. We have not modelled accretion to stars with octupole fields, but with different contributions from dipole and quadrupole components. This gives information on how matter flows to the star. Our analysis shows that the quadrupole dominantly determines the matter flow close to the star and the shape of hot spots if $B_q > B_d$. Thus, we would expect that in a star with a dominant octupole, the accretion spot would be determined by one of octupole belts, or part of the belt in the case of tilted octupole fields. So from our point of view, for such a strong octupole field, the single round spot in the high latitude region is an unexpected feature, which requires additional analysis in the future.

The results of our simulations are also important for analysis of magnetospheric gaps in young stars. In stars with multiple magnetic poles, for example, in the case of the dipole plus quadrupole fields with different orientations of the axes, the probability is high that one accretion stream crosses the equatorial plane, thus filling it with matter. This factor may be important in determining the survival of close-in exosolar planets, which have a peak in their spatial distribution at a few stellar radii. In the case of a dipole field, a large low-density magnetospheric gap may be formed in the equatorial plane, which may halt subsequent migration of planets (Lin et al. 1996, Romanova & Lovelace 2006). However, if a star has a complex magnetic field with several poles, one of streams may flow through the equatorial plane and the magnetospheric gap may be not empty.

BIBLIOGRAPHY

[1] Agapitou, V., & Papaloizou, J. C. B. 2000, MNRAS, 317, 273

[2] Attridge, J. M., & Herbst, W. 1992, ApJ, 398, L61

[3] Bardou, A. 1999, MNRAS, 306, 669

[4] Balsara, D.S. & Kim, J. 2004, ApJ, 602, 1079

[5] Bildsten, L., et al. 1997, ApJS, 113, 367

[6] Bouvier, J.Cabrit, S.,Fernández, M., Martín, E.L., & Matthews, J. M. 1993, A&A, 272,176

[7] Bouvier, J., Alencar, S.H.P., Harries, T. J., Johns-Krull, C. M., & Romanova, M. M. 2006; PPV Conference Paper, astro-ph0603498

[8] Camenzind, M. 1990, Rev. Mod. Astron., 3, 234

[9] Chakrabarty, D., Morgan, E. H., Muno, M. P., Galloway, D. K., Wijnands, R., van der Klis, M., & Markwardt, C. B. 2003, Nature, 424, 42

[10] Davidson, K., & Ostriker, J. P. 1973, ApJ, 179, 585

[11] Donati, J.-F., & Cameron, A. C. 1997, MNRAS, 291,1

[12] Donati, J.-F., Cameron, A. C., Hussain, G.A.J., & Semel, M. 1999, MNRAS, 302, 437

[13] Donati, J.-F., Forveille, T., Cameron, A.C., Barnes, J.R., Delfosse, X., Jardine, M.M., & Valenti, J.A. 2006, Science, 311, 633

[14] Donati J.-F. et al., 2007a, in van Belle G., ed., ASP Conf. Ser., Proc. 14th Meeting on Cool Stars, Stellar Systems and the Sun. Astron. Soc. Pac., San Francisco, in press (astro-ph/0702159)

[15] Donati, J.-F. et al., 2007b, MNRAS, 380, 1297

[16] Edwards, S., et al. 1993, AJ, 106, 372

[17] Elsner, R. F., and Lamb, F. K. 1977, ApJ, 215, 897

[18] Fendt, C., & Elstner, D. 1999, A&A, 349, L61

[19] Ghosh, P., & Lamb, F. K. 1978, ApJ, 223, L83

[20] Ghosh, P., & Lamb, F. K. 1979a, ApJ, 232, 259

[21] Ghosh, P., & Lamb, F. K. 1979b, ApJ, 234, 296

[22] Ghosh, P., Lamb, F. K., & Pethick, C. J. 1977, ApJ, 217, 578

[23] Goodson, A. P., Böhm, K. H., & Winglee, R. M. 1999, ApJ, 524, 142

[24] Goodson, A. P., Winglee, R. M., & Böhm, K. H. 1997, ApJ, 489, 199

[25] Gregory, S. G., Jardine, M., Simpson, I. & Donati, J.-F., 2006, MNRAS, 371, 999

[26] Hartmann, L., Hewett, R., & Calvet, N. 1994, ApJ, 426, 669

[27] Hayashi, M. R., Shibata, K., & Matsumoto, R. 1996, ApJ, 468, L37

[28] Hirose, S., Uchida, Y., Shibata, K., & Matsumoto, R. 1997, PASJ, 49, 193

[29] Jardine, M., Wood, K., Cameron, A.C., Donati, J.-F., & Mackay, D.H. 2002, MNRAS, 336, 1364

[30] Jardine, M., Cameron, A.C., Donati, J.-F., Gregory, S.G., & Wood, K. 2006, MNRAS, 367, 917

[31] Johns-Krull, C., Valenti, J.A., & Koresko, C. 1999, ApJ, 516, 900

[32] Johns-Krull, C. M., Valenti, J. A., Hatzes, A. P., & Kanaan, A. 1999, ApJ, 510, L41

[33] Johns-Krull, C. M., & Gafford, A. D. 2002, ApJ, 573, 685

[34] Johns-Krull, C. M. 2007, ApJ, 664, 975

[35] Kato, Y., Hayashi, M. R., & Matsumoto, R. 2004, ApJ, 600, 338

[36] Kenyon, S. J., Yi, I. & Hartmann, L. 1996, ApJ, 462,439

[37] Koldoba, A. V., Kuznetzov, O. A., & Ustyugova, G. V. 1992, Rep. Keldysh Inst. Applied Mathematics, Russian Acad. Sci., No. 69

[38] Koldoba, A. V., Lovelace, R. V. E., Ustyugova, G. V., & Romanova, M. M. 2002, AJ, 123, 2019

[39] Koldoba, A. V., Romanova, M. M., Ustyugova, G. V., & Lovelace, R. V. E. 2002, ApJ, 576, L53

[40] Koldoba, A. V., & Ustyugova, G. V. 1994, Rep. Keldysh Inst. Applied Mathematics, Russian Acad. Sci., No. 87

[41] Königl, A. 1991, ApJ, 370, L39

[42] Kulkarni, A. K., & Romanova, M. M. 2005, ApJ, 633, 349

[43] Kulkarni, A. K., & Romanova, M. M. 2008, MNRAS, in press, astro-ph0802.1759

[44] Lamb, F. K., Pethick, C. J., & Pines, D. 1973, ApJ, 184, 271

[45] Landau, L. D., & Lifshitz E. M. 1983, *The Classical Theory of Fields, Fourth English Edition*

[46] Li, J., & Wickramasinghe, D. T. 1997, MNRAS, 286, L25

[47] Lin, D.N.C., Bodenheimer, P. & Richardson, D.C. 1996, Nature, 380, 606

[48] Lipunov, V.M. 1978, Soviet Astronomy, 22, 702

[49] Long, M., Romanova, M. M., & Lovelace, R. V. E. 2005, ApJ, 634, 1214

[50] Long, M., Romanova, M. M., & Lovelace, R. V. E. 2007, MNRAS, 374, 436

[51] Lovelace, R. V. E., Romanova, M. M., & Bisnovatyi-Kogan, G. S. 1995, MNRAS, 275, 244

[52] Lovelace, R. V. E., Romanova, M. M., & Bisnovatyi-Kogan, G. S. 2005, ApJ, 625, 957

[53] Matt, S., & Pudritz, R.E. 2004, ApJ, 607, L43

[54] Matt, S., & Pudritz, R.E. 2005, MNRAS, 356, 167

[55] Miller, K. A., & Stone, J. M. 1997, ApJ, 489, 890

[56] Nagase, F. 1989, PASJ, 41, 1

[57] Powell, K.G., Roe, P.L., Linde, T.J., Gombosi, T.I., & De Zeeuw, D.L. 1999, J. Comp. Phys., 154, 284

[58] Pringle, J. E., & Rees, M. J. 1972, A&A, 21, 1

[59] Romanova, M. M., Kulkarni, A. K., & Lovelace, R. V. E. 2008, ApJ, 673, L171

[60] Romanova, M. M., & Lovelace, R. V. E. 2006, ApJ, 645, L73

[61] Romanova, M. M., Ustyugova, G. V., Koldoba, A. V., Chechetkin, V. M., & Lovelace, R. V. E. 1998, ApJ, 500, 703

[62] Romanova, M. M., Ustyugova, G. V., Koldoba, A. V., & Lovelace, R. V. E. 2002, ApJ, 578, 420

[63] Romanova, M. M., Ustyugova, G. V., Koldoba, A. V., & Lovelace, R. V. E. 2003, ApJ, 595, 1009

[64] Romanova, M. M., Ustyugova, G. V., Koldoba, A. V., & Lovelace, R. V. E. 2004, ApJ, 616, L151

[65] Romanova, M. M., Ustyugova, G. V., Koldoba, A. V., & Lovelace, R. V. E. 2004, ApJ, 610, 920

[66] Safier, P. N. 1998, ApJ, 494, 336

[67] Scholz, A., & Ray, J. 2006, ApJ, 638, 1056

[68] Shakura, N. I., & Sunyaev, R. A. 1973, A&A, 24, 337

[69] Shu, F. H., Najita, J., Ruden, S. P., & Lizano, S. 1994, ApJ, 429, 797

[70] Smirnov, D.A., Lamzin, S.A., Fabrika, S.N., & Valyavin, G.G. 2003, A&A, 401, 1057

[71] Symington, N.U., Harries, T.J., Kurosawa, R., & Naylor, T. 2005, MNRAS, 358, 977

[72] Tanaka, T. 1994, J. Comput. Phys., 111, 381

[73] Toro E. F., 1999, *Riemann Solvers and Numerical Methods for Fluid Dynamics: A Practical Introduction*, 2nd edn. Springer-Verlag, Berlin

[74] Ustyugova, G. V., Koldoba, A. V., Romanova, M. M., Chechetkin, V. M., & Lovelace, R. V. E. 1995, ApJ, 439, L39

[75] Ustyugova, G. V., Koldoba, A. V., Romanova, M. M., Chechetkin, V. M., & Lovelace, R. V. E. 1999, ApJ, 516, 221

[76] Ustyugova, G. V., Koldoba, A. V., Romanova, M. M., & Lovelace, R. V. E. 2006, ApJ, 646, 304

[77] Uzdensky, D.A., Königl, A., & Litwin, C. 2002, ApJ, 565, 1191

[78] Uzdensky, D.A., Königl A., & Litwin, C. 2002, ApJ, 565, 1205

[79] Valenti, J.A., & Johns-Krull, C.M. 2004, Ap&SS, 292, 619

[80] van der Klis, M. 2000, Annu. Rev. Astron. Astrophys, 38, 717

[81] von Rekowski, B., & Brandenburg, A. 2004, A&A, 420, 17

[82] von Rekowski, B., & Brandenburg, A. 2006, Astron. Nachr., 327, 53

[83] Wang, Y.-M. 1995, ApJ, 449, L153

[84] Warner, B. 1995, *Cataclysmic Variable Stars* (Cambridge: Cambridge Univ. Press)

[85] Warner, B. 2000, PASP, 112, 1523

[86] Warner, B. 2004, PASP, 116, 115

[87] Wickramasinghe, D. T., Wu, K., & Ferrario, L. 1991, MNRAS, 249, 460

[88] Wijnands R., 2004, in Kaaret P., Lamb F. K., Swank J. H., eds, AIP Conf. Proc. Vol. 714, X-ray Timing 2003: Rossi and Beyond. Am. Inst. Phys., Melville, NY, p. 209